Aerodynamic Optimization of a Sounding Rocket at Mach 1.5: Analysis of Nose Cone, Fin, and Canard Configurations

A project presented to
The Faculty of the Department of Aerospace Engineering
San Jose State University

In partial fulfillment of the requirements for the degree
Master of Science in Aerospace Engineering

By

Osiris L. Zamudio Jr

May 2025

Approved by

Dr. Yawo Ezunkpe
Faculty Advisor

© 2025
Osiris Lenin Zamudio Jr
ALL RIGHTS RESERVED

ABSTRACT

Aerodynamic Optimization of a Sounding Rocket at Mach 1.5: Analysis of Nose Cone, Fin, and Canard Configurations

Osiris L. Zamudio Jr

This study investigates the aerodynamic optimization of a supersonic sounding rocket at Mach 1.5 through systematic computational fluid dynamics (CFD) analysis. Detailed two-dimensional simulations were conducted to evaluate the aerodynamic performance of multiple nose cone profiles, tail fin shapes, and canard configurations under compressible, steady-state, supersonic flow conditions. Three primary nose cone geometries ogive, von Kármán, and long ellipsoid were analyzed across fineness ratios from 4:1 to 7:1, while tail fins and canards were assessed based on their ability to minimize drag and enhance stability at critical deflection angles. Building on the results, three conceptual 3D rocket configurations were proposed to target different mission profiles: efficiency-oriented, control authority-focused, and balanced performance designs. This research also identified several key areas for future work, including expansion into full three-dimensional CFD modeling, high-altitude dynamic simulations, and coupled aerodynamic-thermal analysis. The findings of this study contribute to the broader understanding of high-speed aerodynamic behavior and establish a strong foundation for future development of supersonic and hypersonic aerospace vehicles. By systematically evaluating each aerodynamic component and their interactions, this project offers practical insights for advancing the next generation of efficient, stable, and mission-adaptable rocket designs.

ACKNOWLEDGEMENTS

I would like to sincerely thank Dr. Yawo Ezunkpe, whose guidance and leadership were essential in the completion of this project and throughout my time at San Jose State University. Dr. Ezunkpe was the professor who opened my eyes to the fascinating world of supersonic and hypersonic flight, teaching me the critical science and mathematics that became the backbone of this research. His classes were challenging yet deeply rewarding, and his constant encouragement gave me the confidence to push my limits academically and professionally. I am also incredibly grateful to Tom Rouse, who played a major role in building my passion for aerospace through hands-on learning. Under his direction, I was able to design, build, and launch my very first rocket an experience that didn't just teach me technical skills, but sparked a real excitement for the field that has shaped my career goals ever since. I am especially grateful to my mentor Scott Wong, who I met in high school and who helped guide me through the college application process as a first-generation college student. Without his wisdom, encouragement, and belief in my potential, I would not have known how to begin this journey into higher education. I also want to extend my appreciation to my classmates and the entire Aerospace Engineering Department staff, whose collaboration and support made the difficult days easier and the good days even more memorable. Finally, I am thankful to San Jose State University for providing a community that truly encouraged my growth, and for giving me the opportunity to pursue my education at such a respected and challenging institution.

I am forever thankful to my family; my mom, dad, sister, and brother; who have always believed in my dreams, even when they seemed impossibly far away. From the very beginning, they supported my passion for space exploration, encouraged my love of engineering, and gave me the opportunity to follow this path with their unwavering belief and sacrifices. Their love and support are the foundation of everything I have achieved, and without them, I would not be where I am today. Every late night, every tough exam, and every small victory was fueled by the knowledge that they were standing with me, cheering me on. I would also like to give a special thank you to my girlfriend, Vicky, whose constant support, patience, and belief in me made even the hardest moments feel lighter. Having people like them by my side made this journey not only possible, but unforgettable and for that, I am endlessly grateful.

TABLE OF CONTENTS

LIST OF TABLES

LIST OF FIGURES

NOMENCLATURE

Symbol	Definition	Units (SI)
ρ	Density	kg/m³
t	Time	s
u	Velocity	m/s
∇	Gradient Operator	1/m
p	Pressure	Pa (N/m²)
τ	Viscous Stress Tensor	Pa (N/m²)
f	Body Force Per Unit Mass (Gravity)	m/s²
T	Temperature	K
k	Thermal Conductivity	W/(m·K)
E	Specific Internal Energy	J/kg
R	Specific Gas Constant	J/(kg·K)
Re	Reynolds Number	Dimensionless
L	Length	m
μ	Dynamic Viscosity	Pa·s (N·s/m²)
M	Mach Number	Dimensionless
a	speed of sound	m/s
γ	Ratio of Specific Heats	Dimensionless
ν	Kinematic Viscosity	m²/s
n	Number of Moles of Gas	mol
V	Volume	m³
∂	Partial Derivative	-
ρ	Radius of Curvature	m
r	radius	m

1. Introduction

1.1. Motivation

Over the past half-century, aerospace vehicles powered by the solid rocket propulsion systems are the most reliable, efficient, and cost-effective. Consequently, current aerospace vehicles can achieve high velocities but encounter significant aerodynamic impediments. One of the leading components is the nose cone, which is the forward section that is subject to the aerothermodynamics effects. Larger-diameter rockets experience significant drag due to increased air displacement, escalating non-linearly with speed. Furthermore, as rockets approach and surpass the speed of sound, the formation of shock waves results in heightened drag and surface pressure. High angles of attack introduce turbulent airflow, which generates unpredictable aerodynamic forces and potential instability. This research aims to optimize the airframe, nose cone profile, and fin configuration to mitigate these issues, thereby improving the aerodynamic efficiency and overall performance of rockets at supersonic speeds. By addressing these aerodynamic challenges, this study contributes to the advancement of high-speed rocket technology, offering potential improvements in both efficiency and stability.

1.2. Literature Review

The aerodynamic design and performance of rockets, especially in supersonic and high-altitude flight regimes, are crucial for stability, efficiency, and mission success. Recent studies have explored various aspects of rocket design, including nose cone geometries, heat transfer, aerodynamic stability, and computational methods. This literature review establishes findings from 20 key studies, providing a comprehensive overview of current research trends and methodologies in this field.

1.2.1. Nose Cone Design and Geometrical Optimization

The shape of the nose cone is crucial in minimizing drag and enhancing the aerodynamic stability of rockets and missiles, especially in supersonic and transonic regimes. Velmani and Suresh [1] conducted a comprehensive numerical study to assess the impact of freestream turbulence on various nose cone geometries in supersonic flows. Their findings revealed that turbulence intensity significantly influences drag and flow separation, with higher turbulence levels exacerbating boundary layer separation and increasing drag. This study underscores the importance of selecting nose cone shapes that can withstand turbulent conditions while maintaining streamlined flow characteristics. Building on this, Shah [2] explored optimal geometries for supersonic missile nose cones, identifying specific shapes such as the bi-conic and tangent ogive that effectively minimize shock wave formation and aerodynamic drag at high speeds. By reducing the intensity of shock waves, these geometries not only lower drag but also improve overall stability, making them ideal for high-speed flight applications.

In addition to these studies, Belega [3] utilized advanced computational techniques, including Computational Fluid Dynamics (CFD) and Smoothed Particle Hydrodynamics (SPH), to analyze a novel aerodynamic nose cone design. This hybrid approach allowed for a more accurate prediction of complex flow patterns around the nose cone, highlighting the design's potential to reduce drag and control flow separation more effectively than traditional shapes. Eghlima and Mansour [4] further investigated the influence of different nose shapes on shock standoff distance in near-sonic flows, which is critical for mitigating aerodynamic heating and drag. Their study demonstrated that elongated and streamlined nose shapes significantly decrease shock standoff distances, reducing the heat load on the vehicle and improving aerodynamic efficiency. Together, these studies provide a detailed understanding of how nose cone geometry affects performance in high-speed flight, offering valuable guidelines for optimizing designs to achieve minimal drag and maximum stability.

1.2.2. Heat Transfer and Thermal Management

Thermal effects are critical in supersonic flight due to the high aerodynamic heating experienced at these speeds. This heating results from the rapid compression and friction of air molecules against the rocket's surface, leading to elevated temperatures that can compromise structural integrity and material properties. Effective thermal management is essential to protect critical components and ensure the vehicle's performance and safety. The study of heat transfer in a supersonic rocket head provides an in-depth examination of the heat transfer mechanisms affecting components in supersonic flow [4]. It explores conduction, convection, and radiation heat transfer modes, considering various nose cone materials and coatings to evaluate their thermal resistance and suitability for high-speed applications. The findings underline the importance of selecting appropriate thermal protection systems (TPS) that can withstand extreme temperature gradients without significant degradation or failure.

Sahbon [5] conducted a comprehensive CFD study of the aerodynamic characteristics of the Twardowsky and FOK rockets, incorporating a detailed thermal analysis to assess heat distribution and its impact on structural components. Their work revealed that localized heating, especially near the nose cone and leading edges, can lead to concentrations of thermal stress, potentially resulting in material fatigue and failure if not properly managed. By simulating various flow conditions and thermal loads, the study provided valuable insights into optimizing TPS design and material selection to enhance the rockets' durability and performance. Furthermore, their research highlighted the influence of flight speed and altitude on the thermal load distribution along the rocket's surface, necessitating a tailored TPS approach that accounts for varying thermal conditions throughout the flight profile. The use of advanced CFD techniques allowed precise modeling of these complex interactions, demonstrating the importance of integrating thermal analysis into the early stages of rocket design to address potential thermal challenges proactively.

1.2.3. Aerodynamic Stability and Control

Cadamuro [6] presented a comprehensive static stability analysis method for passively stabilized sounding rockets, offering a robust framework for evaluating their stability without relying on active control systems. This approach is particularly valuable for missions where simplicity, reliability, and cost-effectiveness are critical, as passive stabilization minimizes the need for complex guidance mechanisms. By analyzing the rocket's center of pressure and center of gravity positions, their method provides insights into the stability margins and aerodynamic behavior throughout the flight trajectory. The study also highlighted the importance of fin geometry and placement in maintaining stability, offering practical guidelines for optimizing design parameters to achieve desirable aerodynamic characteristics. Milne [7] further advanced this field by developing a high-fidelity dynamics model for a high-altitude supersonic sounding rocket. Their model integrates aerodynamic, structural, and environmental factors, allowing for precise predictions of flight dynamics and stability under a range of operating conditions. This multi-disciplinary approach enables engineers to simulate various flight scenarios, evaluate potential instabilities, and refine design configurations before conducting physical tests.

Building on these contributions, Barrowman [8] provided a seminal method for calculating the aerodynamic characteristics of slender-finned vehicles, formulating equations that have become a cornerstone in rocketry stability and control analysis. His work established a systematic way to determine the normal force and moment coefficients, which are critical for predicting the rocket's behavior in flight. These formulas remain widely used in both academic research and practical applications, serving as a benchmark for more complex computational models. Kumar [9] explored the effect of Mach number on the drag coefficient of sounding rockets, using computational fluid dynamics (CFD) to analyze how changes in speed influence aerodynamic forces. Their findings indicated that as Mach number increases, the drag coefficient initially rises due to shock wave formation and flow separation but stabilizes at higher supersonic speeds. This research provides essential data for optimizing rocket designs to minimize drag and enhance performance, particularly in high-speed flight regimes. Together, these studies contribute to a deeper understanding of the aerodynamic and stability considerations essential for the successful design and operation of sounding rockets.

1.2.4. Drag Reduction Techniques

Drag reduction is a critical aspect of optimizing the efficiency and performance of high-speed rockets, as it directly impacts fuel consumption, stability, and overall mission success. Famellos [10] conducted a detailed investigation into the use of a base bleed unit for drag reduction in high-power rockets operating at transonic speeds. This technique involves introducing a controlled flow of gas from the rear of the rocket to fill the wake region, thereby reducing pressure drag and minimizing turbulent flow separation. Their study demonstrated that implementing a base bleed unit can lead to significant improvements in aerodynamic efficiency, reducing drag by up to 15% in some configurations. These findings have substantial implications for the design of transonic and supersonic vehicles, as reducing drag not only enhances speed and range but also

improves stability and control by mitigating adverse aerodynamic forces. The research provides valuable guidelines for integrating base bleed systems into rocket designs, enabling more efficient propulsion and better performance across a wide range of operating conditions.

In another innovative approach to drag reduction, Brocksmith [11] explored the application of tubercles—wave-like protrusions along the leading edge of rocket fins—using computational fluid dynamics (CFD) analysis. His research focused on evaluating the aerodynamic benefits of tubercles at very high Reynolds numbers, which are characteristic of high-speed rocket flights. The results indicated that tubercles can significantly reduce drag and improve the overall aerodynamic stability of the rocket by disrupting the spanwise flow and delaying flow separation along the fin surfaces. This leads to smoother airflow and reduced pressure drag, particularly in regimes where traditional fin designs might experience increased resistance and instability. By demonstrating that tubercles can enhance both aerodynamic efficiency and structural performance, this study opens new avenues for the design of rocket fins, particularly for missions requiring high maneuverability and precise control. Together, these studies underscore the importance of innovative aerodynamic modifications in advancing the performance of high-speed rockets, highlighting the potential for novel design elements to achieve significant drag reduction and efficiency gains.

1.2.5. Tail Fin Configurations and Stability

Tail fin configurations play a crucial role in ensuring the stability and control of sounding rockets, particularly at high speeds and varying flight conditions. Sankalp [12] conducted an extensive computational analysis to evaluate the impact of different tail fin designs on the aerodynamic performance of sounding rockets. Their study explored various configurations, including trapezoidal, delta, and elliptical fin shapes, to determine their effects on stability, drag, and overall flight dynamics. The findings indicated that specific fin shapes could significantly enhance the rocket's stability by improving the aerodynamic center of pressure and reducing oscillatory movements. For example, delta fins provided better stability at high angles of attack, while trapezoidal fins demonstrated lower drag coefficients, making them suitable for missions prioritizing speed and fuel efficiency. These insights are valuable for engineers looking to optimize fin configurations based on mission-specific requirements, such as achieving a stable ascent phase or minimizing aerodynamic resistance during supersonic flight.

In a related study, Li [13] investigated the aerodynamic characteristics and flight trajectories of tail fin-stabilized projectiles with various shapes, further contributing to the understanding of fin design optimization. Their research focused on analyzing how different fin geometries influence factors such as lift, drag, and moment coefficients, which are crucial for maintaining stable flight paths. By employing both experimental testing and computational simulations, the study provided comprehensive data on the performance of different fin configurations, including rectangular, swept, and ogive-shaped fins. The results showed that swept

fins, due to their tapered design, offered improved aerodynamic efficiency and better control over the projectile's flight path compared to conventional rectangular fins. Moreover, the study highlighted the importance of fin aspect ratio and sweep angle in determining the aerodynamic stability and maneuverability of the vehicle. Together, these studies underscore the significance of tail fin design in enhancing the stability and control of sounding rockets, offering valuable guidelines for tailoring fin configurations to meet specific aerodynamic and mission requirements.

1.2.6. Aeroelastic Effects and Structural Dynamics

The interaction between aerodynamic forces and structural dynamics is a critical area of research, particularly for slender spinning sounding rockets, where structural flexibility can significantly influence flight performance. Silva [14] conducted a detailed sensitivity analysis on the aeroelastic dynamic stability of such rockets, focusing on how structural deformations and spin rates interact with aerodynamic forces. Their study revealed that the structural flexibility of the rocket body, combined with its high rotational speeds, can lead to complex aeroelastic phenomena such as bending torsion coupling and flutter. These effects can destabilize the vehicle, causing deviations from the intended flight path and potentially leading to structural failure. By using computational models to simulate various flight conditions and structural configurations, the researchers were able to identify critical spin rates and structural stiffness parameters that minimize adverse aeroelastic interactions. This research provides essential guidelines for designing slender spinning rockets with enhanced stability and control, ensuring reliable performance even under the demanding conditions of high-speed flight.

Building on these insights, Minotti [15] proposed a comprehensive design methodology that integrates aeroelastic considerations into the performance evaluation of new generation sounding rockets. Their approach emphasizes the importance of accounting for both aerodynamic loads and structural dynamics during the early design stages, allowing for a more accurate prediction of the rocket's behavior under various flight scenarios. By incorporating aeroelastic analysis into the overall design process, the methodology enables engineers to optimize the structural configuration and material selection to reduce the risk of aeroelastic instabilities. For example, their study demonstrated how modifying fin placement and using composite materials can improve aeroelastic stability without compromising aerodynamic performance. This integrated approach not only enhances the reliability and safety of the rocket but also allows for more efficient designs by balancing aerodynamic efficiency with structural robustness. Together, these studies underscore the necessity of considering aeroelastic effects in the design and evaluation of sounding rockets, paving the way for the development of more advanced and reliable aerospace vehicles.

1.2.7. Computational and Experimental Methodologies

Advanced computational methods are becoming indispensable for modeling the complex aerodynamic phenomena encountered by sounding rockets, particularly when traditional experimental techniques are limited by cost or technical constraints. Endo [16] leveraged high-

resolution simulations to investigate the interaction between an ionospheric sounding rocket and the surrounding plasma environment, focusing on wake-induced plasma waves. These waves are generated by the rocket's passage through the ionosphere, where it disrupts the ambient plasma flow, leading to the formation of intricate wave patterns in its wake. By using sophisticated numerical models to simulate these interactions, the researchers were able to capture the dynamic behavior of plasma waves, which can influence communication signals and the rocket's trajectory. Their findings are crucial for understanding the plasma-rocket interactions that can occur during high-altitude missions and for developing strategies to mitigate their potential impacts on vehicle performance and mission success. This study highlights the value of advanced simulations in exploring the complex coupling between a rocket's physical structure and the surrounding ionospheric environment, where traditional wind tunnel tests are not feasible.

In a complementary effort, de Neto [17] employed advanced computational techniques, such as chimera and patched multiblock meshes, to study the aerodynamic characteristics of sounding rockets under various flow conditions. These methods enable the simulation of complex, multi-scale flow fields around the rocket, allowing for a detailed analysis of interactions between different flow regions, such as the boundary layer, shock waves, and wake. By utilizing these computational tools, the researchers were able to achieve high-resolution results that are essential for accurately predicting aerodynamic forces and moments on the rocket. Their study demonstrated the effectiveness of these techniques in capturing intricate flow phenomena that are difficult to replicate in experimental setups, providing valuable data for refining rocket designs and improving flight performance. Complementing these computational approaches, Bryson [18] developed a vertical wind tunnel specifically designed to predict rocket flight dynamics. This novel experimental setup allows for controlled testing of rocket models under varying wind conditions, offering a practical way to validate computational models of stability and control. Together, these studies illustrate the significant advancements in computational and experimental methods for analyzing rocket aerodynamics, enabling more precise predictions and effective design optimizations for complex aerospace systems.

1.2.8. High-Altitude and High-Speed Rocket Design

Research into the design of rockets capable of operating at high altitudes and speeds has seen significant advancements, particularly in the optimization of aerodynamic and structural performance. Milne et al. [7] made notable contributions by developing a high-fidelity dynamics model for high-altitude rockets, focusing on optimizing their aerodynamic profiles to ensure stable and efficient flight. Their work involved using sophisticated simulations to predict the behavior of rockets under varying atmospheric conditions, enabling precise adjustments to the design that enhance performance in thin air environments typical of high altitudes. This approach allows for a more accurate understanding of how changes in rocket shape, fin configuration, and weight distribution affect flight dynamics, leading to more robust and reliable designs. Minotti [15] further expanded on this by integrating aeroelastic considerations into the design process, ensuring that

the structural integrity of the rocket is maintained even at extreme speeds and altitudes. Their methodology combines aerodynamic and structural analysis to predict and mitigate potential issues such as flutter and dynamic instability, which can compromise the rocket's performance and safety. These studies provide a comprehensive framework for designing rockets capable of performing optimally under the demanding conditions of high-altitude missions.

Addressing the challenges of high-speed flight, Famellos [10] and Silva [14] explored strategies for reducing drag and enhancing aeroelastic stability, two critical factors that influence the performance and safety of rockets at high velocities. Famellos investigated the use of base bleed units to reduce drag in high-power rockets operating at transonic speeds. By introducing controlled gas flow from the rear of the rocket to fill the wake region, they were able to minimize pressure drag and improve overall aerodynamic efficiency. This technique is particularly beneficial for rockets transitioning from subsonic to supersonic speeds, where drag can significantly impact fuel efficiency and stability. Meanwhile, Silva et al. focused on the aeroelastic dynamic stability of slender, spinning sounding rockets. Their research highlighted how structural flexibility and spin rates interact with aerodynamic forces, potentially leading to destabilizing effects such as bending torsion coupling and flutter. By identifying critical parameters for minimizing these adverse interactions, their study offers valuable insights for designing rockets that remain stable and controllable under high-speed conditions. Together, these studies advance the understanding of how to design high-speed, high-altitude rockets that are both aerodynamically efficient and structurally sound.

The studies reviewed provided a comprehensive overview of the advancements in rocket nose cone design, aerodynamic stability, drag reduction, and thermal management. The integration of computational and experimental methodologies has significantly enhanced the precision and reliability of performance predictions. Continued research in these areas will contribute to the development of more efficient and stable rocket designs, essential for both scientific and commercial aerospace applications.

1.3. Project Objective

The primary objective of this project is to enhance the aerodynamic efficiency of a 4-inch diameter supersonic rocket, targeting speeds of approximately Mach 1.5. This project will concentrate on the design, modeling, optimization, and simulation of the rocket's critical components, including the nose cone, fin configuration, fin shape, and overall airframe structure. This project will focus on validating the new optimized design through computational analysis and simulations, providing insights into its potential capabilities and advantages, rather than actual construction of the rocket. Additionally, the project will use oblique shock wave theory to theoretically conclude atmospheric and surface data such as pressure, temperature, density, and coefficient of drag. This data will be essential for comparing the simulated results with theoretical

measurements, to establish and confirm new standards in supersonic rocket design. For the application and benefit of rockets like supersonic interceptors and cruise missiles.

1.4. Methodology

To accomplish this computational approach, the project will evaluate and optimize the aerodynamic performance of a sounding rocket at Mach 1.5. The focus will be on the design, simulation, and analysis of three primary aerodynamic components: the nose cone, tail fins, and canards. Each component will be analyzed using computational fluid dynamics (CFD) simulations to assess its influence on drag, flow separation, and overall aerodynamic efficiency. The geometries of all configurations will be created using SolidWorks. Nose cone profiles will include ogive, von Kármán, and long ellipsoid shapes, each tested at fineness ratios ranging from 4:1 to 7:1. Fin designs will include clipped delta and trapezoidal profiles, while canards will be evaluated in both swept-back clipped delta and triangular delta configurations. All geometries will be imported into ANSYS Fluent, where structured quadrilateral meshes will be generated using ANSYS Meshing. Boundary layer refinement and proximity-based refinement will be applied to improve accuracy in critical flow regions, particularly around leading edges and areas prone to separation. Simulations will be conducted under compressible, steady-state, supersonic flow conditions at Mach 1.5, using a density-based solver. Air will be modeled as an ideal gas, with viscosity handled via the Sutherland model to account for temperature dependence. Flow fields will be analyzed through velocity and pressure contours, coefficients of drag, coefficient of pressure, and coefficient of skin friction will be calculated for each configuration. These CFD results will be evaluated to determine which geometry combinations minimize drag and promote aerodynamic stability under supersonic conditions.

2. Mathematical Model

2.1. Governing Equations

2.1.1. Continuity Equation

The continuity equation is a fundamental principle in fluid dynamics that ensures the conservation of mass within a control volume or flow field. It states that the rate of change of mass within a specified volume must equal the net flux of mass entering and leaving that volume. Compressibility of the flow causes the air density to change as the rocket interacts with the surrounding fluid, and the continuity equation helps capture these changes accurately.

$$\frac{\partial \rho}{\partial t} + \nabla * (\rho u) = 0 \tag{2.1}$$

At Mach 1.5, the flow is compressible; hence, the density is no longer constant-it varies significantly with pressure and temperature variations. In such a case, the moving rocket produces shock waves where changes in these properties become abrupt. The continuity equation ensures that these changes are accounted for properly by relating how the density changes with respect to time and space. For instance, as the rocket accelerates and encounters shock waves, the air downstream of the shock experiences a sharp increase in density. The continuity equation tracks these changes to ensure that the mass flowing into a given volume before the shock matches the mass flowing out after the shock, despite the density variations.

The continuity equation is also vital in modeling the behavior of the boundary layer that forms on the rocket's surface. In high-Reynolds number, turbulent flow, and the boundary layer will be thin but significantly affect the overall drag and heat transfer to the rocket. The continuity equation works with the momentum and energy equations to model how mass is transported through this thin layer, especially near points where the flow may separate from the surface, near the rocket fins.

2.1.2. Navier-Strokes Equations

The most prominent role among all in the determination of the behavior of airflow around a rocket is taken by the Navier-Stokes equations. A description of how the unsteady velocity field of a fluid develops under the action of internal and external forces, taking into consideration viscous effects, pressure gradients, and body forces such as gravity, is afforded by these equations. A rocket would encounter supersonic flows, for which the compressible form of the Navier-Stokes equations is needed to resolve such complex properties in aerodynamics: shock waves, turbulence, and boundary layer behavior at the surface of a rocket. Therefore, the compressible flow can be modelled by three kinds of conservation: conservation of mass, conservation of momentum, and conservation of energy.

$$\frac{\partial(\rho u)}{\partial t} + \nabla * (\rho u \times u) = -\nabla p + \nabla * \tau + \rho f \quad (2.2)$$

Under supersonic flow, the rocket experiences significant pressure gradients, especially near the nose cone, fins, and body where shock waves form. These pressure gradients result in aerodynamic forces such as lift and drag, which directly influence the rocket's stability and performance. The momentum conservation will be accounted for by the Navier-Stokes equations, which include all different forces: viscous stresses that turn out to be very important for skin friction drag, a highly valued component of the total aerodynamic drag of the rocket. Since the flow needs to be compressible at the supersonic speeds, then Navier-Stokes should include changes in air density, pressure, and temperature. These shock waves cause discontinuities in the flow, and equations are fundamental to predicting what such property changes would do to the aerodynamics performance of a rocket, particularly drag and stability. Turbulent flow is also expected at high Reynolds numbers, making the accurate modeling of turbulence critical.

2.1.3. Energy Equation

The energy equation is a component of the compressible Navier-Stokes equations, capturing how energy is conserved within the flow around the rocket at supersonic speeds. In this context, the equation accounts for changes in internal energy, kinetic energy, and potential energy due to work done by pressure forces, viscous stresses, and heat transfer through conduction and turbulence. At Mach 1.5, a significant portion of the energy in the flow is carried as kinetic energy, but when the rocket encounters shock waves, much of this kinetic energy is rapidly converted into internal energy, resulting in substantial temperature increases near the rocket's surface. These thermal effects, particularly in areas like the nose cone and leading edges of the fins, can lead to high temperatures that may affect the rocket's structural integrity. Properly applying the energy equation allows for accurate prediction of heat transfer and temperature distribution, which are essential considerations for material selection and thermal management.

$$\frac{\partial E}{\partial t} + \nabla * \big((E + p)u\big) = \nabla * (\tau * u) + \nabla * (k \nabla T) + f * u \quad (2.3)$$

2.2. Boundary Conditions

2.2.1. Inlet and Outlet Conditions

Inlet and outlet boundary conditions define the flow that enters and leaves the computational domain of the rocket, which will be tested at an altitude of 8,000 meters, which represents a typical operating altitude for surface-to-air missiles. A velocity inlet condition was applied at the domain inlet, maintaining a consistent freestream Mach number of 1.5. Flow parameters such as static pressure, temperature, and air density were adjusted based on standard atmospheric conditions corresponding precisely to this altitude. At the outlet boundary, a pressure outlet condition is taken with the static pressure values assigned for the atmospheric pressure at

the fixed altitude. For supersonic flow analysis, the Dirichlet and Neumann boundary conditions can be considered within the computational fluid dynamic models. The Dirichlet conditions are applied at the inflow to set the initial velocity and temperature while Neumann conditions can be applied at the outflow. Where the air flow within the domain can exit without the dependence of velocity or static pressure. These conditions also allow for the analysis of the shock waves on the surface.

Another inlet boundary condition considered was the pressure far-field condition. The pressure far-field boundary is particularly suitable for modeling external, compressible flows involving supersonic or transonic speeds, as it enables direct specification of Mach number, static pressure, and temperature at the domain boundary. This boundary condition assumes uniform freestream conditions at an infinite distance, effectively replicating an open atmospheric environment. Employing a pressure far-field inlet can simplify computational setup, especially when analyzing shock formation, aerodynamic interactions, and flow separation characteristics around supersonic bodies.

2.2.2. Laminar vs. Turbulent

Laminar flow is a fluid flow regime where the movement of particles occurs in smooth, parallel layers with minimal disruption between them. This steady motion makes the velocity vary uniformly. Each division of fluid moves at different velocities, the fastest one in the middle of the flow and the slowest near the edge. Laminar flow normally appears when the velocities are lower and the Reynolds number is low, where viscous forces predominate over inertial ones. Due to its inherent stability, the laminar flow produces reduced skin friction drag compared to turbulent flow, a phenomenon conducive to drag reduction. However, for supersonic flows encountered in high-velocity flow over a rocket, the generation of laminar flow is quite hard to achieve because even minor disruptions in the flow can generate transition to turbulence.

Turbulent flow is a chaotic flow regime that is characterized by rapid fluctuations and vortices which intensely mix the layers of the fluid. This normally develops at high Reynolds numbers when the inertial forces are much greater than the viscous forces, leading to instability and complex motion. In supersonic flows, such as those surrounding a rocket at Mach 1.5, the possibility of turbulence occurring is almost a certainty given the great speeds and sharp pressure gradients. Turbulent flow seriously increases skin friction drag and enhances heat transfer to the surface, possibly an increasing thermal load on the body of the rocket.

2.2.3. Wall Boundary Conditions

Application of the wall boundary condition to the surface of the rocket enforces the no-slip condition and maintains the air velocity relative to the surface of the rocket at zero. Accurate computations of the boundary layer developing along the rocket require this boundary condition, particularly at supersonic speeds where the contribution of skin friction drag becomes

considerable. The rapid flow interacting with the rocket surface exerts viscous forces in addition to the overall drag. Additionally, in regions such as the nose cone and fins, where shock waves may form and interact with the boundary layer, the wall condition helps capture the complex behavior of flow separation and aerodynamic forces. If thermal effects are considered, the wall condition also accounts for heat transfer to the rocket's surface due to high-speed flow, which can lead to substantial heating, especially near the leading edges.

2.3. Assumptions

2.3.1. Compressible Flow

At Mach 1.5, the flow of air around the rocket is within the supersonic regime; hence, the effects of compressibility are very pronounced due to the air flow being compressed into a corner. Since the pressure disturbances produced by the motion of the rocket cannot generate upstream at a speed greater than that of the vehicle, it results in the generation of oblique shock waves. The shock waves are accompanied by sudden changes in pressure, temperature, and density of air around the rocket. Neglecting compressibility would result in incorrect estimates of the drag and lift forces; besides, it would also misrepresent the location and strength of the corresponding shock waves. Therefore, there is a need to solve the full compressible form of the Navier-Stokes equations, which includes variations of air density and pressure to represent the actual aerodynamics of the flying rocket at supersonic speeds.

2.3.2. Steady State Flow

In many aerodynamic analyses, assuming steady-state flow simplifies the problem by focusing on conditions where the flow properties: velocity, pressure, and density do not change with time. For this design, the steady-state assumption may be valid for analyzing the rocket in level flight at a constant velocity, far from transitional events such as shock wave formation or turbulent boundary layer separation. However, this assumption will need to be revisited for transient singularities, like rapid changes in angle of attack or during transitions between different flight regimes. For the steady-state regions of flight, this assumption reduces the complexity and computational cost of the simulations.

2.3.3. 2D Flow

The computational simulations performed in this analysis utilize a two-dimensional (2D) flow model, significantly simplifying aerodynamic computations while preserving accuracy in critical flow features. Although rocket components such as fins, nose cones, and body geometries inherently exhibit three-dimensional aerodynamic behaviors, a carefully constructed 2D model can effectively capture essential characteristics like pressure distribution, drag, and flow separation along the surfaces. The two-dimensional approach assumes flow uniformity along the third

dimension (spanwise direction), reducing computational costs without sacrificing detailed analysis of critical aerodynamic interactions.

2.3.4. Supersonic Flow Characteristics

Supersonic flow introduces unique aerodynamic occurrences that are absent in subsonic flow. The formation of shock waves causes sudden changes in the flow properties, such as pressure and velocity, which can result in significant increases in drag (wave drag) and thermal loads. Furthermore, boundary layer separation due to adverse pressure gradients behind the shock waves can lead to complex flow features like vortices and recirculation zones, especially near the fins and afterbody. These occurrences complicate the prediction of forces and moments, yet they are of primary importance for rocket stability and control. The accurate capturing of these characteristics will be highly instrumental to the improvement in design of the rocket and in ensuring that it maintains aerodynamic efficiency and stability during supersonic flight.

2.3.5. Ideal Gas Law

The assumption of an ideal gas simplifies the relationship between pressure, density, and temperature in the flow around the rocket. In supersonic conditions, air behaves similarly to an ideal gas because the intermolecular forces and deviations from ideality are relatively small compared to the magnitude of aerodynamic forces. The ideal gas law, a straightforward way to link these quantities, enabling the calculation of density from pressure and temperature fields in the CFD model. This assumption is particularly useful when dealing with compressible flow, where changes in pressure and temperature significantly affect air density.

$$pV = nRT \tag{2.4}$$

2.4. Non-Dimensional Parameters

2.4.1. Reynolds Number

The Reynolds number is a dimensionless parameter that describes the nature of the flow surrounding the rocket, notably with respect to the intensity of inertial forces relative to viscous forces. This value is very important in defining the flow regime, whether laminar or turbulent, around the rocket. For Mach 1.5, it is expected that Reynolds number will be high; hence, the flow is generally turbulent. This affects the boundary layer development, and the skin friction drag experienced by the rocket. A high Reynolds number signifies that inertial forces dominate over viscous forces, leading to more complex flow field such as flow separation and turbulence, particularly in regions like the fins and near shock wave interactions.

$$Re = \frac{\rho u L}{\mu} = \frac{uL}{v} \tag{2.5}$$

$$v = \frac{\mu}{\rho} \tag{2.6}$$

2.4.2. Mach Number

The Mach Number (M) describes compressibility effects due to the air flow around the rocket. The vehicle is designed to cruise at Mach 1.5; hence, it belongs to the supersonic flow regime where compressibility effects are essential. In that area, shock waves form around the nose cone and fins. Pressures, temperatures, and densities change abruptly. The Mach number governs how these shock waves form and generates, influencing the overall aerodynamic forces on the rocket. As Mach numbers increase, wave drag becomes more pronounced, and the behavior of the flow field shifts, requiring careful consideration in both the design and optimization phases to ensure stability and performance at these high speeds.

$$M = \frac{u}{a} \tag{2.7}$$

$$a = \sqrt{\gamma RT} \tag{2.8}$$

2.5. Turbulence Model

The turbulence model plays a crucial role in effectively replicating the complicated dynamics of turbulent flow surrounding the rocket at supersonic velocities. Considering the elevated Reynolds numbers linked to Mach 1.5, it is anticipated that the flow will exhibit complete turbulence, especially in nearness to the rocket's surface, where boundary layer occurrence are significant. To efficiently characterize this behavior, the Reynolds-Averaged Navier-Stokes (RANS) methodology is utilized in conjunction with an appropriate turbulence model to simulate the influence of turbulence on the mean flow dynamics. For this analysis, models such as k-ε or k-ω SST are evaluated due to their ability to accurately represent both near-wall characteristics and large-scale flow separation, especially in areas such as the nose cone and fins where interactions between shocks and the boundary layer are of considerable importance. These models help simulate the action of turbulence upon aerodynamic forces, hence giving much better predictions of drag, skin friction, and heat transfer. Direct resolution of the full Navier-Stokes equations for turbulent flows, also called Direct Numerical Simulation (DNS), involves huge computational resources.

2.6. Numerical Solution Methods

The numerical solution method utilizes a density-based solver, which is well-suited for capturing the compressible flow conditions around the rocket at Mach 1.5. This solver is specifically designed for scenarios where density variations significantly affect the flow field, such

as supersonic flows with shock waves. By directly solving the density and pressure fields, the density-based solver accurately models the compressibility effects that are critical for determining aerodynamic forces, pressure distributions, and temperature changes on the rocket's surface. To account for the temperature-dependent nature of air viscosity at high speeds, the Sutherland model is applied. This model provides a more precise viscosity calculation by adjusting for temperature changes due to shock heating and frictional effects in the boundary layer. Using the Sutherland model is needed for realistic predictions of skin friction drag and heat transfer, especially in high-temperature zones near the nose cone and fins. Additionally, air is modeled as an ideal gas to simplify the relationship between pressure, density, and temperature. This assumption captures the compressible behavior of air at supersonic speeds, where changes in pressure and temperature considerably influence density.

3. Computational Approximation

3.1. Mesh Generation

3.1.1. Structured vs. Unstructured

Mesh selection plays a crucial role in computational fluid dynamics because it determines how accurately the flow characteristics can be captured while balancing computational efficiency. Structured meshes are defined by their grid-like arrangement, where elements are uniformly spaced and systematically aligned. This regularity simplifies how nodes are connected, making these meshes computationally efficient and easier to use in solvers. Geometries that match this orderly grid structure such as the ogive, von Karman, and ellipsoid nose cones, as well as the fins and canards are especially well-suited to structured meshes. However, structured meshes can require significant preprocessing to fit more complex or irregular geometries, which is where unstructured meshes excel. Unstructured meshes use irregularly shaped elements, such as triangles, that adapt more naturally to intricate or curved surfaces. While flexible, this adaptability comes with higher computational costs and greater solver complexity due to the irregular connectivity of nodes.

For aerodynamic components experiencing supersonic flow at Mach 1.5, structured meshes align well with the smooth, predictable surfaces of these shapes. The structured layout allows for precise representation of shock waves and boundary layer occurrences in critical regions like the leading edges of fins, canards, and nose cones. Due to these meshes being regular, they simplify solver operations and provide a high degree of accuracy in areas with sharp gradients, such as where shock waves form. This alignment between the geometry and the mesh structure makes structured meshes an efficient and reliable choice for simulating these aerodynamic components.

The aerodynamic components, including the ogive, von Karman, and ellipsoid nose cones, along with the clipped delta fin, trapezoidal fin, swept-back clipped delta canard, and delta canard, are particularly well-suited to structured meshes. These components have streamlined profiles, and the leading edges are areas where significant flow occurrences, such as shock waves and flow separation, occur. Structured meshes enable precise control over the distribution of nodes in these high-gradient areas, allowing for a detailed analysis of flow behavior and the capture of subtle boundary layer effects. Refining the mesh near the edges of the components ensures the accuracy of the results while maintaining efficiency by keeping the resolution coarser in less critical regions.

Structured meshes are also advantageous for analyzing turbulence and flow separation, both of which directly affect drag and aerodynamic performance. Their uniform grid layout ensures smooth transitions between nodes, minimizing numerical objects that could distort calculations of drag coefficients. Additionally, the structured nature of the mesh allows for better refinement in regions of interest, such as the leading edges of fins and the curvature of nose cones,

where the interaction of airflow is most critical. By choosing structured meshes, the simulation can focus on accurately capturing aerodynamic forces while maintaining efficient computation. This makes structured meshes an excellent option for improving the understanding of flow behavior and optimizing the design of these components for supersonic performance.

3.1.2. Mesh Element Shapes

The choice of mesh element shapes is fundamental in computational fluid dynamics as it dictates how well the simulation captures flow behavior around complex geometries. For simulating supersonic airflow at Mach 1.5 around the aerodynamic components such as the ogive, von Karman, and ellipsoid nose cones, as well the fins and canards, quadrilateral elements are particularly advantageous. These elements, characteristic of structured meshes, form a regular, grid-like pattern that aligns effectively with the smooth and streamlined profiles of these components. Their uniformity allows for precise calculation of flow properties, especially in regions where linear gradients dominate, such as along the boundary layer or at the stagnation points of the nose cone. Quadrilateral elements are not only efficient but also inherently stable, reducing computational errors when simulating high-speed flows.

The benefits of quadrilateral elements extend beyond their alignment with geometric features. These elements can achieve a high level of accuracy with fewer nodes compared to triangular elements, making them highly efficient in terms of computational resources. This efficiency is particularly valuable when analyzing shock waves and boundary layer behavior, where a high resolution is essential. Quadrilateral elements excel at capturing flow phenomena in regions of sharp gradients, such as the leading edges of fins and canards. By refining the quadrilateral elements in these critical zones, the mesh ensures detailed and accurate resolution of flow properties like pressure, velocity, and density. Outside these regions, coarser quadrilateral elements maintain computational efficiency while still providing reliable data in less critical areas of the flow field. While quadrilateral elements are ideal for most of the aerodynamic components, triangular elements may also be employed in specific situations. Triangles are particularly useful in transitional zones where the geometry becomes irregular or when a structured grid transitions into areas that require unstructured meshing.

3.1.3. Boundary Layer Refinement

Boundary layer refinement plays a pivotal role in computational fluid dynamics, especially for aerodynamic components operating under supersonic conditions. The boundary layer is a thin region near the surface where the flow velocity transitions sharply from zero at the wall to freestream conditions. Accurate resolution of this region is essential because it governs critical aerodynamic behaviors, such as skin friction, pressure gradients, and flow separation. To capture these phenomena effectively, a refined mesh with high node density near the surface is required. This ensures that the steep velocity and pressure gradients within the boundary layer are resolved, allowing for precise calculation of aerodynamic forces and flow behavior. Structured meshes,

which allow for systematic and gradual refinement, are particularly advantageous in resolving the details of boundary layers along streamlined geometries.

For the components of the rocket that are considered, boundary layer refinement is essential to capture occurrences such as shock wave interaction, turbulence generation, and flow detachment. High-resolution mesh elements placed strategically along the surfaces improve the simulation's ability to calculate key parameters, such as wall shear stress and heat transfer rates, which are critical in supersonic flows. By maintaining a small y+ value, the mesh ensures that the first grid point lies within the viscous sublayer, enabling accurate application of turbulence models. This level of refinement allows the simulation to capture subtle flow features that contribute to drag reduction and minimize flow separation.

3.1.4. Mesh Quality

Mesh quality is a decisive factor in determining the accuracy and stability of CFD simulations, particularly for high-speed aerodynamic analyses. One of the primary parameters to consider is the element aspect ratio, which quantifies the ratio of an element’s longest dimension to its shortest. In regions such as the boundary layer, where velocity and pressure gradients are steep, elements with high aspect ratios aligned parallel to the flow direction are preferred. This orientation ensures accurate resolution of shear stresses and minimizes numerical diffusion. However, excessively high aspect ratios in other regions can degrade solution quality by introducing interpolation errors and instability. Structured meshes are inherently advantageous in controlling aspect ratios, as they allow consistent alignment with flow patterns around components like the ogive and von Karman nose cones or the clipped delta fins. Ensuring optimal aspect ratios across the domain reduces errors in the computed aerodynamic coefficients, such as drag.

Another critical parameter is element distortion, which measures how much an element deviates from its ideal geometric configuration. High levels of distortion, particularly in regions of sharp curvature or abrupt geometry transitions, can adversely affect numerical accuracy and convergence rates. Maintaining low distortion is essential in areas of complex flow interaction, such as the leading edges of fins or nose cones, where supersonic flow creates high-intensity gradients. Smoothness, defined by the gradual transition of element sizes, further ensures that rapid changes in cell size do not disrupt solver performance or introduce artificial flow features.

3.1.5. Mesh Refinement

Curvature-based refinement is a strategy for generating a mesh that accurately represents the geometry of aerodynamic components with curved or complex surfaces. Supersonic flow around the considered components requires precise representation to capture local flow behavior. By refining the mesh in areas of high curvature, smaller and more densely packed elements conform closely to the geometry, minimizing approximation errors. This refinement is particularly

important for regions like leading edges and fin tips, where accurate resolution ensures proper modeling of pressure gradients, shock wave interactions, and boundary layer behavior.

Proximity-based refinement focuses on resolving flow behavior in areas where surfaces are close together or interact. This method adjusts the mesh resolution based on the distance between adjacent surfaces, such as the narrow gaps between fins and the airframe or the regions where canards meet the rocket body. In these proximity zones, local flow patterns often include sharp velocity and pressure gradients that require detailed resolution. By placing finer mesh elements in these critical areas, proximity-based refinement ensures the accurate capture of flow occurrence like wake formation, vortex shedding, and turbulent interactions. At the same time, this approach avoids excessive mesh density in areas where detailed resolution is unnecessary, maintaining computational efficiency. Proximity refinement allows for a well-balanced mesh, optimizing accuracy and performance in simulations of supersonic flows.

3.2. Geometry Modeling of Aerodynamic Components

3.2.1. Nose Cone

3.2.1.1. Ogive

The selected nose cone designs encompass four variations of ogive shapes, each defined by aspect ratios ranging from 4:1 to 7:1. These aspect ratios determine the length of the nose cone relative to its 4-inch diameter. The lengths of the nose cones are 16.0 inches, 20.0 inches, 24.0 inches, and 28.0 inches for aspect ratios of 4:1, 5:1, 6:1, and 7:1, respectively. The curvature for each configuration increases with the aspect ratio, with the 4:1 design having a curvature of 65.0 inches, the 5:1 design at 101.0 inches, the 6:1 design at 145.0 inches, and the 7:1 design at 197.0 inches. These values define the smoothness of the ogive profile.

However, the geometry of the ogive curvature resulted in a leading edge that was too sharp, which posed challenges for computational modeling. The sharp edge made it difficult to generate a structured mesh without errors or failures during the meshing process. To address this issue, a half model of the nose cones was used when meshing. This modification not only allowed the structured mesh to succeed but also ensured that the computational fluid dynamics (CFD) simulations could proceed without numerical instabilities caused by overly fine or irregular mesh elements near the sharp edge. Each nose cone was placed within an air domain measuring approximately 100 inches in length and 50 inches in width. The air domain features a rounded inlet, facilitating smooth airflow entry to minimize numerical instability and accurately capture flow behavior. This setup allows for precise analysis of aerodynamic performance, including pressure distribution, flow separation, and shock wave behavior.

$$\rho = \frac{r^2 + L^2}{2 * r} \tag{3.1}$$

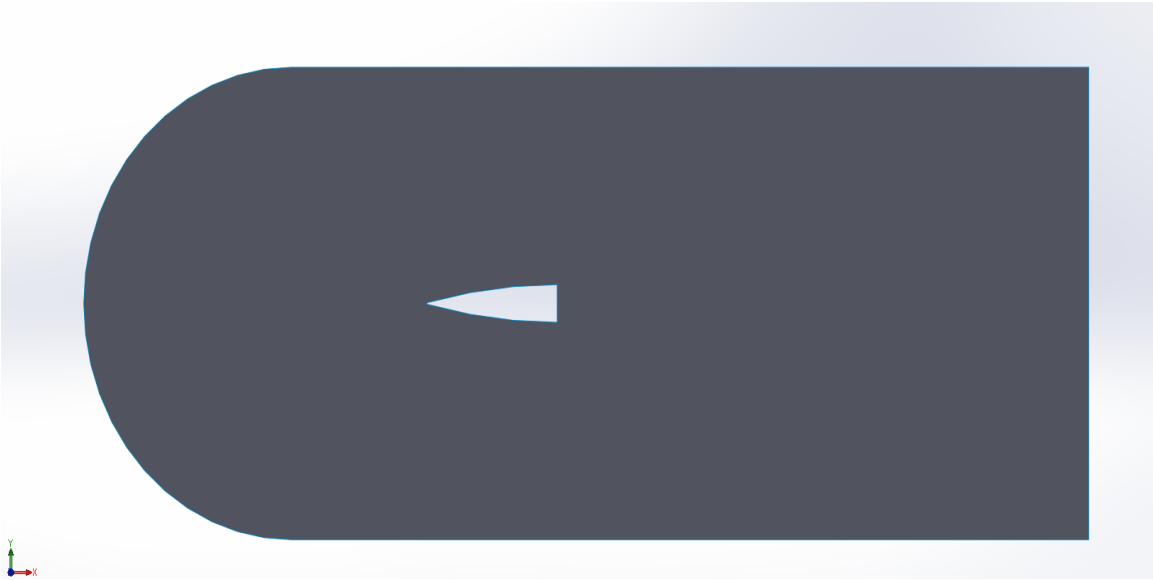

Figure 3.1 – Geometry and domain of ogive 4:1.

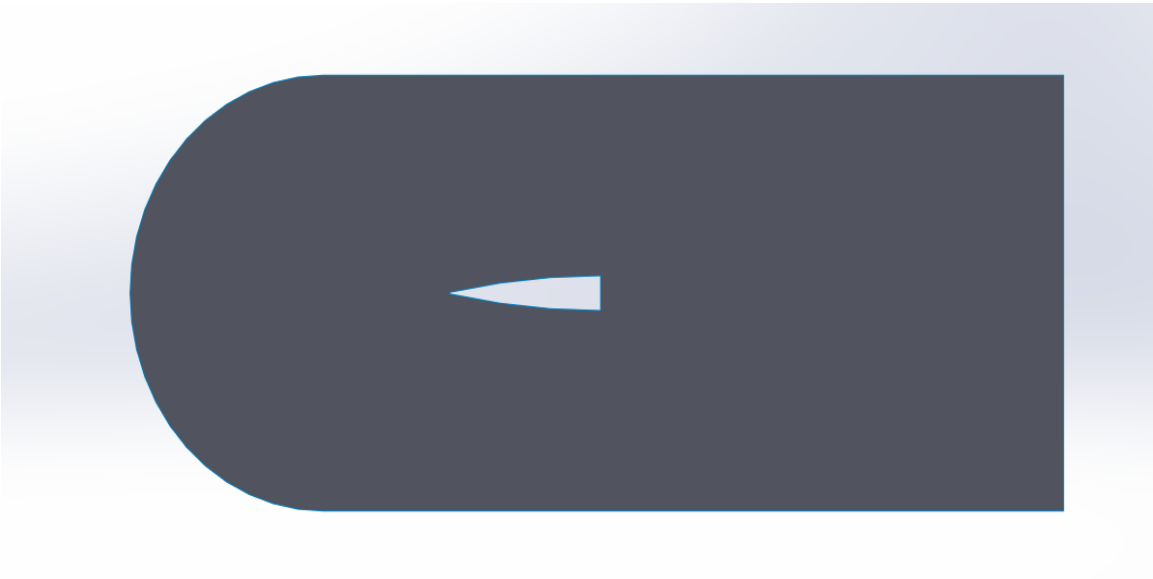

Figure 3.2 – Geometry and domain of ogive 5:1.

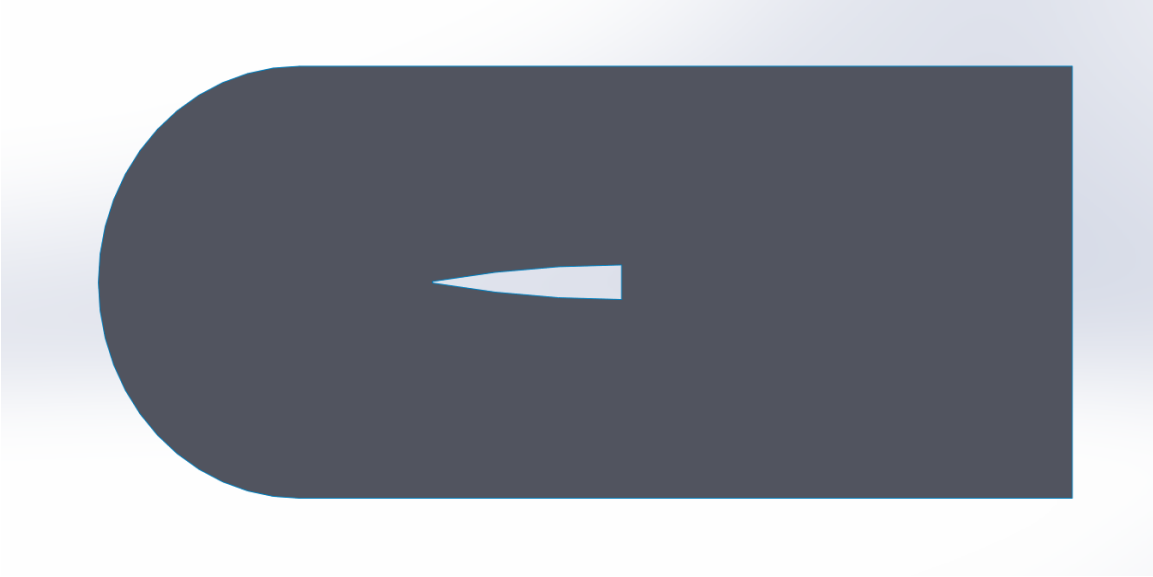

Figure 3.3 – Geometry and domain of ogive 6:1.

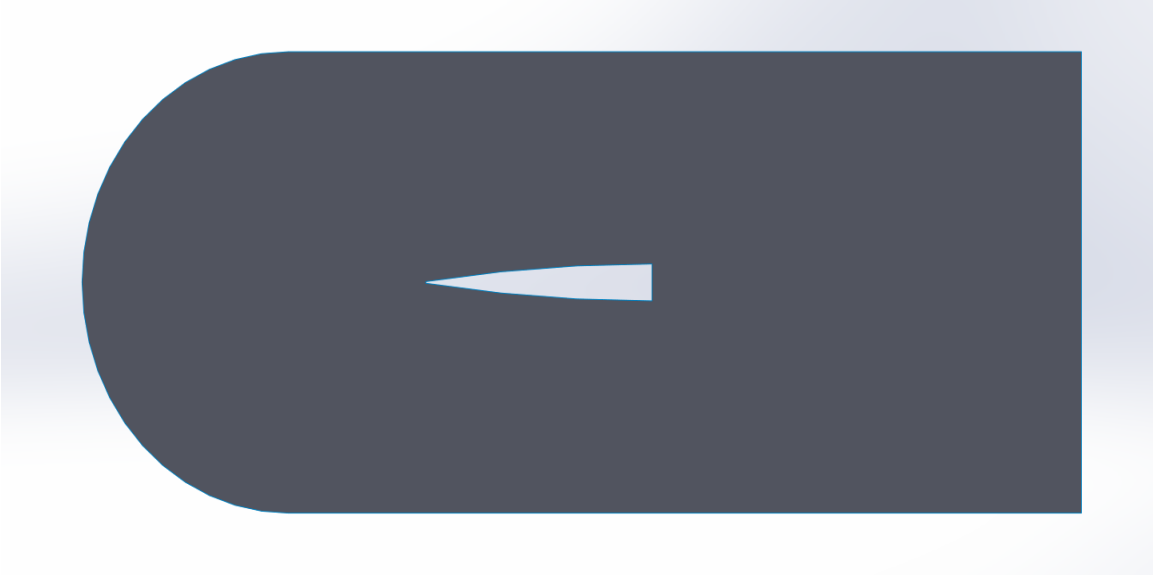

Figure 3.4 – Geometry and domain of ogive 7:1.

3.2.1.2. Von Karman

The Von Kármán nose cones were designed with aspect ratios of 4:1, 5:1, 6:1, and 7:1, consistent with the lengths used for the ogive nose cones. Unlike the ogive profiles, the curves of the Von Kármán nose cones were derived using the mathematical equation associated with the Von Kármán curve profile, which is optimized for minimizing drag in supersonic and transonic flows. The curve profile is defined by the relationship between the nose cone's length and diameter in the governing equation. The curvature of each nose cone was generated using an equation-driven

curve in SolidWorks, with the profile explicitly defined and bounded by the full length of each nose cone. The diameter, another key variable, defines the base of the curve, while the profile equation ensures continuity and smooth flow attachment across the surface. To analyze their aerodynamic performance, the Von Kármán nose cones were modeled within an air domain identical to that used for the ogive and long ellipsoid designs.

$$y(x) = \frac{2}{\sqrt{\pi}} * \sqrt{\arccos\left(1 - \frac{2x}{L}\right) - \frac{\sin\left(2 * \arccos\left(1 - \frac{2x}{L}\right)\right)}{2}} \quad (3.2)$$

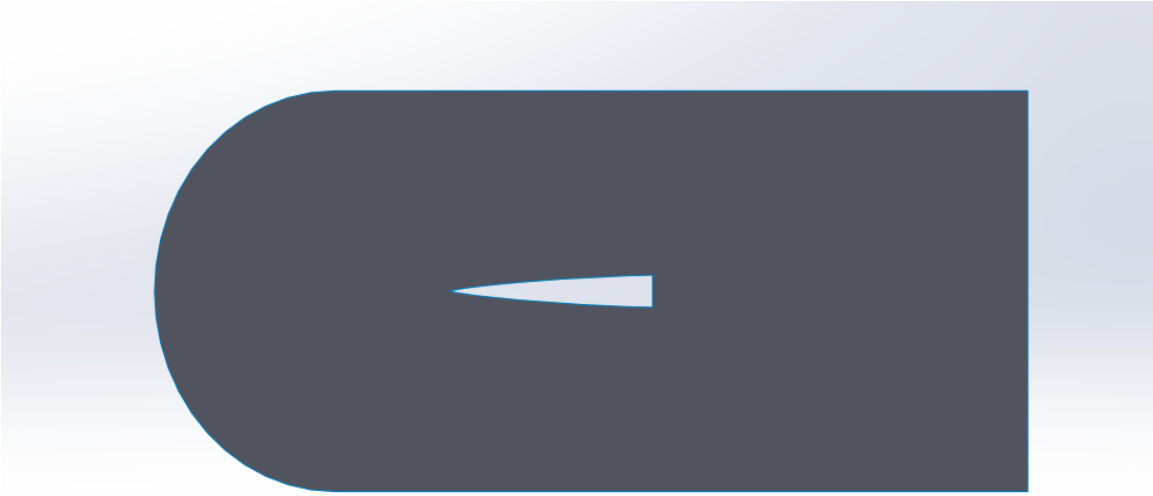

Figure 3.5 – Geometry and domain of von Karman 7:1.

Figure 3.6 – Geometry and domain of von Karman 6:1.

Figure 3.7 – Geometry and domain of von Karman 5:1.

Figure 3.8 – Geometry and domain of von Karman 4:1.

3.2.1.3. Long Ellipsoid

The design of the long ellipsoid nose cones was based on four aspect ratios: 4:1, 5:1, 6:1, and 7:1. These ratios defined the lengths of the nose cones like the other profiles and the long ellipsoid had the same 4-inch diameter. The curvature of each nose cone was generated using an equation-driven curve in SolidWorks, with the ellipsoid profile explicitly defined and bounded by the full length of each nose cone. The ellipsoid curve equation incorporates several dependent

variables, with the length of the nose cone playing a central role in defining the extent of the taper. Longer lengths result in a more elongated curve, providing a gradual transition that ensures smooth airflow attachment and minimizes flow disturbances. The diameter serves as a constraint for the base of the profile, while the explicit equation ensures precision in generating the symmetric and streamlined shape.

$$y = 2 * \sqrt{1 - \frac{(x-L)^2}{L^2}} \tag{3.3}$$

Figure 3.9 – Geometry and domain of long ellipsoid 4:1.

Figure 3.10 – Geometry and domain of long ellipsoid 5:1.

Figure 3.11 – Geometry and domain of long ellipsoid 6:1.

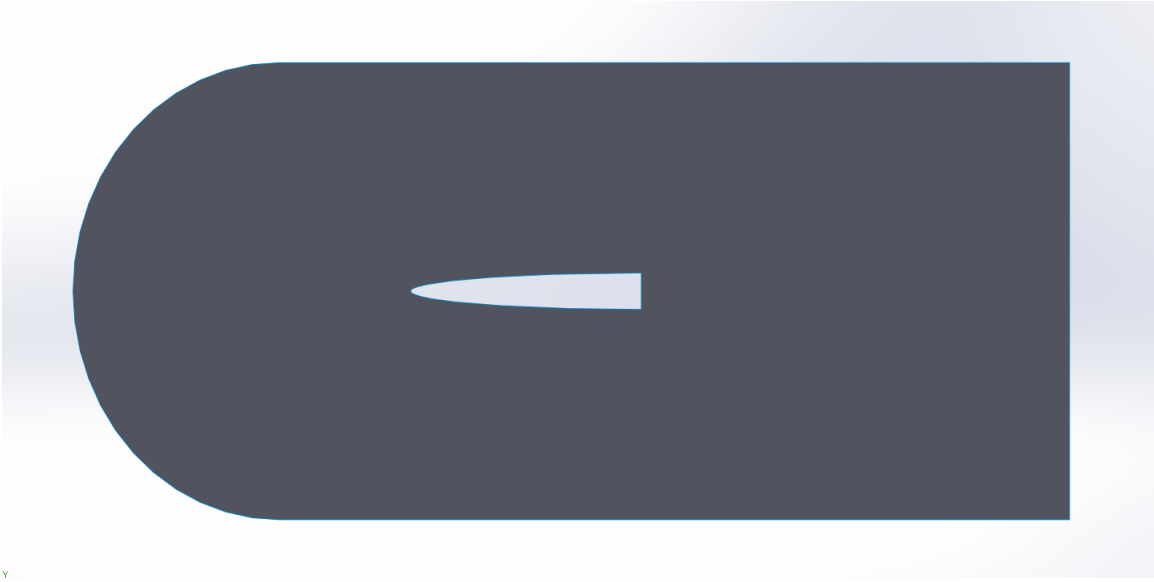

Figure 3.12 – Geometry and domain of long ellipsoid 7:1.

3.2.2. Tail Fins

The tail fin features a clipped delta configuration with a root chord of 12.00 inches, tip chord of 2.08 inches, and a vertical span of 1.75 inches. This geometry enhances aerodynamic stability and minimizes induced drag by reducing tip vortices during supersonic flight. A deflection angle of 10 degrees was selected to provide sufficient control authority without generating excessive aerodynamic loads or causing boundary-layer separation. The chosen angle offers an optimal balance, ensuring effective stability and maneuverability throughout the flight envelope.

The second clipped delta tail fin geometry is defined by a root chord of 12.00 inches, a tip chord of 5.47 inches, and a vertical span of 1.75 inches. The fin is set at a deflection angle of 15 degrees, providing increased aerodynamic control required for more aggressive maneuvering and trajectory corrections. Although a greater deflection angle inherently raises aerodynamic loading and the potential for flow separation, 15 degrees was selected as an optimal compromise to ensure sufficient maneuverability without significantly degrading performance. This angle ensures stable and effective flight control under demanding flight conditions at higher Mach numbers.

Figure 3.13 – Geometry and domain of clipped delta fin at 10 degrees.

Figure 3.14 – Geometry and domain of clipped delta fin at 15 degrees.

The second tail fin configuration features a trapezoidal geometry, characterized by a 12.00-inch root chord, 3.00-inch tip chord, and a span of 1.35 inches. Trapezoidal fins are particularly effective at supersonic conditions because their tapered geometry reduces shock-induced drag, which can significantly affect overall vehicle performance. Additionally, the trapezoidal shape maintains structural simplicity, making it easier to manufacture and integrate onto the vehicle body. With a moderate deflection angle of 10 degrees, this geometry allows smoother flow attachment along the fin surfaces, decreasing the likelihood of adverse shock-wave interactions. These geometric choices collectively support stable, predictable fin performance at high-speed flight conditions, ultimately aligning with the aerodynamic objectives of minimizing drag.

The next trapezoidal tail fin configuration has a root chord of 12.00 inches, a tip chord of 3.00 inches, and a vertical span of 1.35 inches, positioned at a deflection angle of 15 degrees. At a deflection of 15 degrees, geometry promotes more pronounced aerodynamic interactions, beneficial for scenarios demanding rapid maneuvering capabilities. While this higher angle slightly increases aerodynamic loading, it strategically leverages the trapezoidal design's structural simplicity to accommodate the increased stresses without compromising efficiency.

Figure 3.15 – Geometry and domain of trapezoidal fin at 10 degrees.

Figure 3.16 – Geometry and domain of trapezoidal fin at 15 degrees.

3.2.3. Canards

The first canard configuration features a swept clipped delta geometry defined by a root chord of 6.00 inches, tip chord of 0.91 inches, vertical span of 1.00 inch, and a leading-edge sweeping angle of 60 degrees. The clipped delta shape combined with significant sweep reduces shock-induced drag and delays aerodynamic flow separation, enhancing performance in supersonic flight regimes. Positioned at a moderate deflection angle of 10 degrees, this canard effectively provides lift and moment control without introducing excessive structural stress or turbulent airflow. The smaller span dimension is particularly advantageous, as it limits aerodynamic interference and reduces induced drag.

The second swept clipped delta canard configuration has a root chord of 6.00 inches, tip chord of 2.85 inches, a vertical span of 1.00 inch, and a leading-edge sweep angle of 60 degrees. This geometry leverages the aerodynamic benefits of high sweep angles, particularly at increased deflection angles such as 15 degrees. At this deflection, the canard produces more substantial aerodynamic forces suitable for rapid pitch corrections and stability adjustments in supersonic flight. The clipped delta shape efficiently manages shock formation, helping maintain attached flow even at more aggressive deflections.

Figure 3.17 – Geometry and domain of swept back clipped delta canard at 10 degrees.

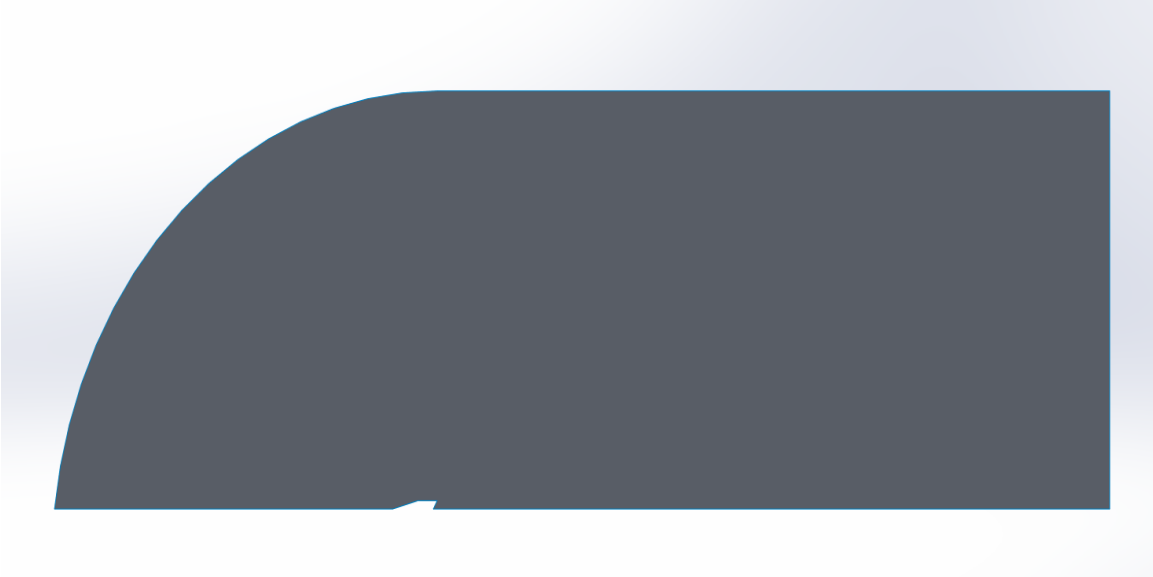

Figure 3.18 – Geometry and domain of swept back clipped delta canard at 15 degrees.

The delta canard geometry includes a root chord of 6.00 inches tapering uniformly to a sharp tip, with a vertical span of 1.06 inches. Delta configurations are particularly advantageous at supersonic conditions due to their inherent aerodynamic stability, effective shock-wave management, and ability to maintain attached flow across their surfaces. Positioned at a moderate 10-degree deflection angle, this geometry promotes steady aerodynamic forces, minimizing potential flow separation issues associated with larger deflections. The sharp, tapered geometry significantly reduces induced drag and structural complexity.

The second delta canard design incorporates a root chord length of 6.00 inches with a span measuring 1.61 inches. This geometry effectively manages higher aerodynamic loads at the chosen deflection angle of 15 degrees, enabling precise control during aggressive pitch maneuvers.

Figure 3.19 – Geometry and domain of delta canard at 10 degrees.

Figure 3.20 – Geometry and domain of delta canard at 15 degrees.

3.3. Mesh Modeling of Aerodynamic Components

3.3.1. Nose Cone Meshing

To streamline computational fluid dynamics (CFD) simulations and enhance accuracy, the nose cone geometries ogive, Von Kármán, and ellipsoid were represented by symmetric half-models rather than complete geometries. Given the inherent symmetry of these shapes, modeling only half of the nose cone significantly simplified the computational effort while preserving accuracy, especially along the axis of symmetry. Each two-dimensional half-geometry was imported into ANSYS Fluent's DesignModeler, where initial geometry segmentation took place. Typically, the geometry was divided into three distinct faces: one face encompassing the curved profile of the nose cone, and two additional faces behind the trailing edge, which allowed more effective meshing control across the computational domain.

A structured meshing strategy was consistently applied across all nose cone models to maximize mesh quality and numerical stability during CFD simulations. Although face meshing was initially considered to achieve quadrilateral-dominant cells, the necessity of accurately resolving boundary-layer flows required the inclusion of inflation layers. Consequently, the meshing procedure relied heavily on edge sizing commands in ANSYS Fluent, using a bias factor of 10 to achieve optimal cell distribution. This bias approach strategically positioned smaller mesh elements directly adjacent to the nose cone surface, gradually transitioning to larger elements farther into the computational domain, effectively capturing detailed boundary-layer occurrences and flow gradients.

The element sizing within the structured mesh was uniformly maintained at a general dimension of 0.0015 meters, balancing computational efficiency with accurate resolution of aerodynamic features. Meshes consistent of around 35,000 to 50,000 cells.This uniform element size facilitated precise capture of crucial flow characteristics, particularly near the leading edge and across regions experiencing steep gradients in velocity or pressure. Importantly, this structured meshing methodology prevented unintended geometric alterations at the sharp tip of the nose cone, maintaining the original curvature and geometry throughout the meshing process.

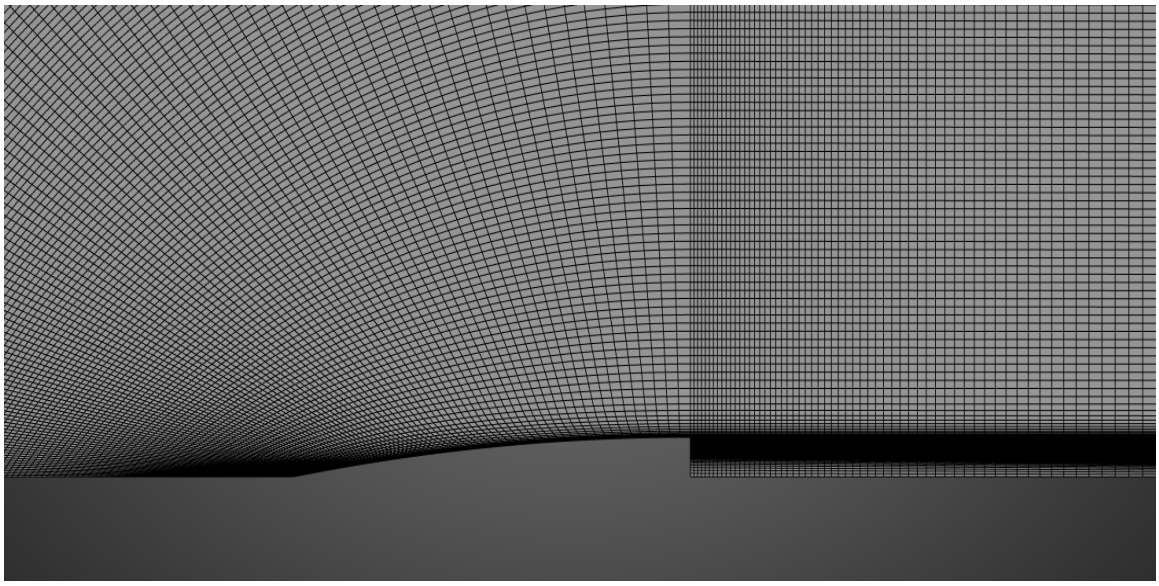

Figure 3.21 – Structured mesh of ogive 7:1.

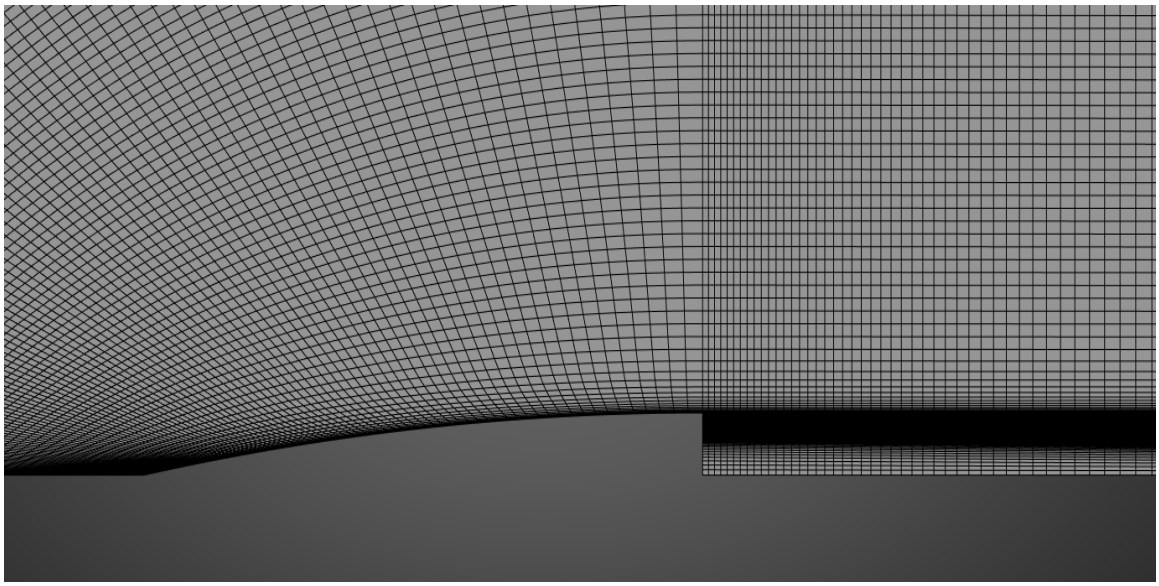

Figure 3.22 – Structured mesh of ogive 6:1.

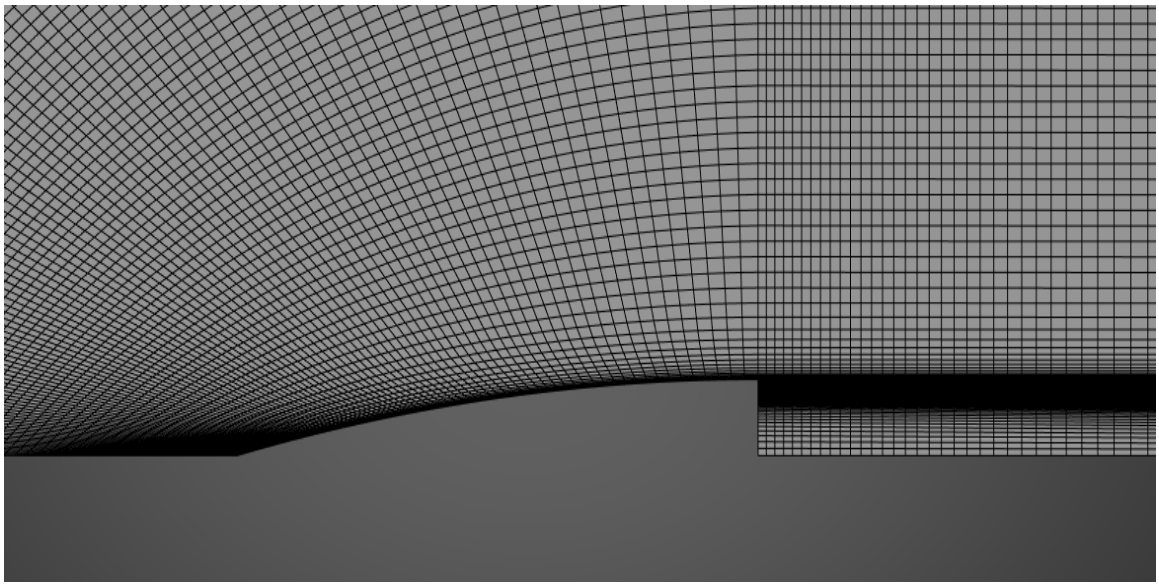

Figure 3.23 – Structured mesh of ogive 5:1.

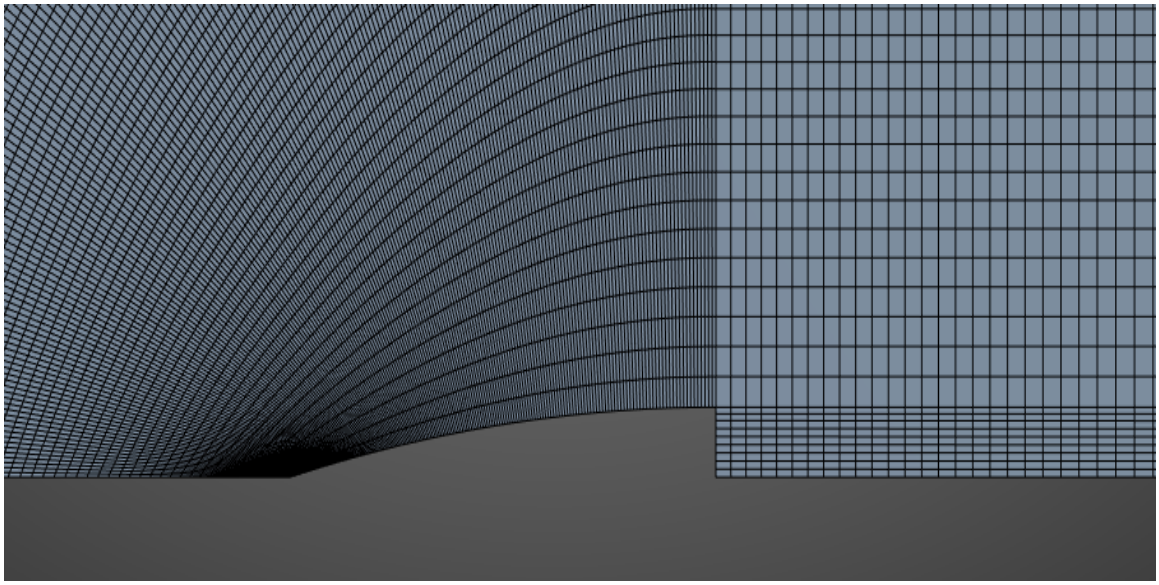

Figure 3.24 – Structured mesh of ogive 4:1.

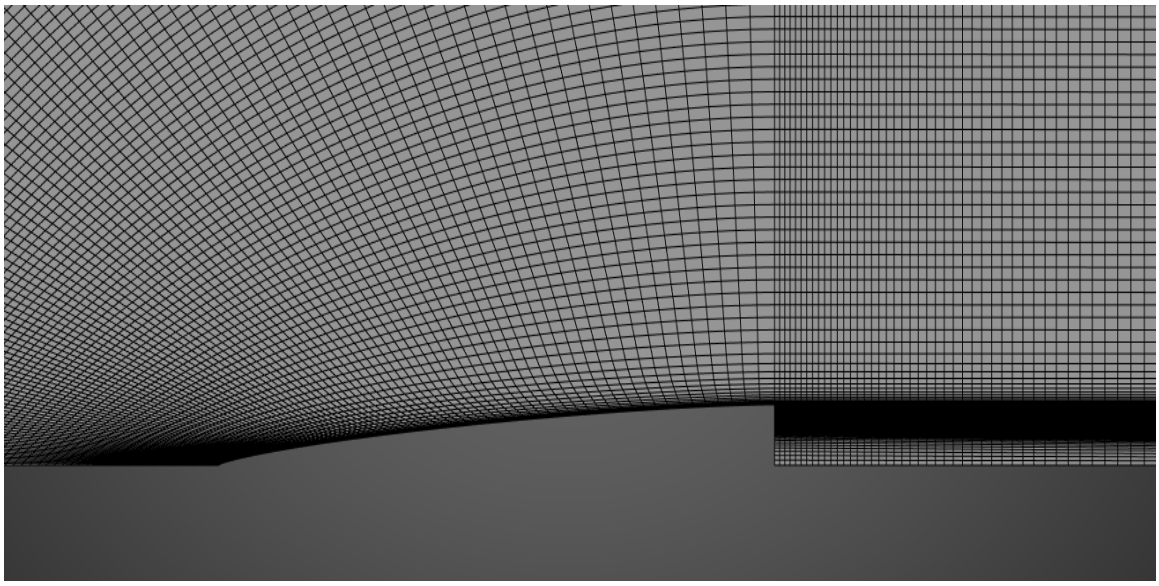

Figure 3.25 – Structured mesh of von Karman 7:1.

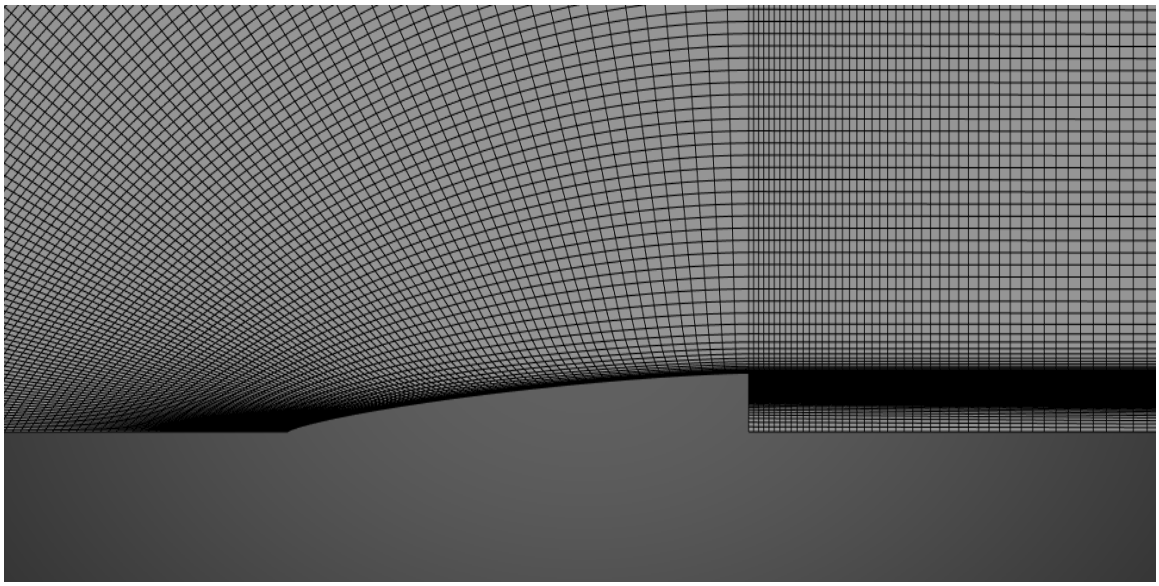

Figure 3.26 – Structured mesh of von Karman 6:1.

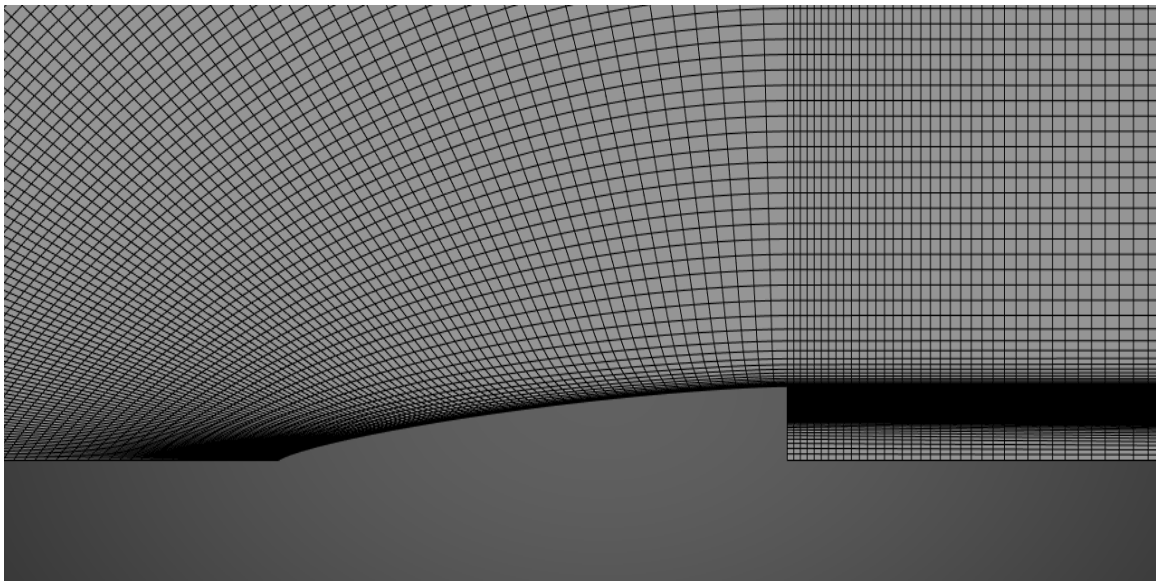

Figure 3.27 – Structured mesh of von Karman 5:1.

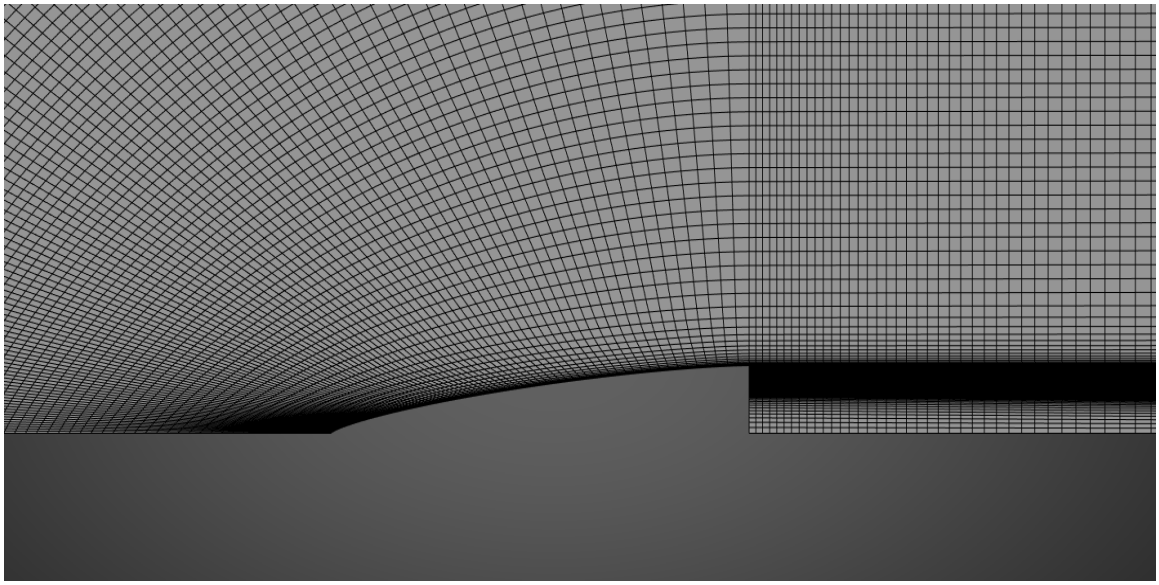

Figure 3.28 – Structured mesh of von Karman 4:1.

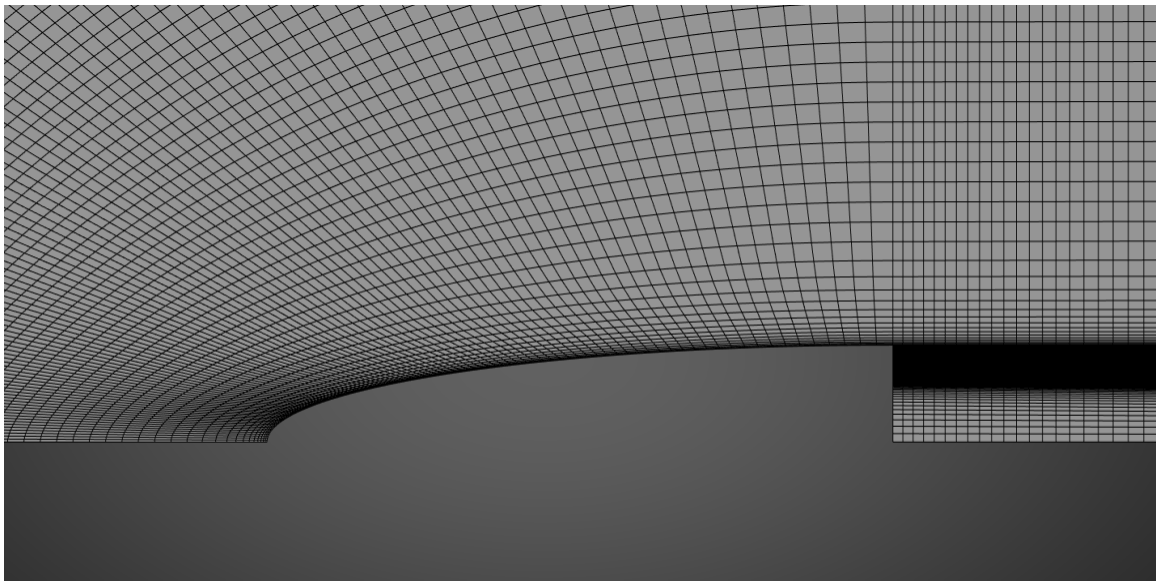

Figure 3.29 – Structured mesh of long ellipsoid 4:1.

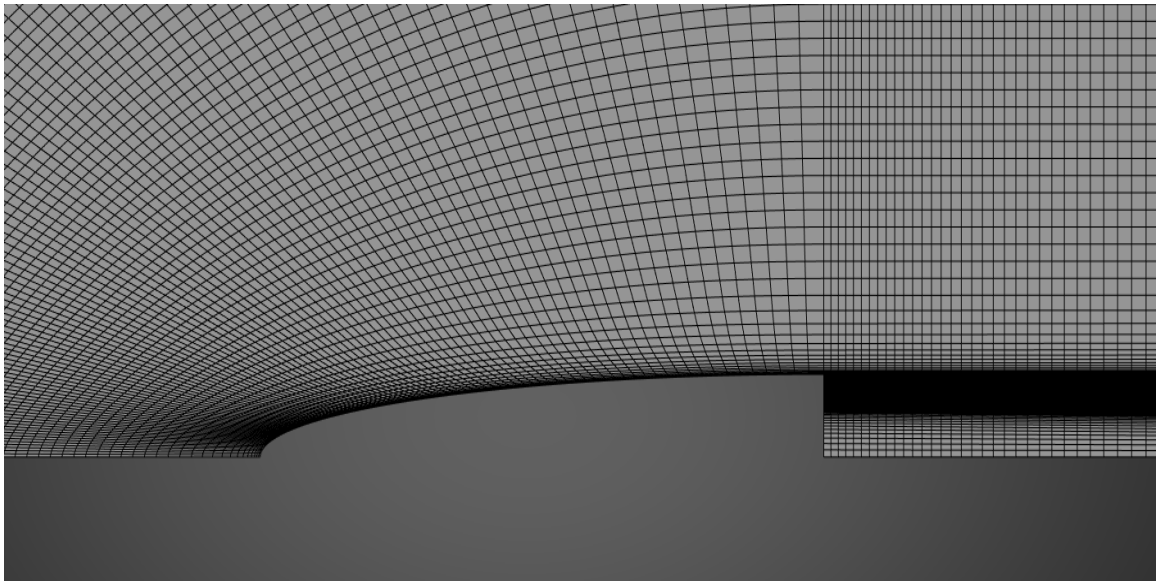

Figure 3.30 – Structured mesh of long ellipsoid 5:1.

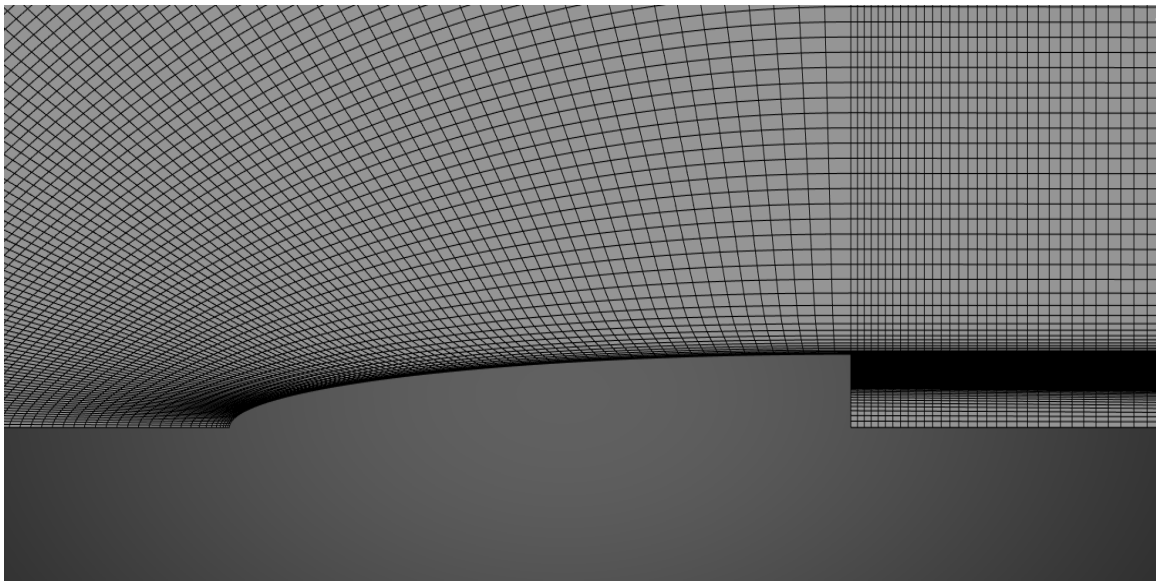

Figure 3.31 – Structured mesh of long ellipsoid 6:1.

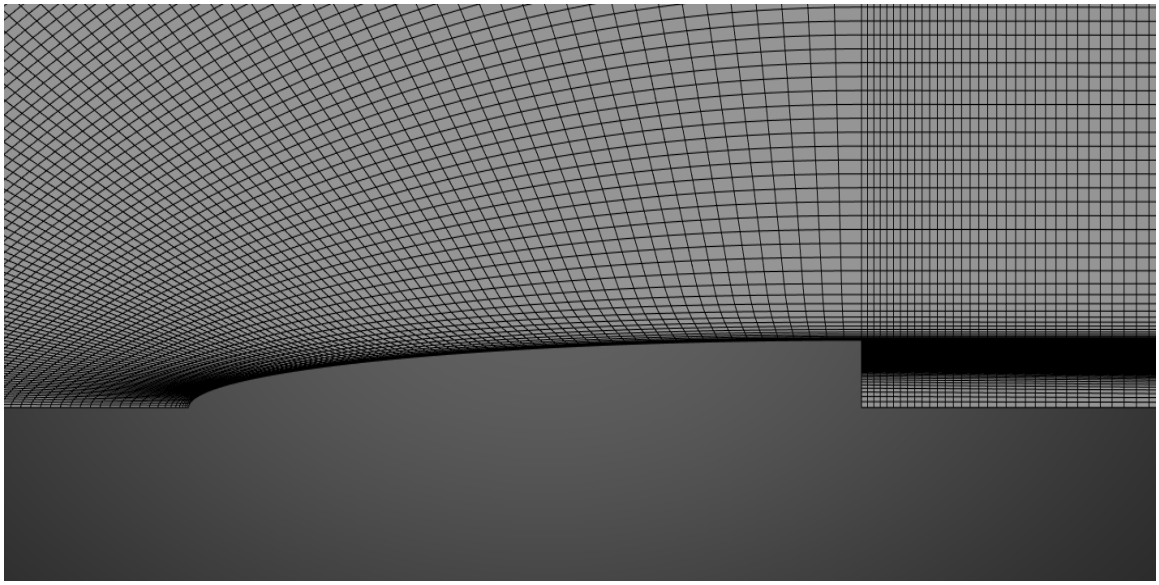

Figure 3.32 – Structured mesh of long ellipsoid 7:1.

3.3.2. Tail Fin and Canards Meshing

The tail fins and canards were meshed using a structured approach consistent with the nose cones. However, these geometries were meshed as complete, two-dimensional profiles without symmetry simplifications, due to the inherent asymmetry introduced by their deflection angles. After importing each geometry into ANSYS Fluent's DesignModeler, the geometry was carefully segmented into four distinct faces. Specifically, segmentation included one face covering the primary aerodynamic surface of each fin or canard, a second face aligned with the horizontal span,

and two additional faces positioned behind the trailing edge to facilitate controlled mesh refinement.

Structured meshes were generated primarily through edge-sizing techniques combined with a bias factor, effectively capturing critical boundary-layer occurrence. Edge sizing with a bias of 10 was specifically employed to cluster smaller mesh elements near the aerodynamic surfaces, providing fine resolution at the leading edges and along the span of each fin and canard. Just like the nose cones, the face meshing command was commonly used to develop the structured mesh further. Away from these surface regions, mesh elements gradually increased in size, ensuring computational efficiency while accurately resolving flow gradients across the domain. To maintain consistency across simulations, a general element size of 0.0015 meters was applied uniformly throughout the tail fin and canard meshes. Meshes consistent of around 30,000 to 45,000 cells.

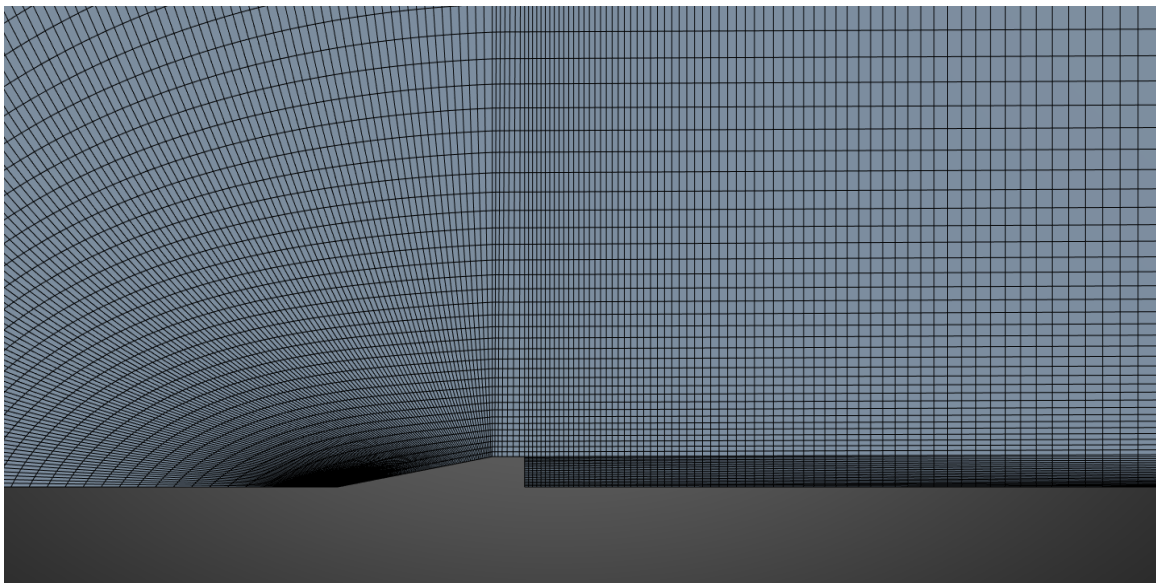

Figure 3.33 – Structured mesh of clipped delta fin at 10 degrees.

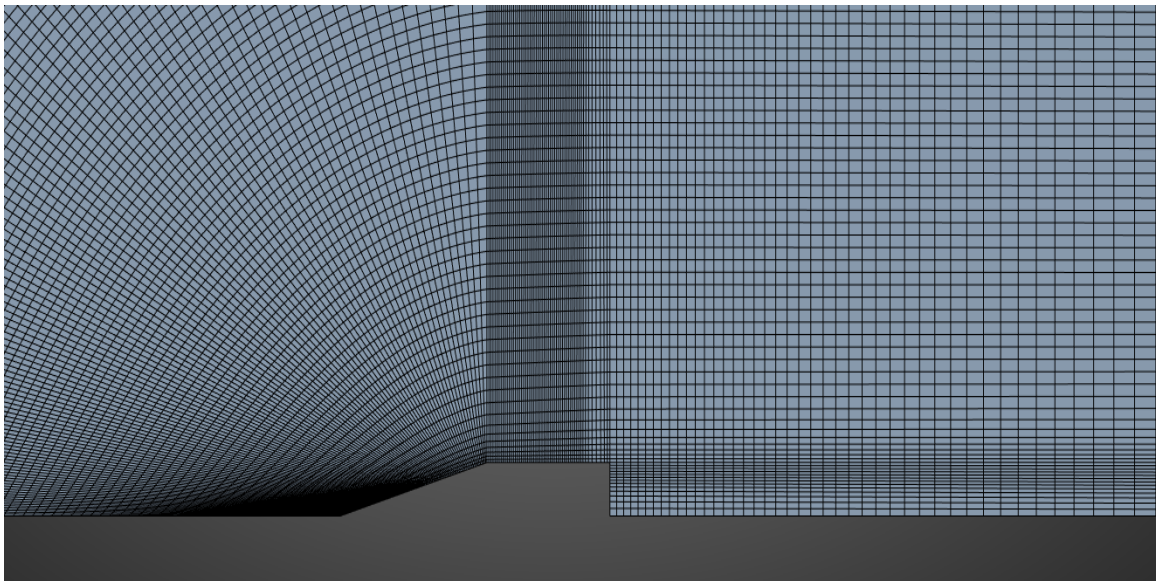

Figure 3.34 – Structured mesh of clipped delta fin at 15 degrees.

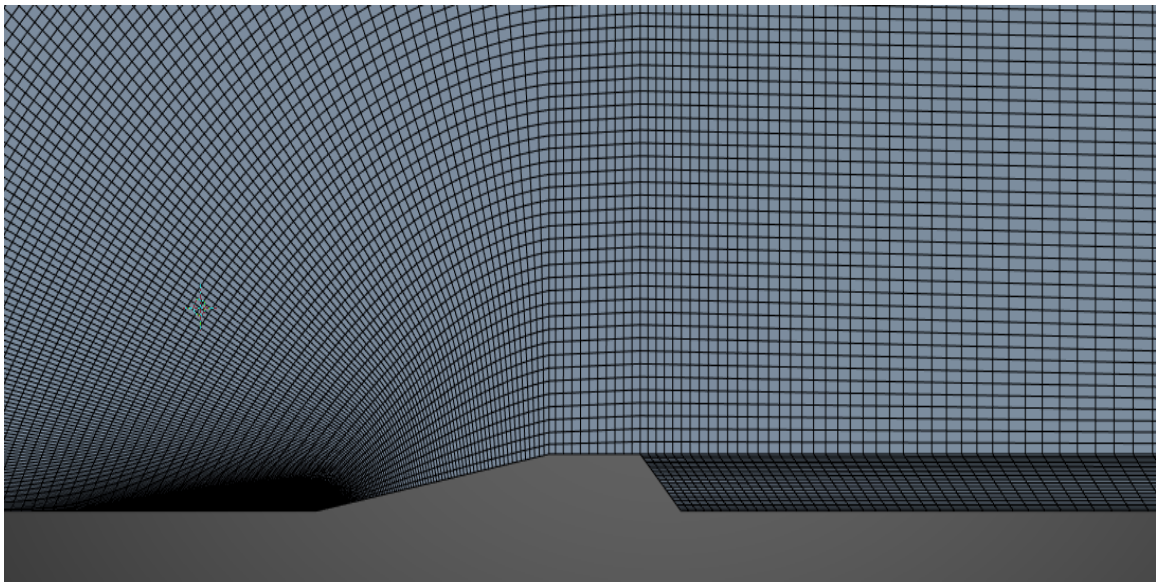

Figure 3.35 – Structured mesh of trapezoidal fin at 10 degrees.

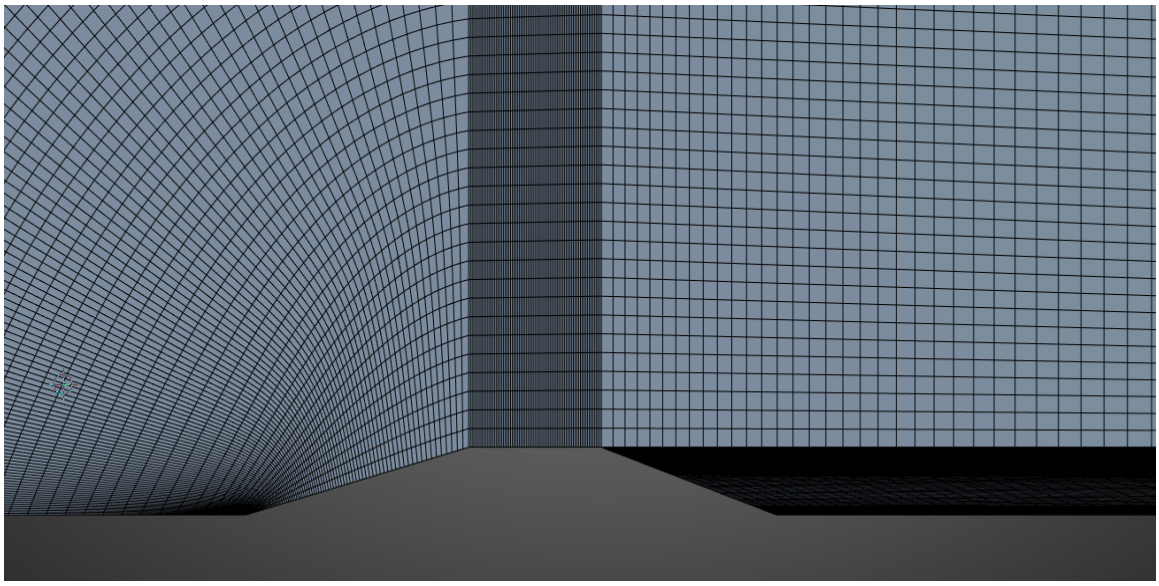

Figure 3.36 – Structured mesh of trapezoidal fin at 15 degrees.

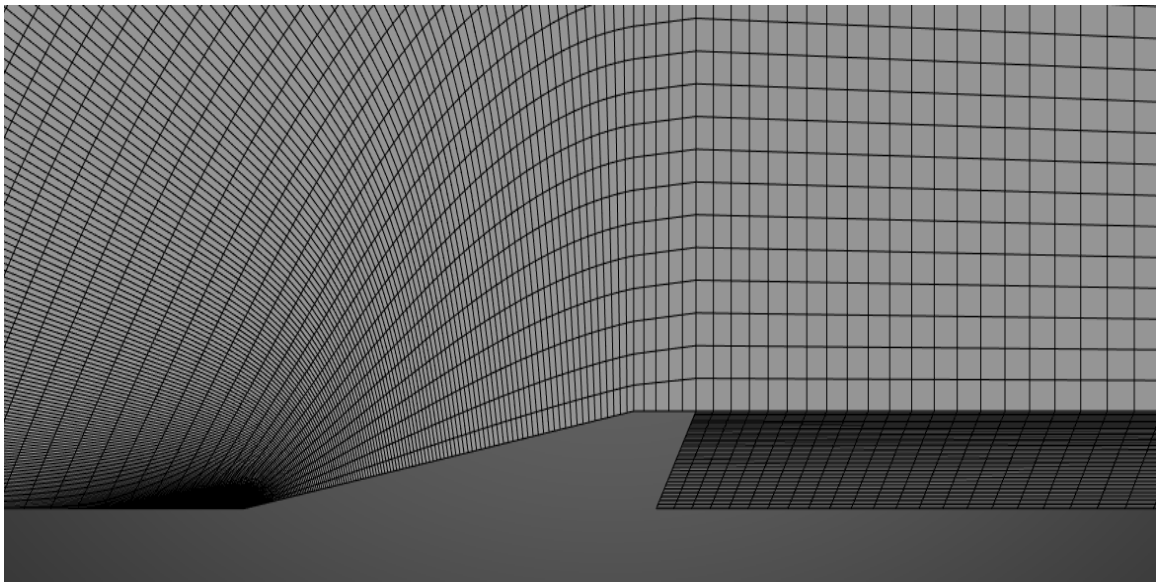

Figure 3.37 – Structured mesh of swept back clipped delta canard at 10 degrees.

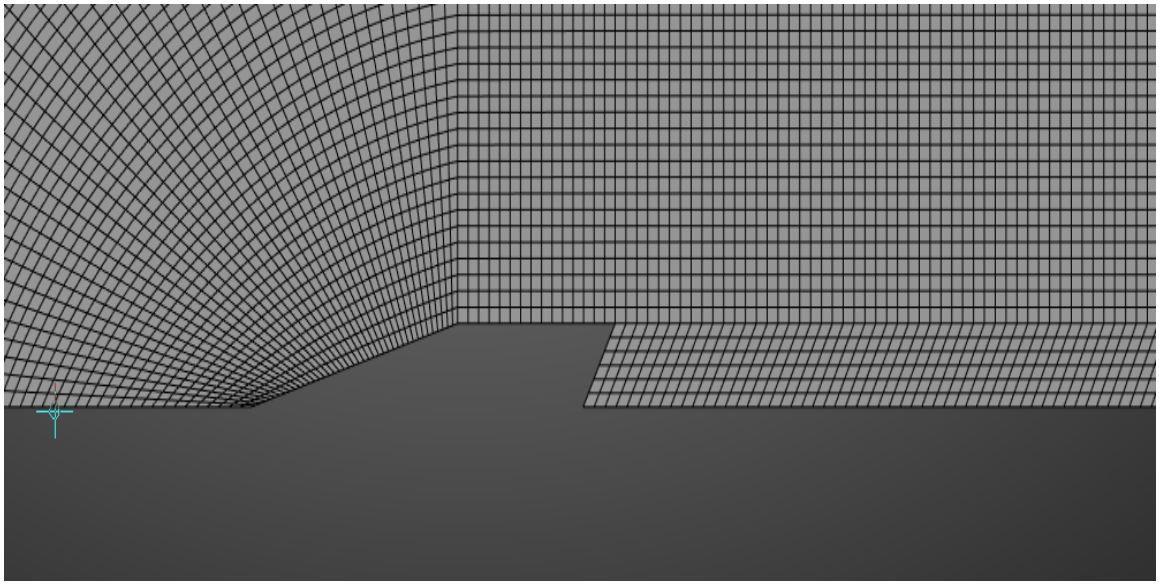

Figure 3.38 – Structured mesh of swept back clipped delta canard at 15 degrees.

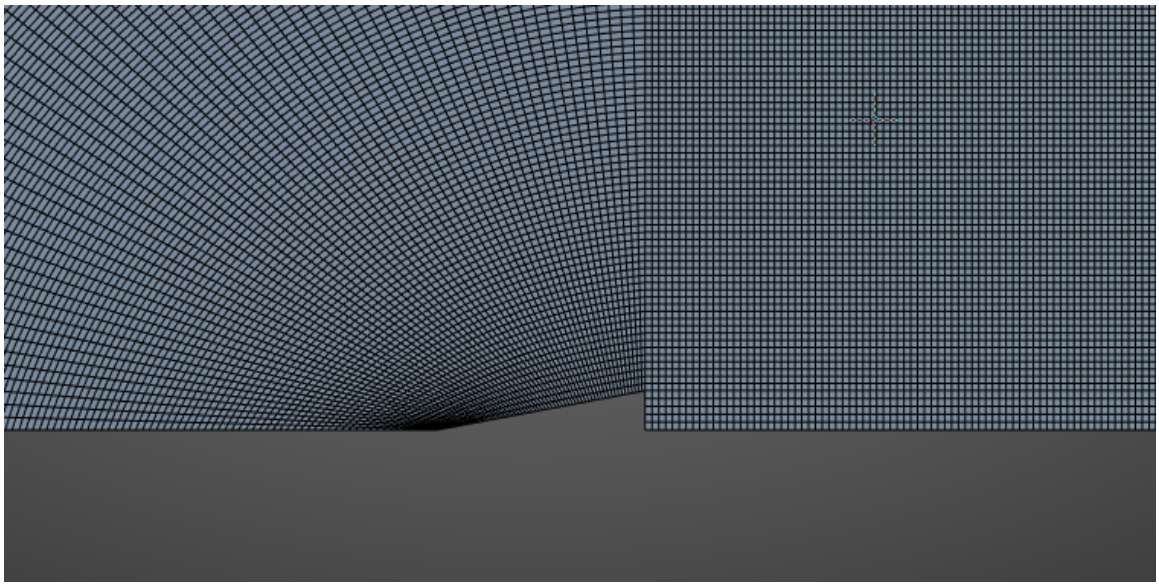

Figure 3.39 – Structured mesh of delta canard at 10 degrees.

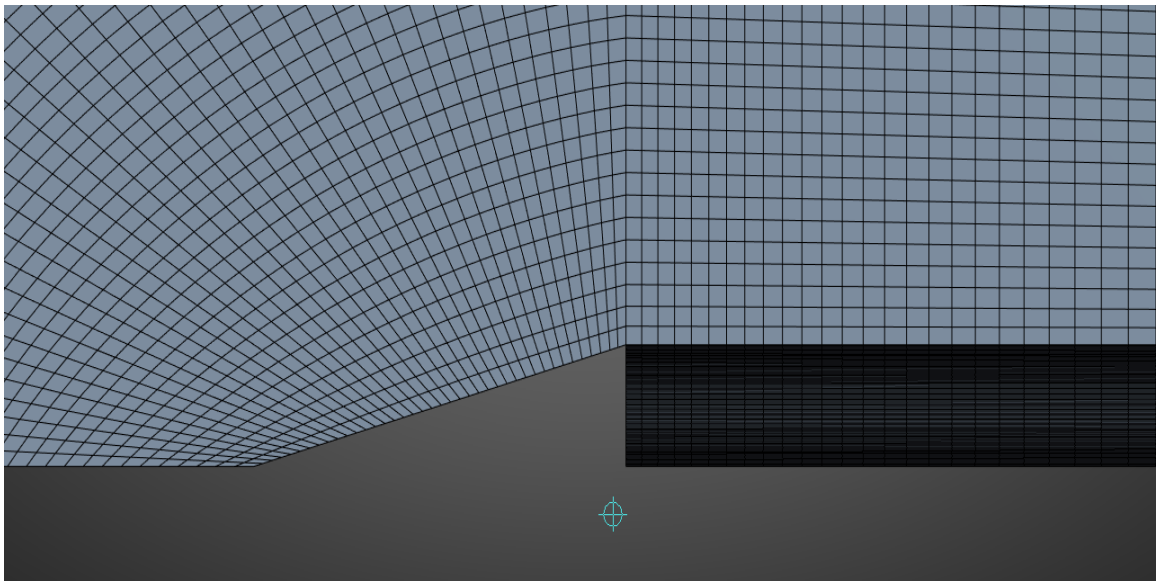

Figure 3.40 – Structured mesh of delta canard at 15 degrees.

4. Results of Nose Cone, Fin, and Canard Configurations

4.1. 2D Nose Cone Configuration

Table 4.1 – Computational coefficient of drag.

Coefficient of Drag				
	4:1	5:1	6:1	7:1
Ogive	0.10841456	0.095556958	0.090639115	0.090163797
Von Karman	0.096390589	0.086652991	0.067121092	0.08456966
Long Ellipsoid	0.14079696	0.12417062	0.11657441	0.11393639

Table 4.2 – Computational coefficient of pressure.

Coefficient of Pressure				
	4:1	5:1	6:1	7:1
Ogive	0.012242555	0.021326524	0.016530678	0.013437491
Von Karman	0.03822825	0.027638075	0.013716244	0.017755391
Long Ellipsoid	0.01384339	0.0092962855	0.0068772586	0.0053958024

Table 4.3 – Computational coefficient of skin friction.

Coefficient of Skin Friction				
	4:1	5:1	6:1	7:1
Ogive	0.0027832035	0.0033286352	0.0032155402	0.0031365988
Von Karman	0.0034300935	0.0032944351	0.0026281776	0.0031217207
Long Ellipsoid	0.0031815406	0.0030792578	0.0030072981	0.0029502234

Table 4.4 – Length and area table.

Length			
28 in	24 in	20 in	16 in
0.7112 m	0.6096 m	0.5080 m	0.4064 m
Cross Sectional Area			
0.00811 m^2			

Testing Altitude: 8,000 Meters
Mach: 1.5

U.S. Standard Atmosphere Air Properties:

- Temperature: -36.94 C to 236.21 K
- Total Temperature: 342.50 K
- Gravity: 8.782 m/s^2
- Absolute Pressure: 35,650 Pa
- Total Pressure: 130872.24 Pa
- Gauge Pressure: 95222.24
- Gauge Total Pressure: 29,547 Pa
- Density: 0.5258 kg/m^3
- Dynamic Viscosity: 1.527e-5 kg/ m*s
- Mach at altitude: 461 m/s

4.1.1. Ogive Nose Cone

The aerodynamics efficiency of an ogive nose cone is strongly influenced by its fineness ratio, which represents the length to diameter proportion. As the ratio increases, the coefficient of drag generally decreases due to the more streamlined shape reducing flow separation and minimizing pressure drag. At a 4:1 fineness ratio, the drag coefficient is approximately 0.1084, but as the ratio extends to 7:1, it drops to 0.0902, indicating improved aerodynamic performance. However, beyond a certain length, the reduction in drag becomes marginal, suggesting that the benefits of increasing the fineness ratio diminish.

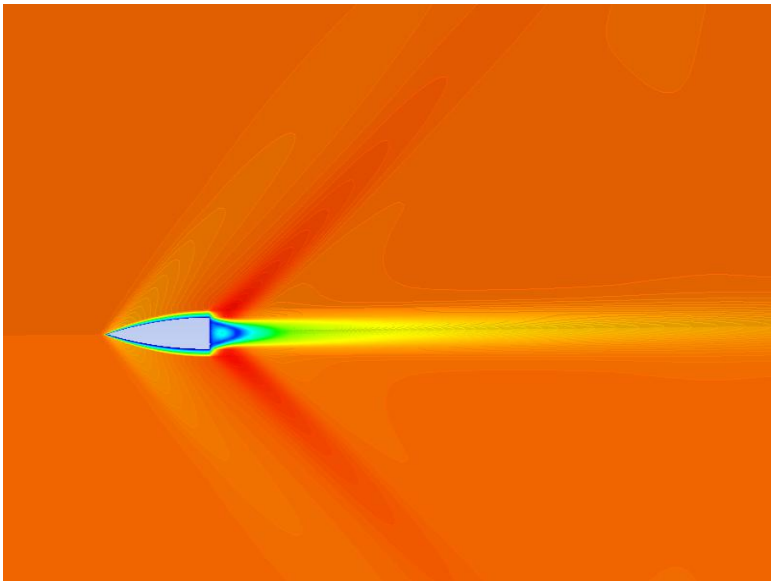

Figure 4.1 – Velocity contour of 4:1 ogive.

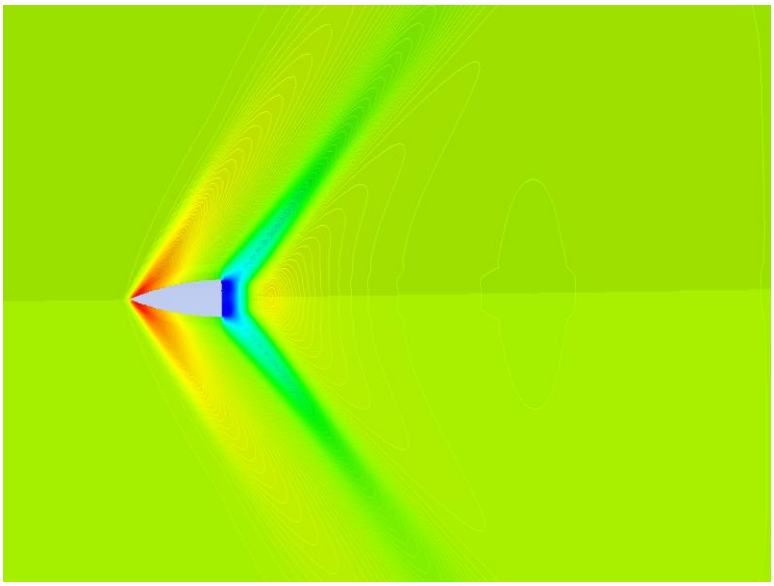

Figure 4.2 - Pressure contour of 4:1 ogive.

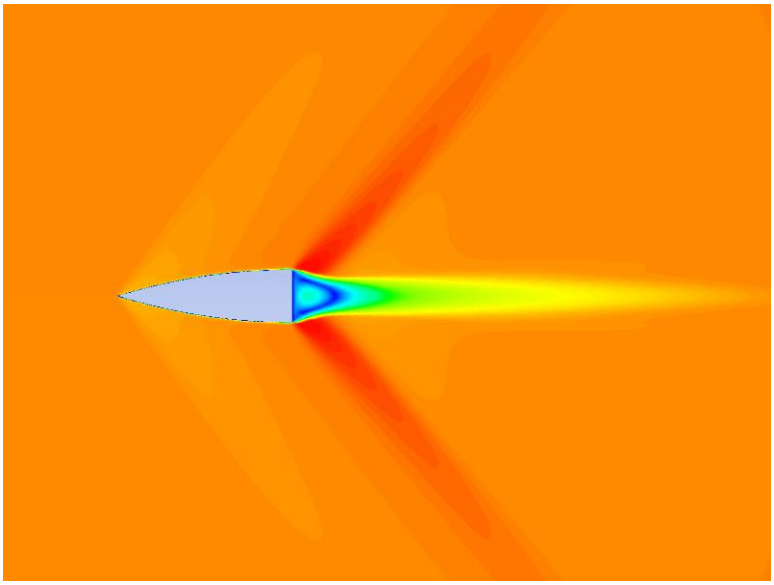

Figure 4.3 - Velocity contour of 5:1 ogive.

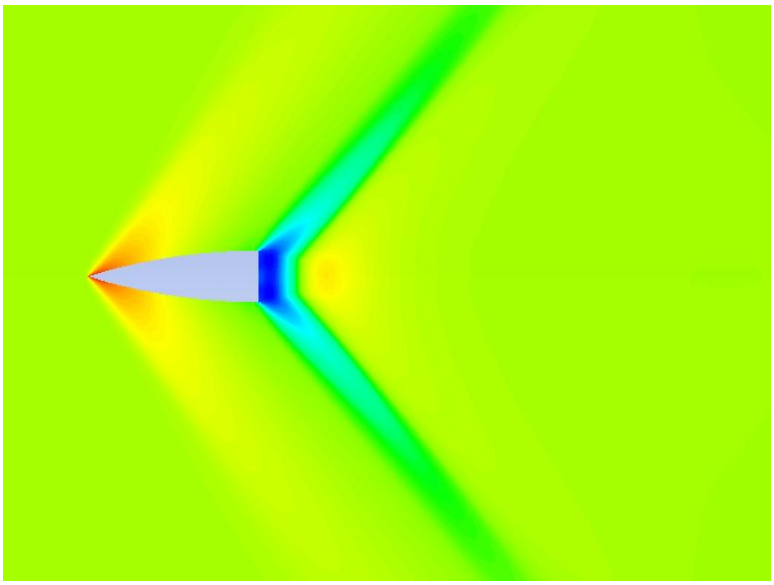

Figure 4.4 - Pressure contour of 5:1 ogive.

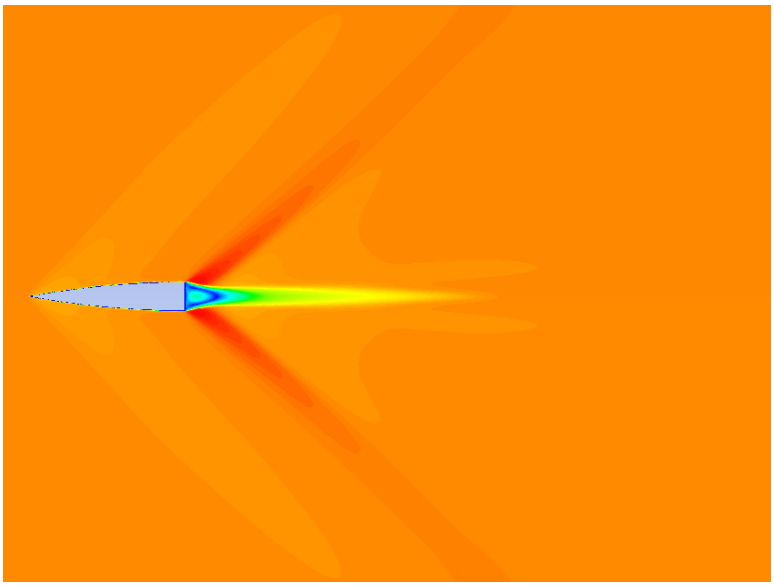

Figure 4.5 - Velocity contour of 6:1 ogive.

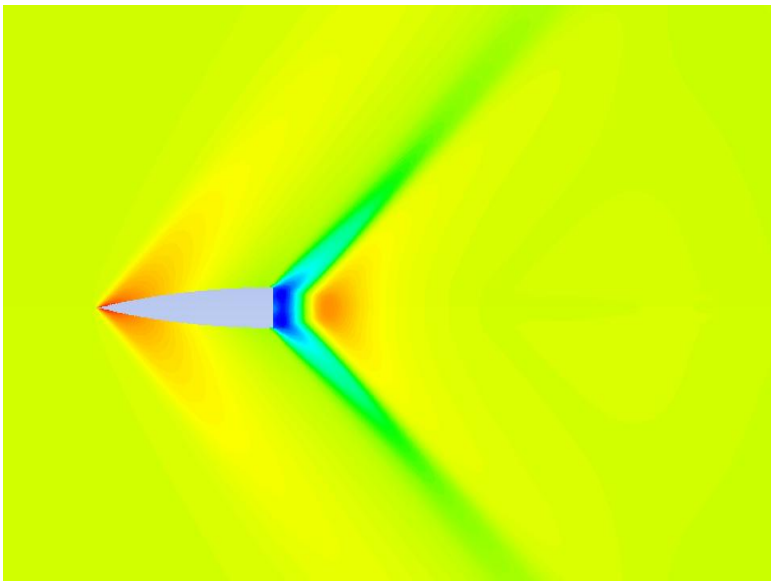

Figure 4.6 - Pressure contour of 6:1 ogive.

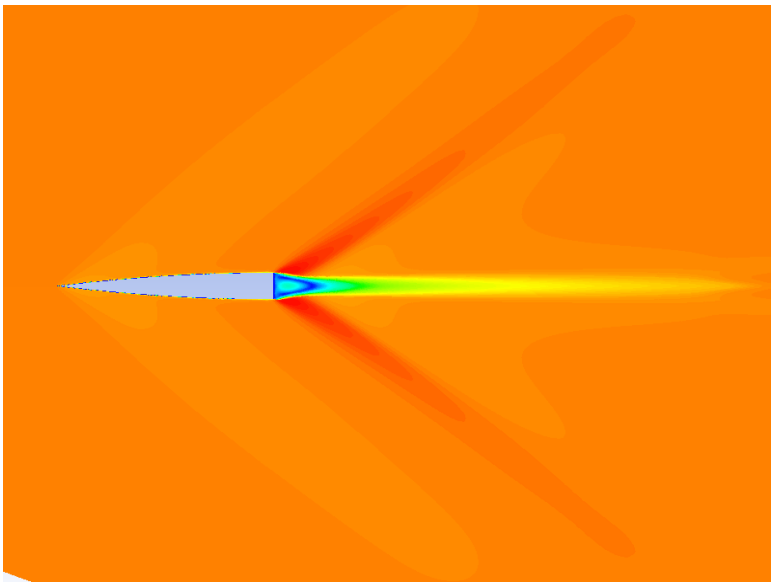

Figure 4.7 - Velocity contour of 7:1 ogive.

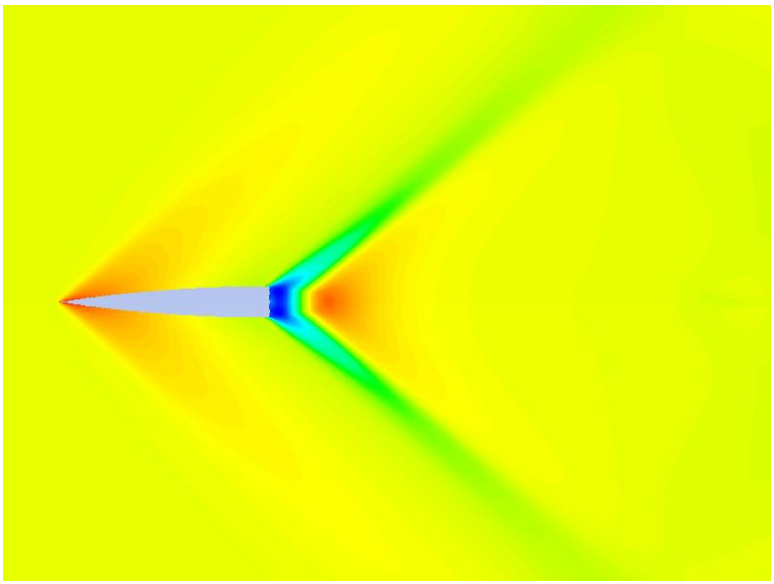

Figure 4.8 - Pressure contour of 7:1 ogive.

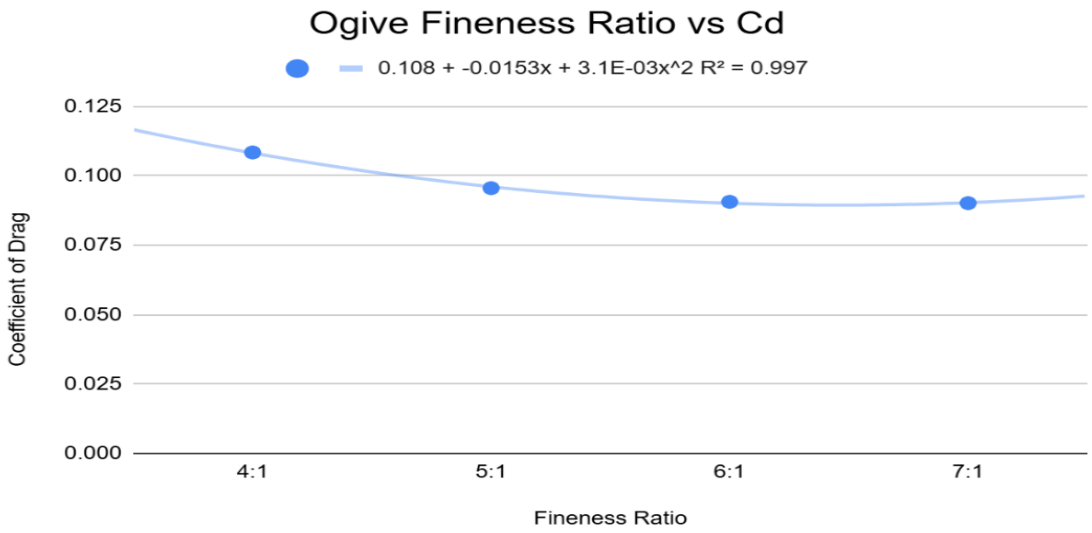

Figure 4.9 – Ogive fineness ratio vs cd.

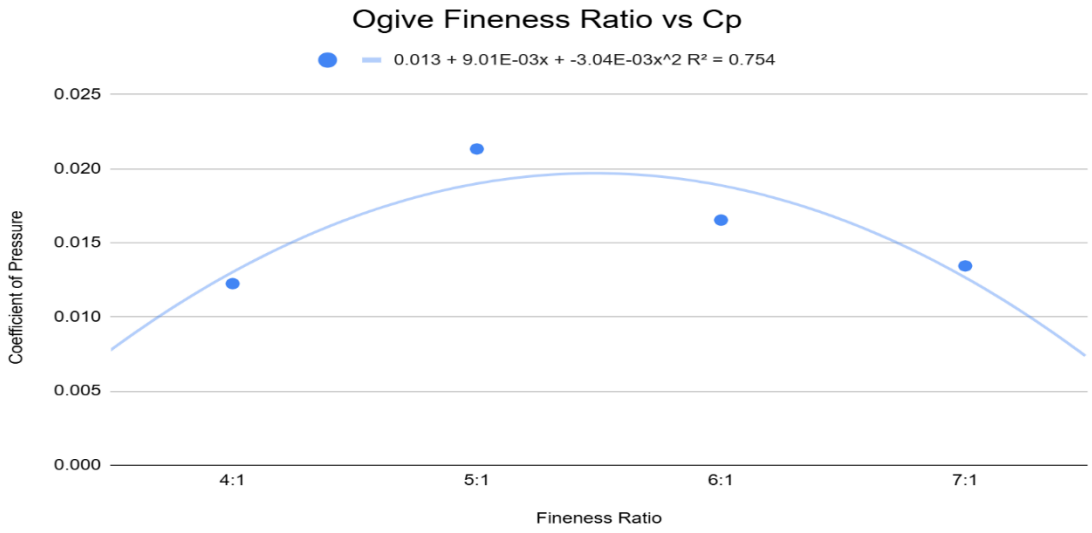

Figure 4.10 – Ogive fineness ratio vs Cp.

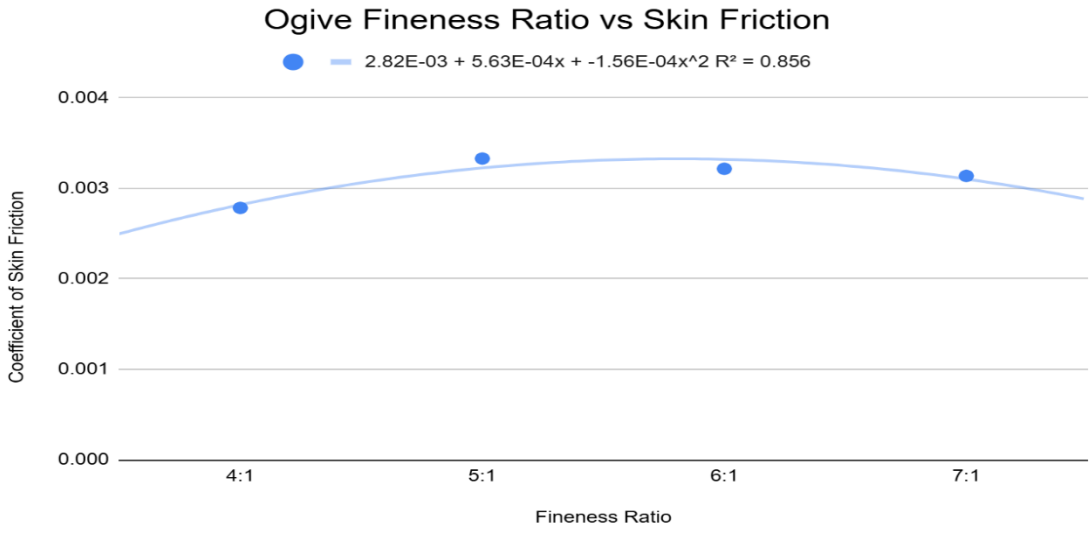

Figure 4.11 – Ogive fineness ratio vs skin friction.

4.1.2. Von Karman Nose Cone

The von Kármán nose cone's drag coefficient trends indicate significant improvement at higher fineness ratios, particularly from 6:1, where it drops to 0.0671, compared to 4:1 at 0.0964. This sharp reduction suggests that its contour effectively delays flow separation and reduces both pressure and wave drag, making it advantageous for supersonic applications. However, at 7:1, the coefficient increases slightly to 0.0846, indicating that excessive elongation does not always yield proportional aerodynamic benefits.

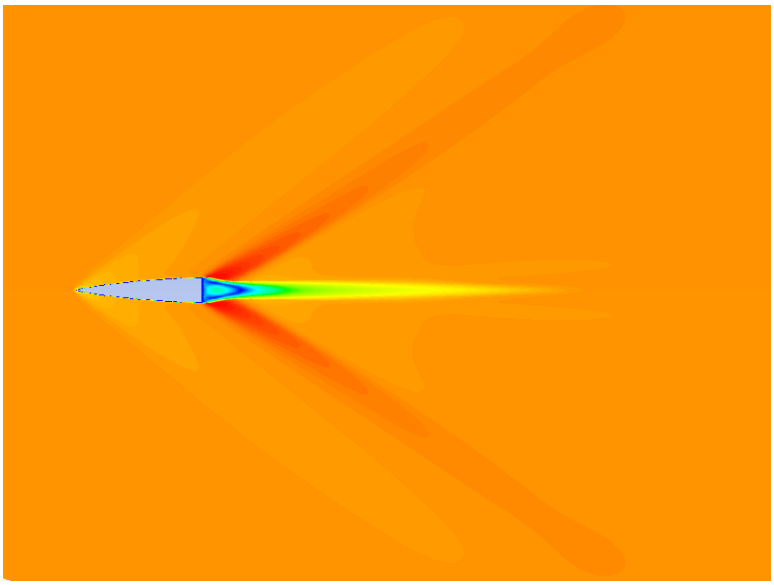

Figure 4.12 - Velocity contour of 4:1 von Karman.

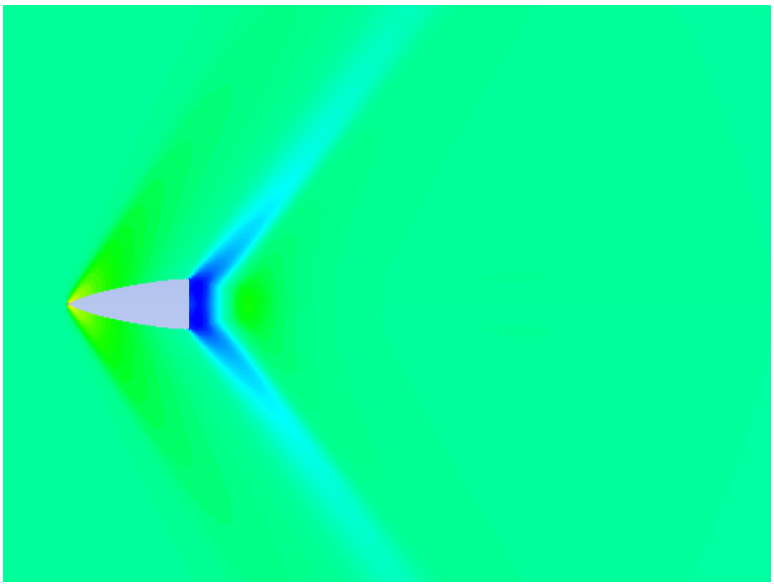

Figure 4.13 - Pressure contour of 4:1 von Karman.

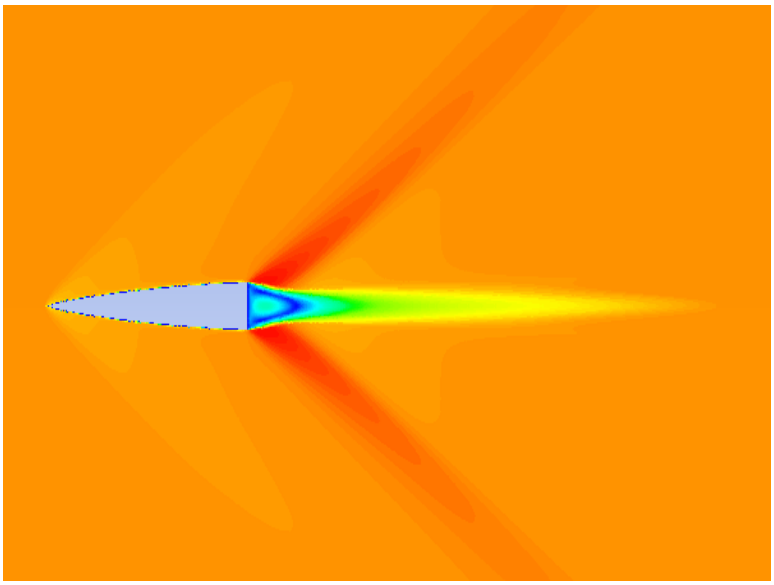

Figure 4.14 - Velocity contour of 5:1 von Karman.

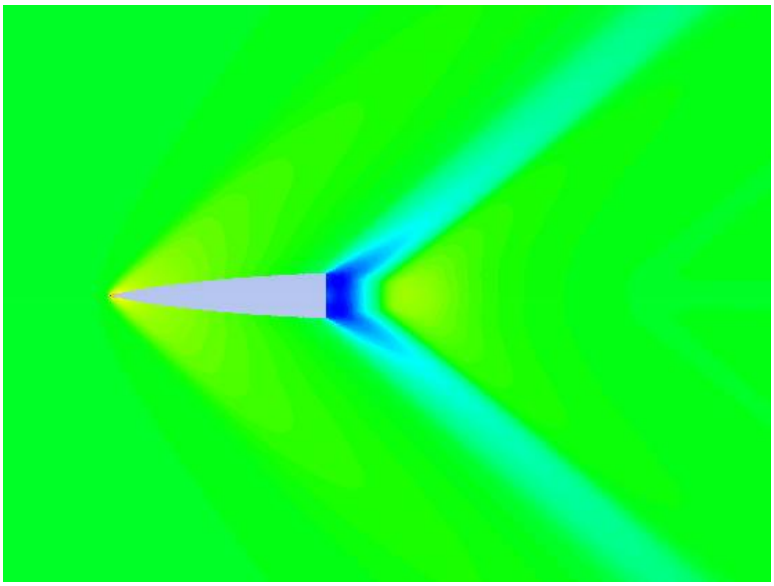

Figure 4.15 - Pressure contour of 5:1 von Karman.

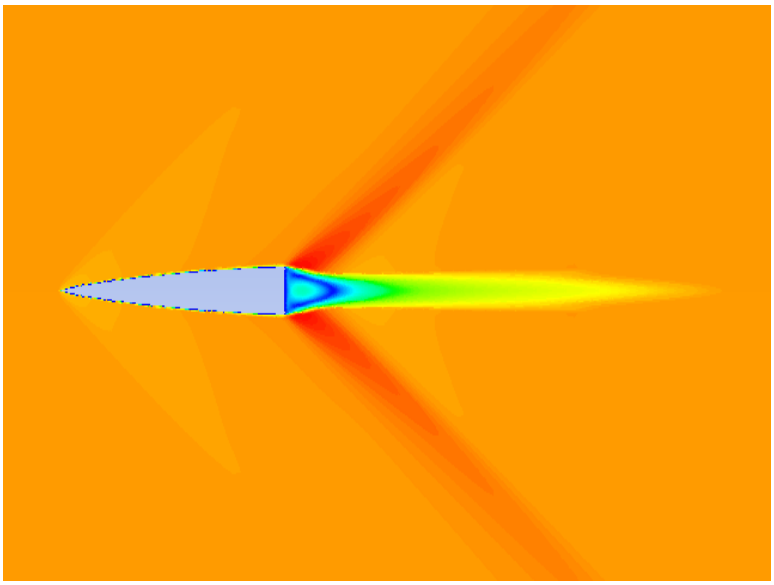

Figure 4.16 - Velocity contour of 6:1 von Karman.

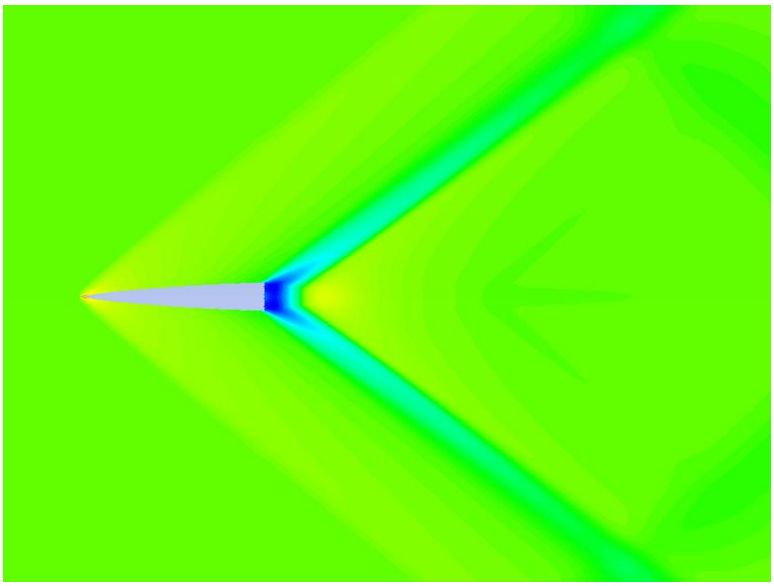

Figure 4.17 - Pressure contour of 6:1 von Karman.

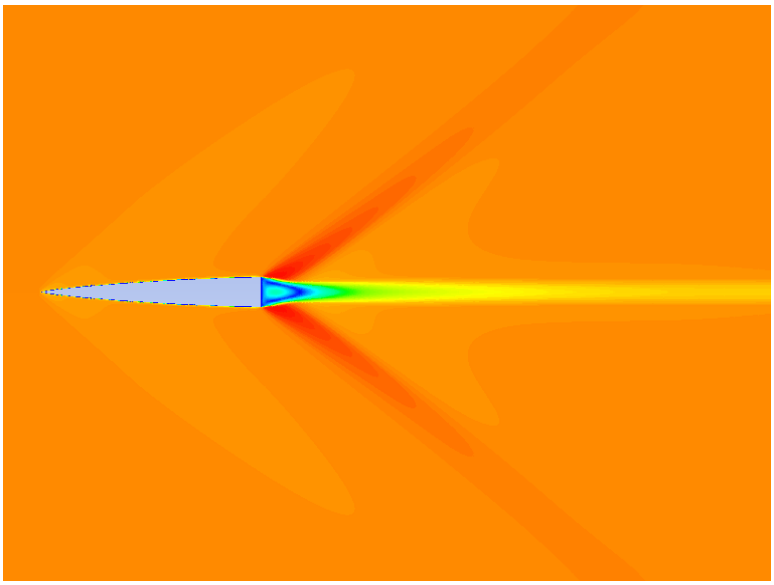

Figure 4.18 - Velocity contour of 7:1 von Karman.

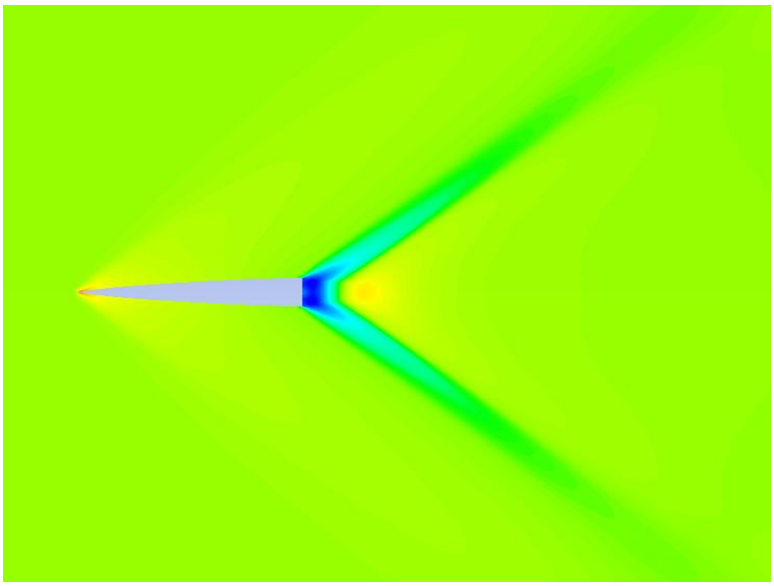

Figure 4.19 - Pressure contour of 7:1 von Karman.

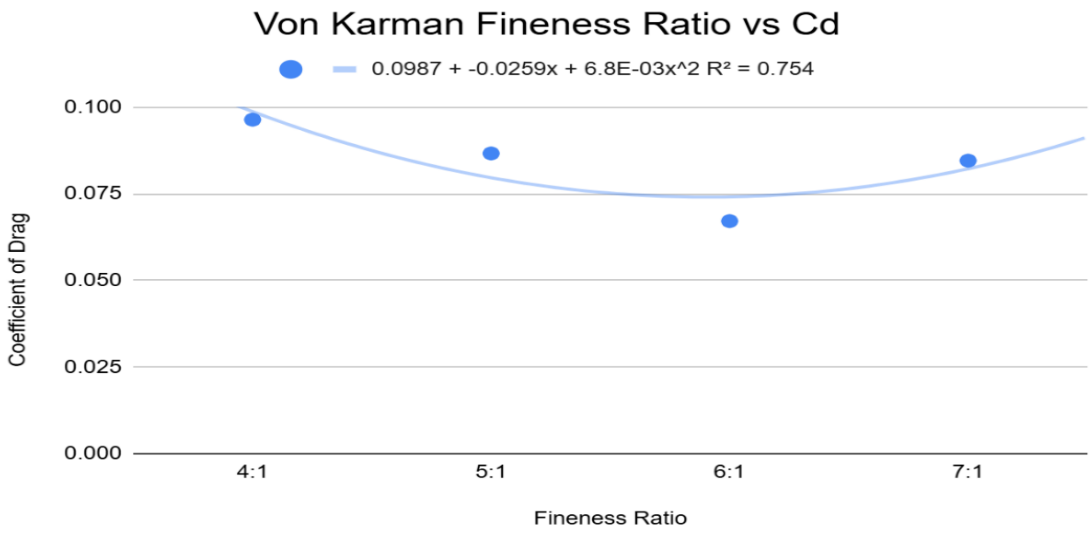

Figure 4.20 – Von Karman fineness ratio vs cd.

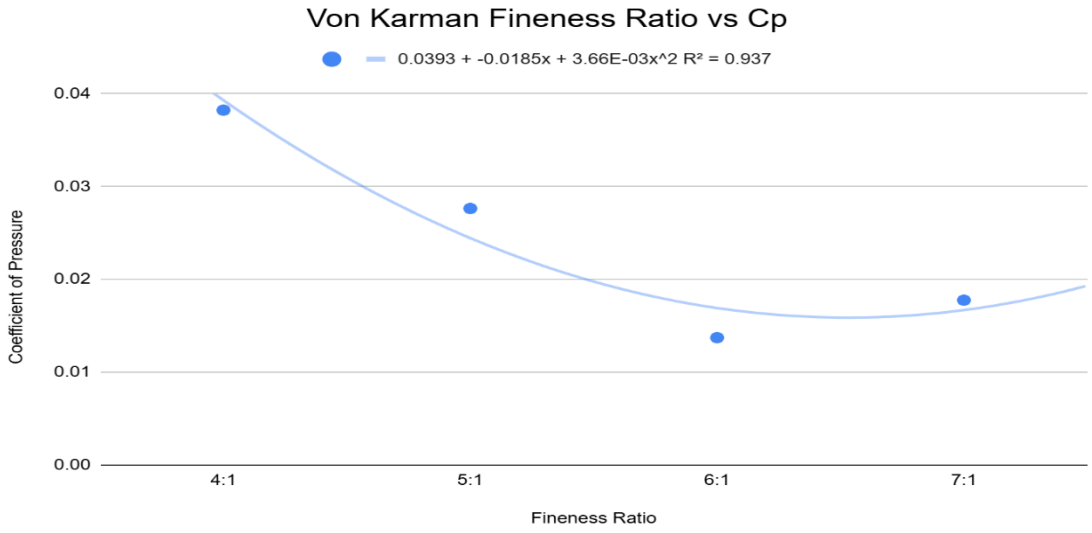

Figure 4.21 – Von Karman fineness ratio vs Cp.

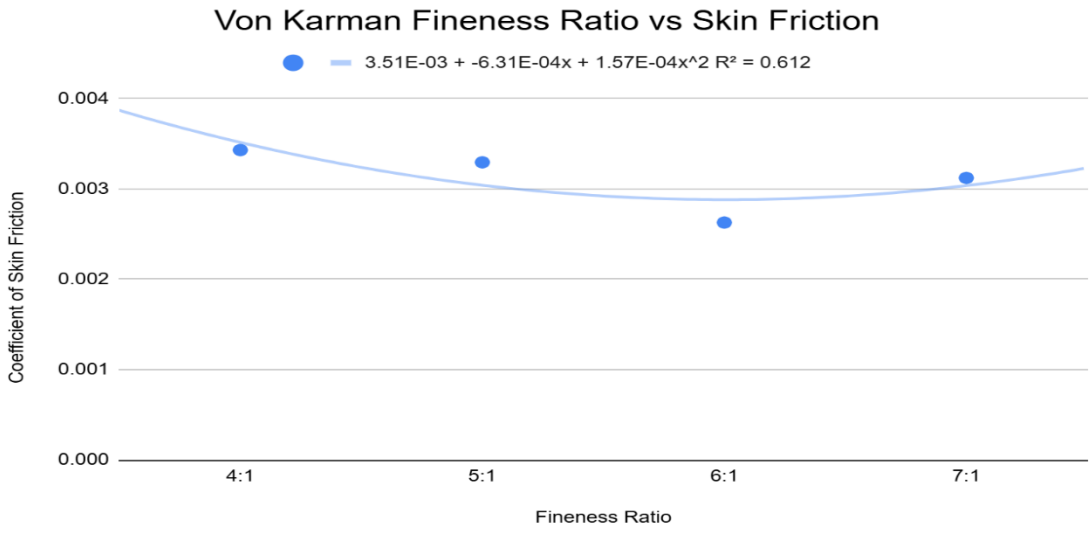

Figure 4.22 – Von Karman fineness ratio vs skin friction.

4.1.3. Long Ellipsoid Nose Cone

Elliptical nose cones exhibit distinct aerodynamic behavior compared to ogive and von Kármán profiles due to their continuously curved leading section. Unlike the other two, which gradually taper, an ellipsoid nose cone features a more gradual slope at the base, leading to higher drag coefficients. The data reflects this trend, with a 4:1 fineness ratio producing a significantly high drag coefficient of 0.1408. Even as the ratio increases to 7:1, the reduction in drag is not as pronounced, settling at 0.1139. This indicates that while increasing length helps lower drag, the gains are less efficient compared to sharper nose profiles.

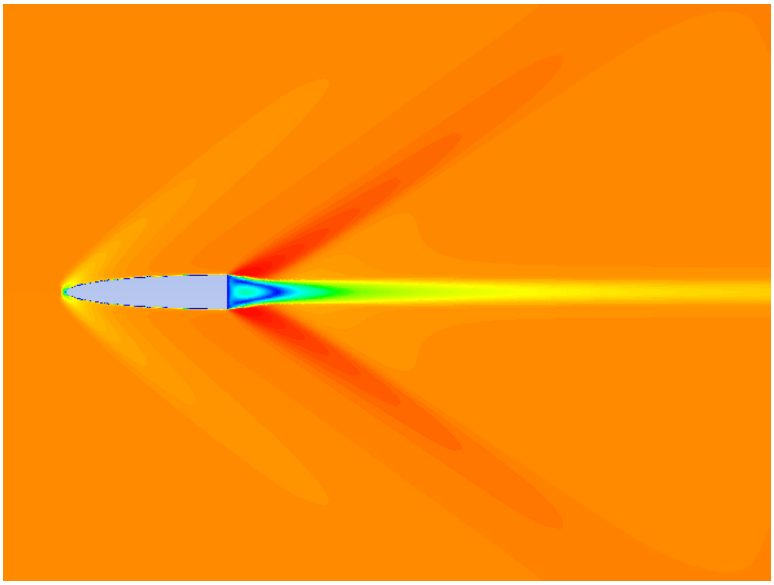

Figure 4.23 - Velocity contour of 4:1 long ellipsoid.

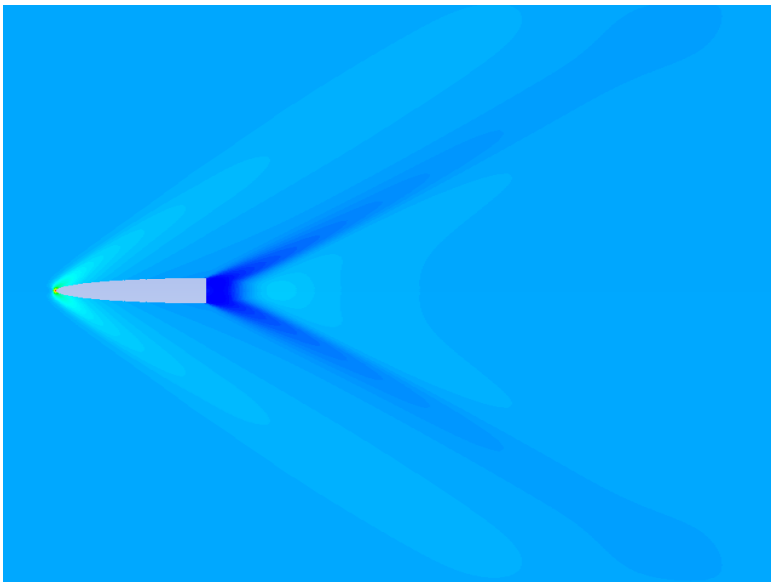

Figure 4.24 - Pressure contour of 4:1 long ellipsoid.

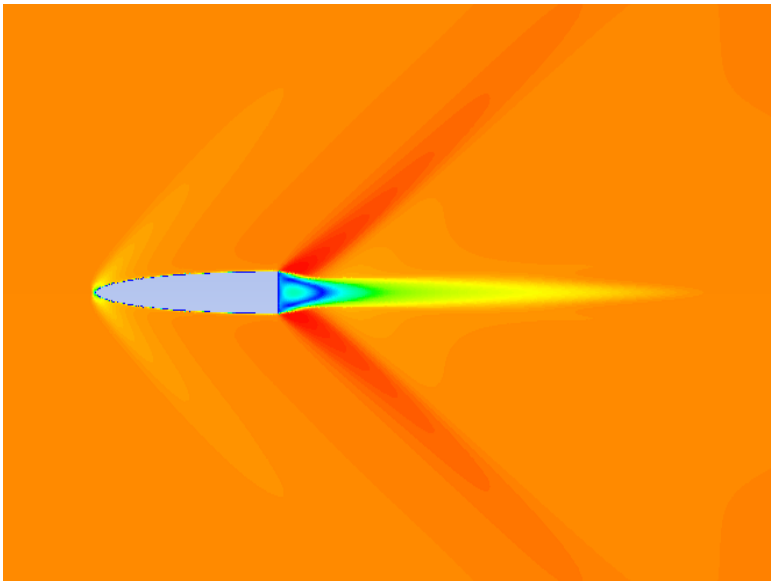

Figure 4.25 - Velocity contour of 5:1 long ellipsoid.

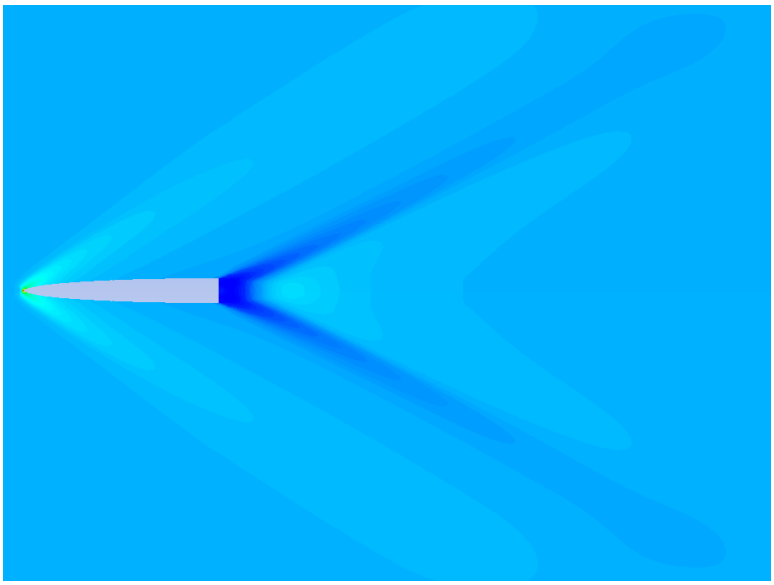

Figure 4.26 - Pressure contour of 5:1 long ellipsoid.

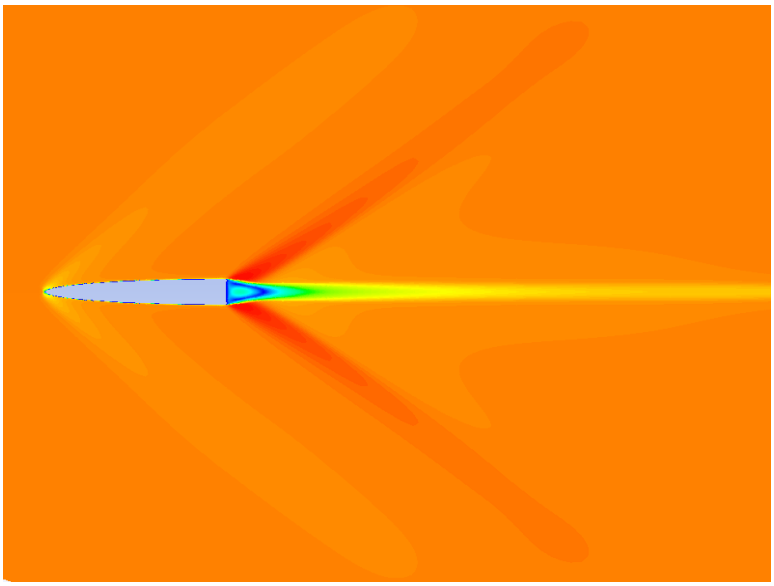

Figure 4.27 - Velocity contour of 6:1 long ellipsoid.

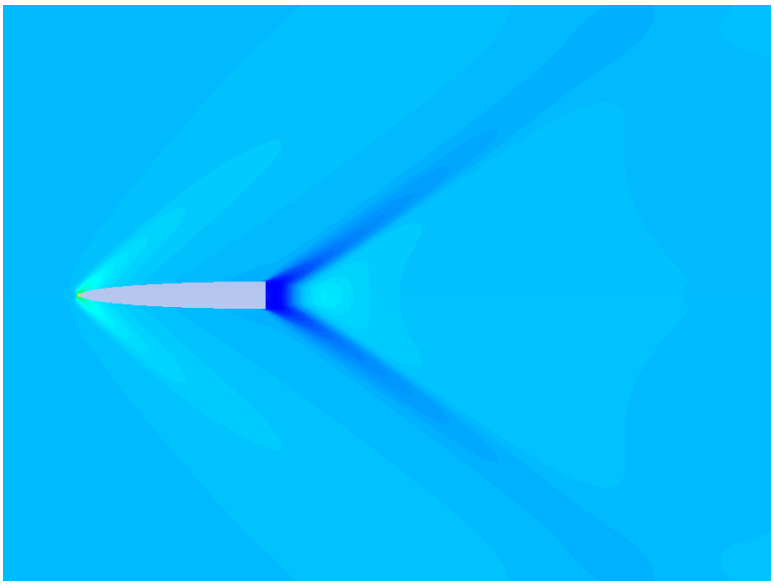

Figure 4.28 - Pressure contour of 6:1 long ellipsoid.

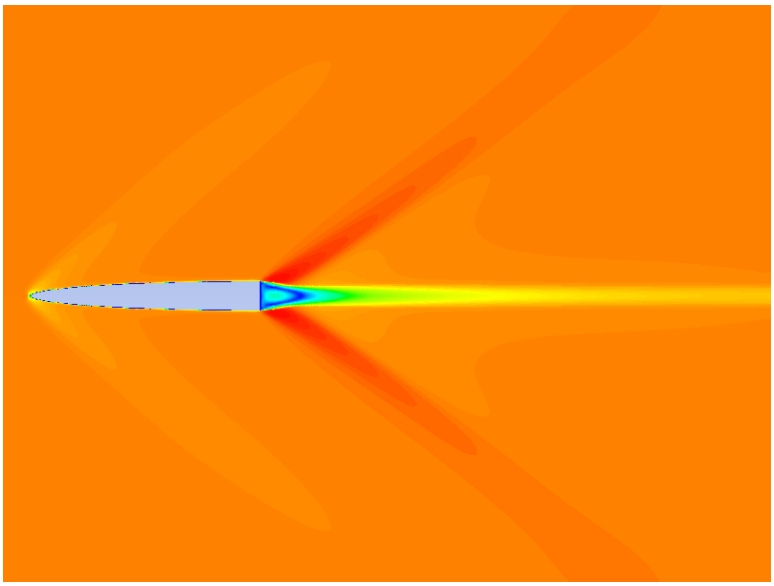

Figure 4.29 - Velocity contour of 7:1 long ellipsoid.

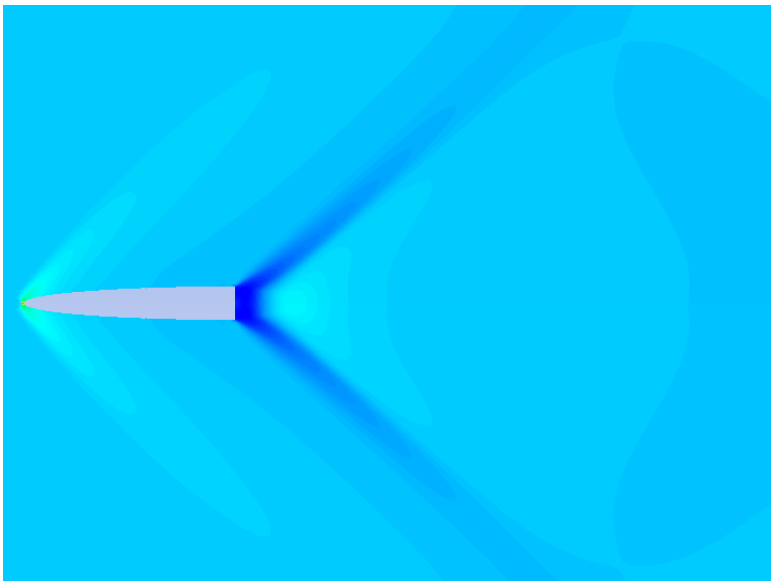

Figure 4.30 - Pressure contour of 7:1 long ellipsoid.

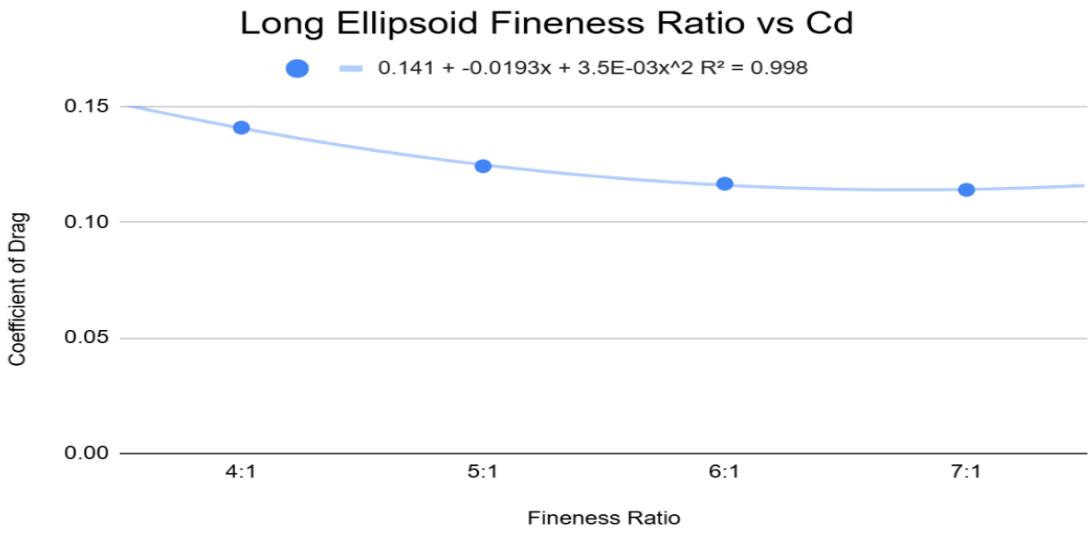

Figure 4.31 – Long ellipsoid fineness ratio vs cd.

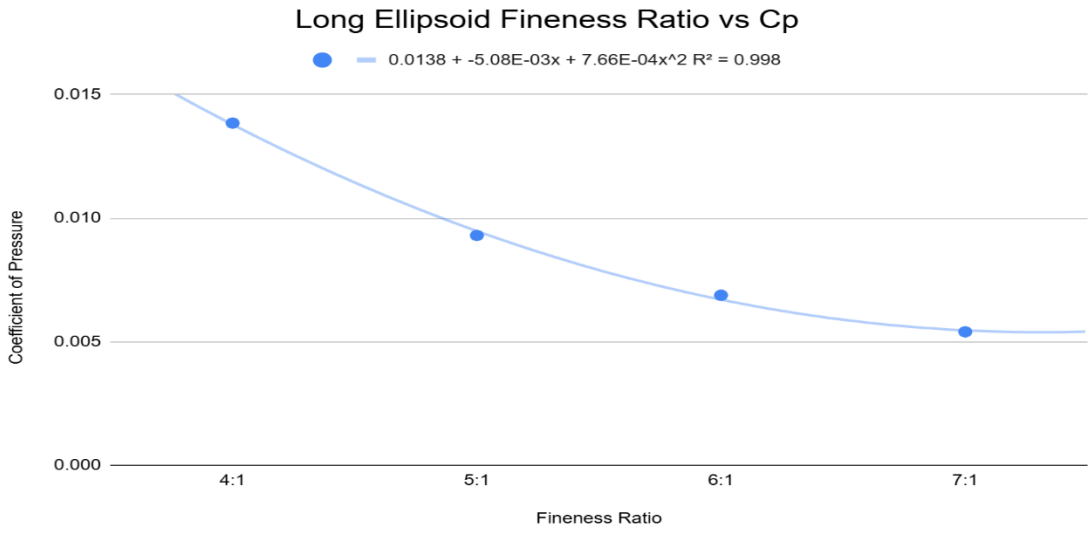

Figure 4.32 – Long ellipsoid fineness ratio vs Cp.

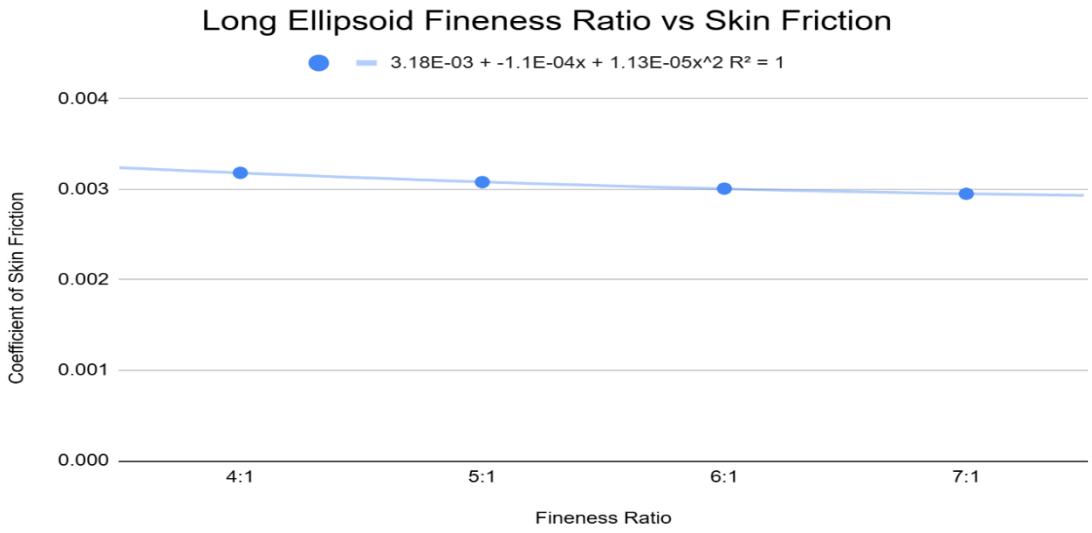

Figure 4.33 – Long ellipsoid fineness ratio vs skin friction.

4.2. 2D Fin Configuration

The following results were obtained from the two-dimensional CFD simulations of the tail fin and canard configurations. Each geometry was analyzed at deflection angles of 10° and 15°, under freestream conditions of Mach 1.5 at an altitude of 8,000 meters. The goal was to examine how shape and deflection angles affect surface pressure, friction, and overall aerodynamic performance. Tables 4.5 through 4.7 summarize the area-weighted averages of the pressure coefficient (Cp), skin friction coefficient (Cf), and drag coefficient (Cd) for each configuration.

These results help quantify how each design interacts with the supersonic flow and support the selection of efficient control surfaces for high-speed flight.

Table 4.5 – Drag coefficient for both deflection angles for tail fins.

Tail Fins	Deflection Angle	Coefficient of Drag
Trapezoidal Tail Fin	10 degrees	0.17833183
	15 degrees	0.22486861
Clipped Delta Tail Fin	10 degrees	0.22963326
	15 degrees	0.34006819

Table 4.6 – Pressure coefficient for both deflection angles for tail fins.

Tail Fins	Deflection Angle	Coefficient of Pressure
Trapezoidal Tail Fin	10 degrees	-0.0066550167
	15 degrees	-0.045271578
Clipped Delta Tail Fin	10 degrees	0.011992911
	15 degrees	0.0048927446

Table 4.7 – Skin Friction coefficient for both deflection angles for tail fins.

Tail Fins	Deflection Angle	Coefficient of Skin Friction
Trapezoidal Tail Fin	10 degrees	0.0029491078
	15 degrees	0.0026811403
Clipped Delta Tail Fin	10 degrees	0.0027960261
	15 degrees	0.003189538

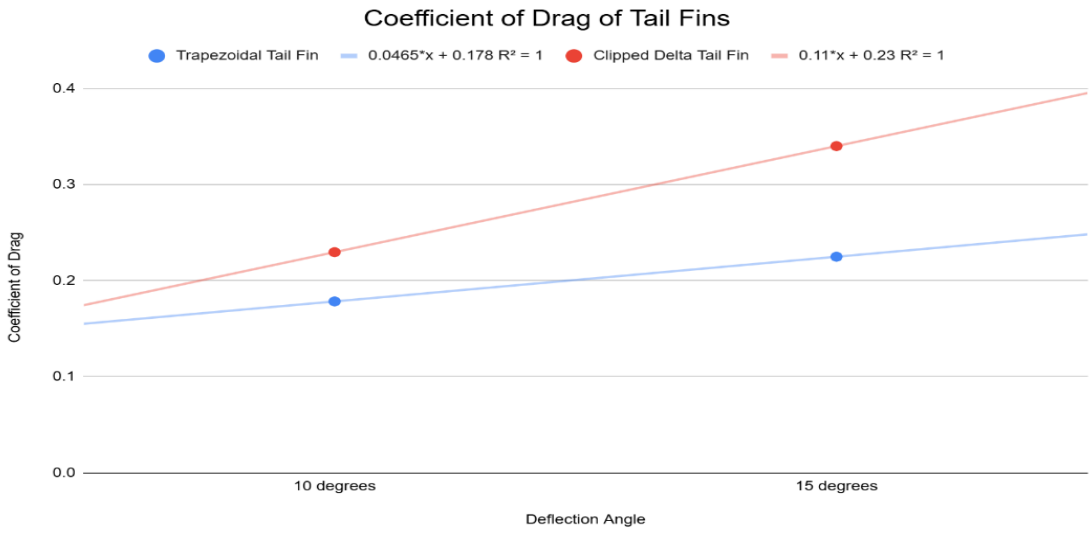

Figure 4.34 – Coefficient of drag of tail fins.

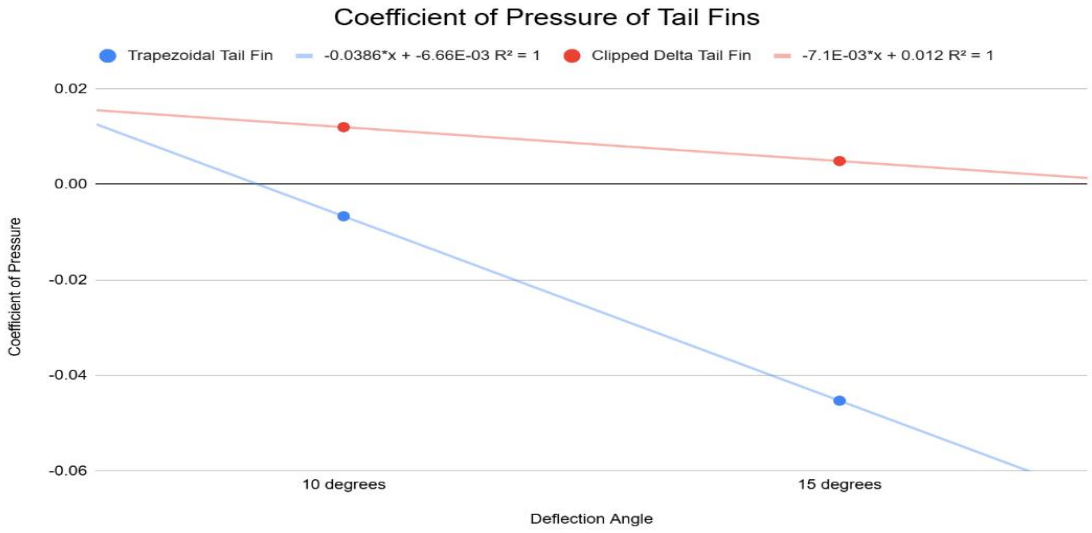

Figure 4.35 – Coefficient of pressure of tail fins.

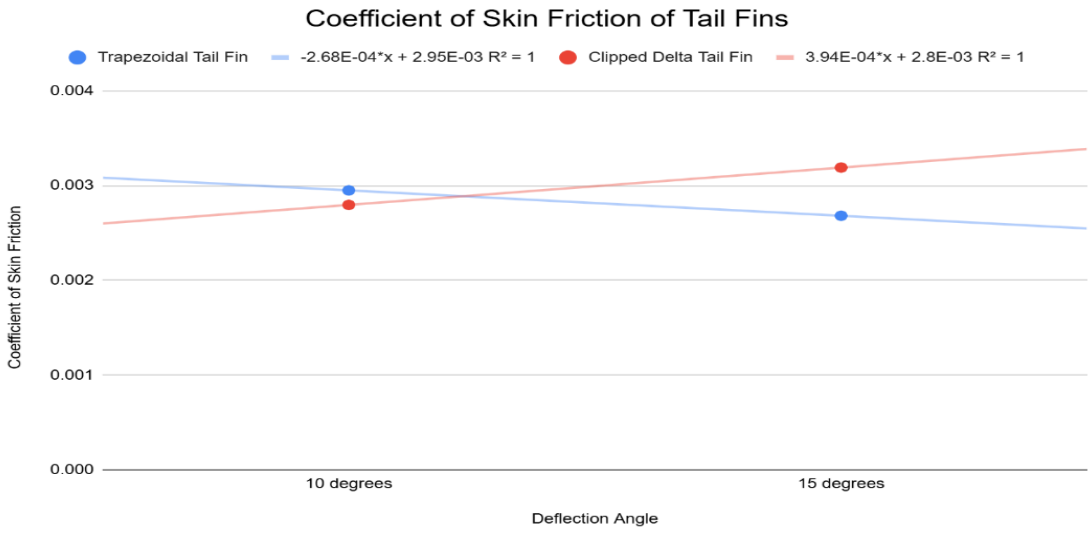

Figure 4.36 – Coefficient of skin friction of tail fins.

4.2.1. Trapezoidal Tail Fin

Table 4.8 – Trapezoidal tail fin area and length in meters.

Trapezoidal	Area [m^2]	Length [m]
10 degree	0.00914	0.3048
15 degree	0.00914	0.3048

The results for the trapezoidal tail fin focus on two control surface deflections: 10 degrees and 15 degrees. Velocity contours are provided for each case, showing how the supersonic freestream interacts with the fin geometry. At both angles, the velocity plots highlight flow acceleration along the leading edge and the formation of a wake region downstream of the trailing edge. As the deflection increases, the wake becomes more prominent, indicating stronger flow separation and increased aerodynamic resistance. Pressure contours are also included, which reveal surface loading patterns across the fin. These plots show areas of high and low pressure concentration, especially near the leading edge and root chord, where flow stagnation and pressure buildup occur. As the deflection angle increases, surface pressure becomes more uneven, which is associated with higher drag.

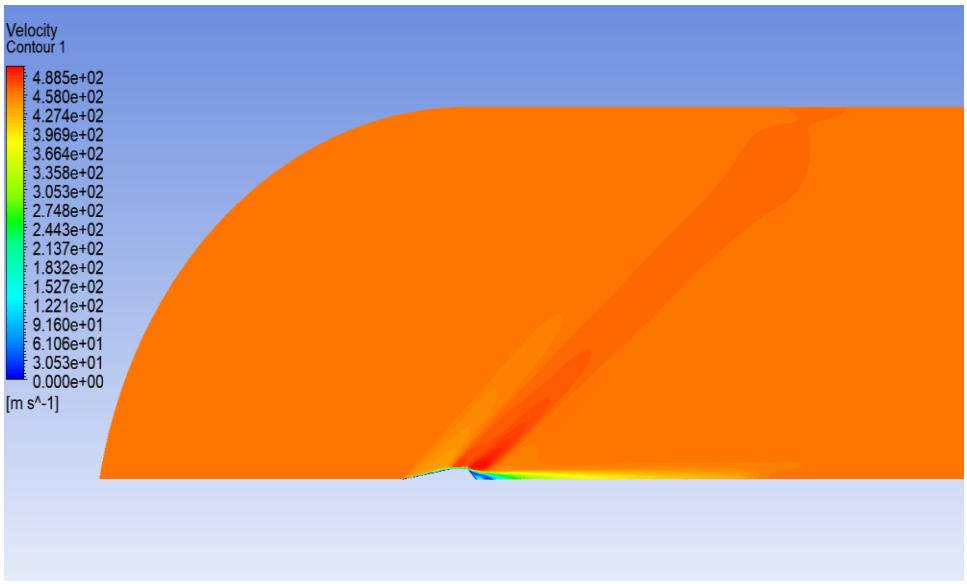

Figure 4.37 – Velocity contour of trapezoidal tail fin (10 deg).

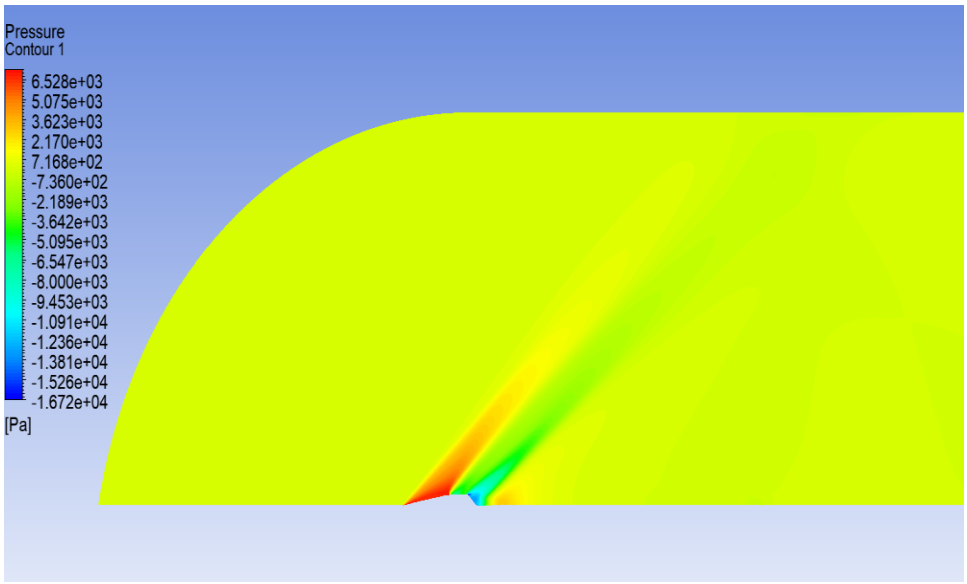

Figure 4.38 – Pressure contour of trapezoidal tail fin (10 deg).

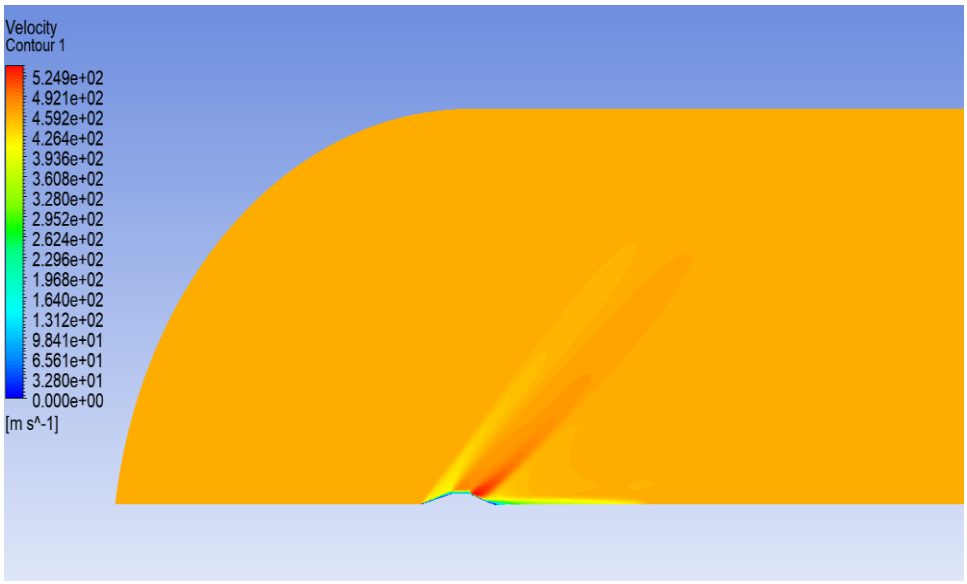

Figure 4.39 – Velocity contour of trapezoidal tail fin (15 deg).

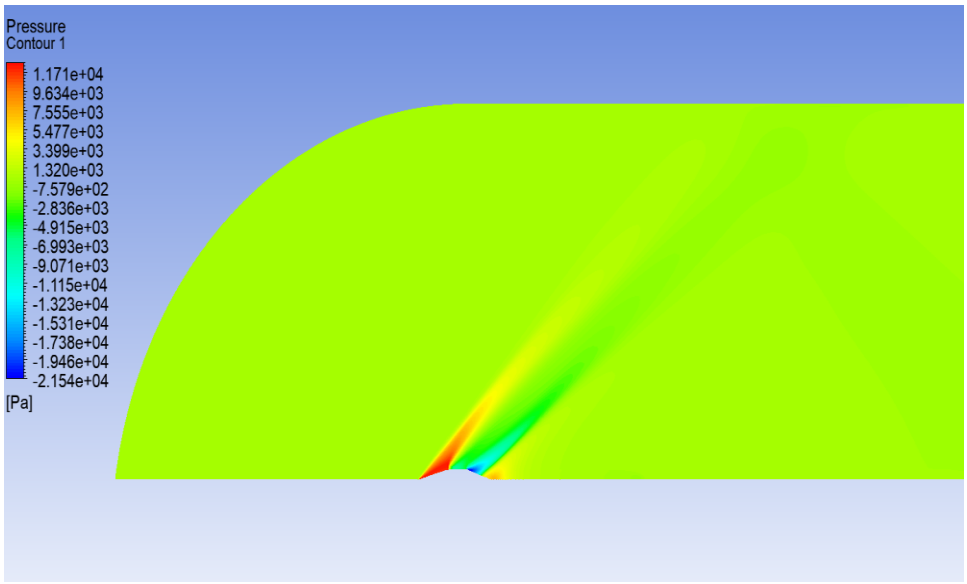

Figure 4.40 – Pressure contour of trapezoidal tail fin (15 deg).

4.2.2. Clipped Delta Tail Fin

Table 4.9 – Clipped delta tail fin area and length in meters.

Clipped Delta	Area [m^2]	Length [m]
10 degree	0.01238	0.3048
15 degree	0.01045	0.3048

Simulation results for the clipped delta tail fin include pressure and velocity contours at deflection angles of 10 degrees and 15 degrees. The clipped delta shape features a more aggressive sweep and shorter tip chord compared to the trapezoidal design. Velocity contours show how flow wraps around the leading edge and transitions into a separated wake behind the trailing edge. At 15 degrees, the velocity plot reveals a larger wake and stronger flow detachment, indicating increased aerodynamic drag. Pressure contours show how surface pressure builds across the fin as deflection increases. Areas near the root and leading edge show concentrated high pressure, while regions along the upper surface experience a drop in pressure, particularly at higher angles. These patterns reflect an increased lift and drag as the fin generates more control force. These values provide a clear comparison of aerodynamic loading and help explain how the clipped delta responds to changes in control input.

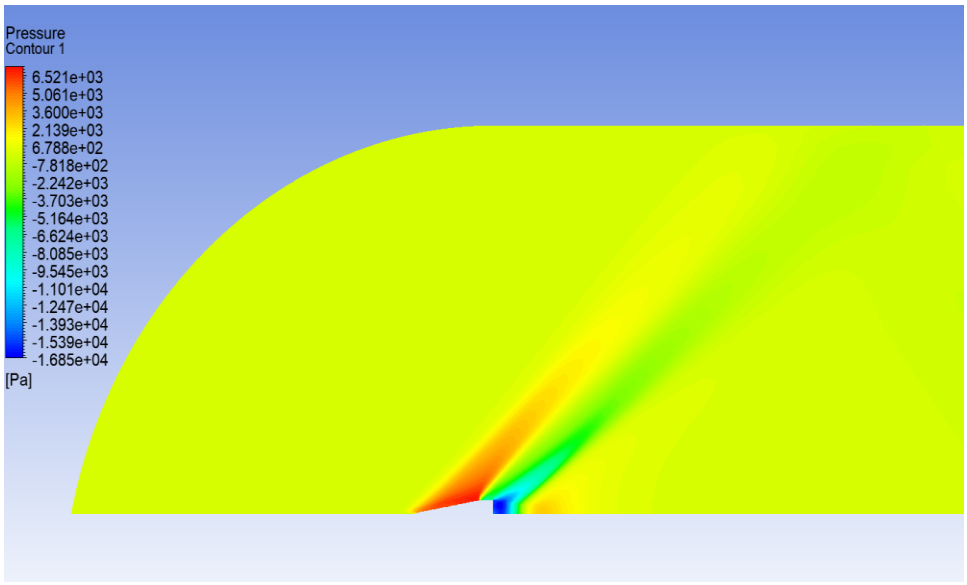

Figure 4.41 – Pressure contour of clipped delta tail fin (10 deg).

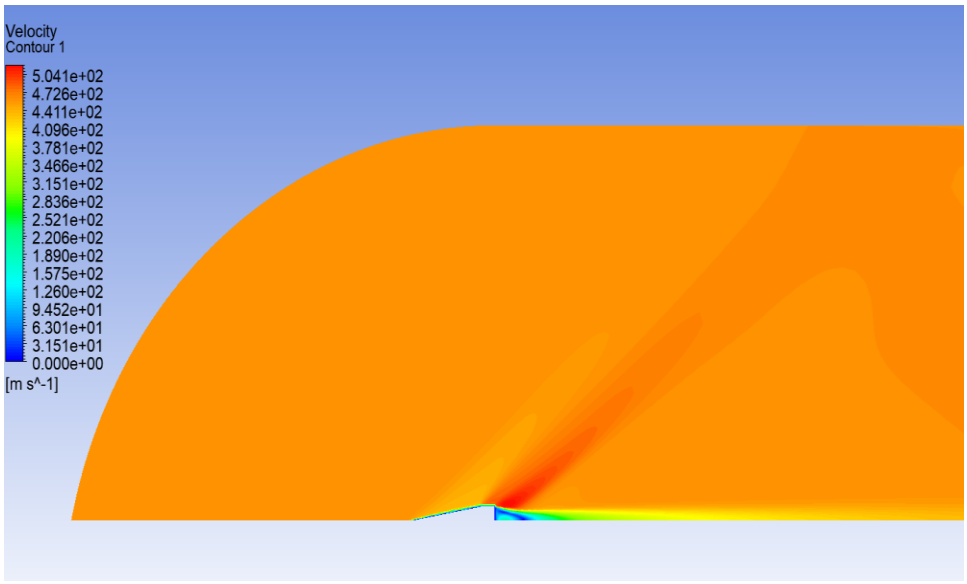

Figure 4.42 – Velocity contour of clipped delta tail fin (10 deg).

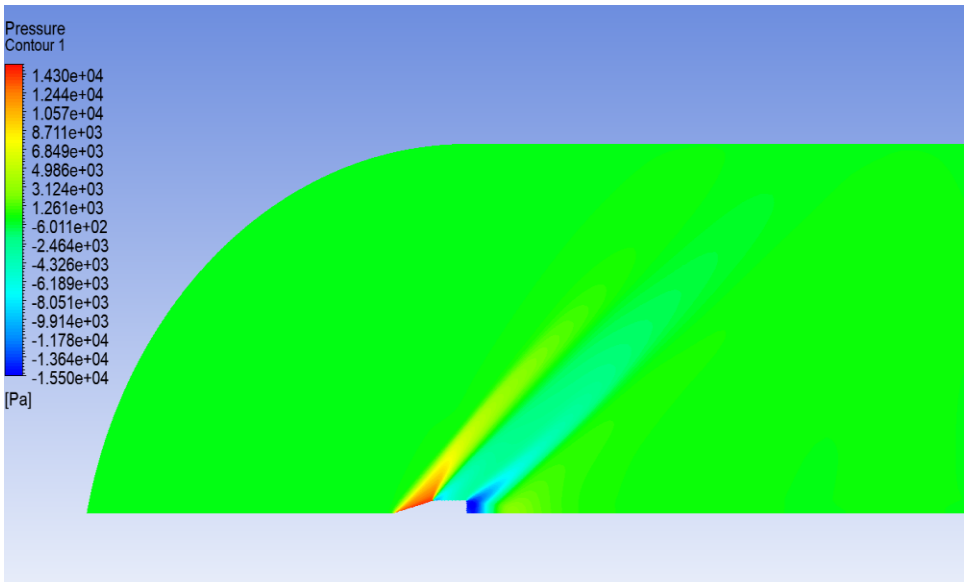

Figure 4.43 – Pressure contour of clipped delta tail fin (15 deg).

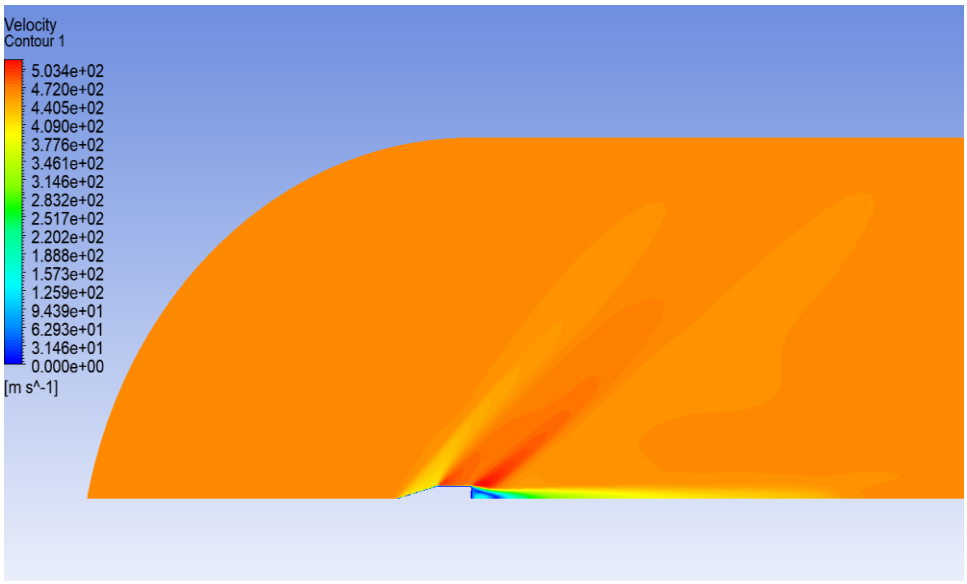

Figure 4.44 – Velocity contour of clipped delta tail fin (15 deg).

4.3. 2D Canards Configuration

Table 4.10 – Drag coefficient for both deflection angles for canards.

Canards	Deflection Angle	Coefficient of Drag
Delta Canards	10 degrees	0.57463797
	15 degrees	0.98360518
Swept Clipped Delta Canards	10 degrees	0.265046
	15 degrees	0.41584134

Table 4.11 – Pressure coefficient for both deflection angles for canards.

Canards	Deflection Angle	Coefficient of Pressure
Delta Canards	10 degrees	0.042433769
	15 degrees	0.1071579
Swept Clipped Delta Canards	10 degrees	0.0091923904
	15 degrees	-0.012088877

Table 4.12 – Skin friction coefficient for both deflection angles for canards.

Canards	Deflection Angle	Coefficient of Skin Friction
Delta Canards	10 degrees	0.0029677164
	15 degrees	0.0026226099
Swept Clipped Delta Canards	10 degrees	0.0027319378
	15 degrees	0.0028001006

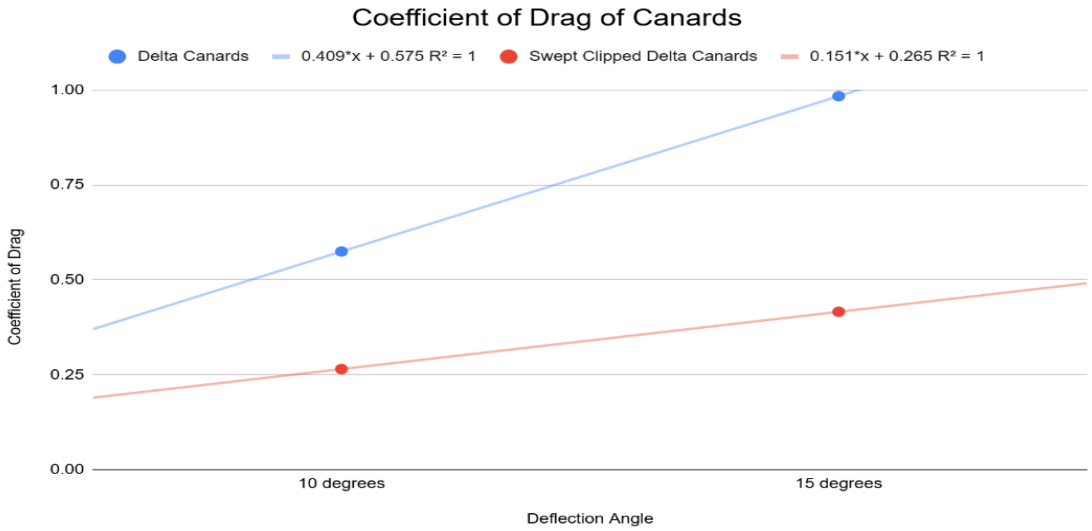

Figure 4.45 – Coefficient of drag of canards.

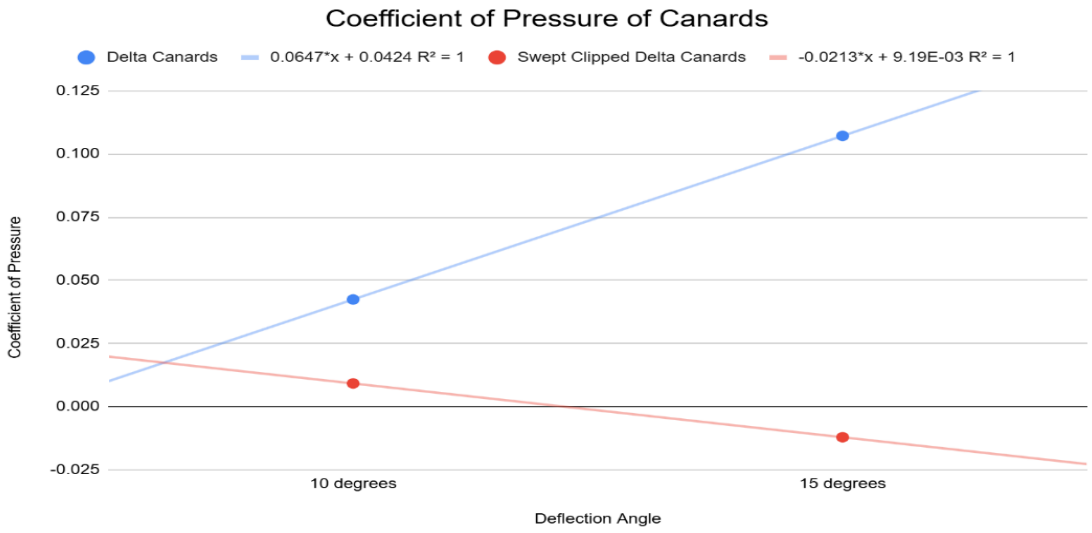

Figure 4.46 – Coefficient of pressure of canards.

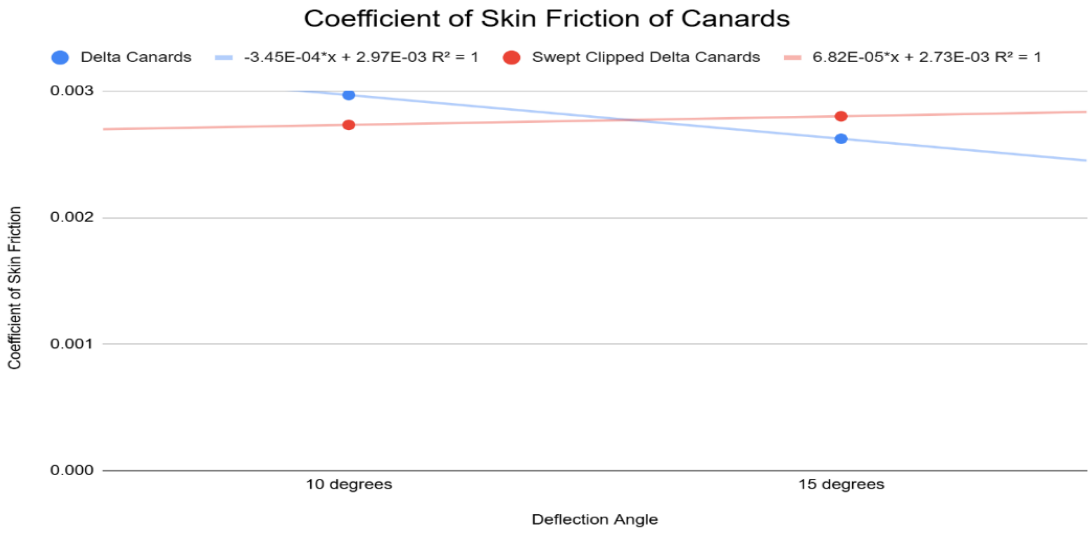

Figure 4.47 – Coefficient of skin friction of canards.

4.3.1. Swept Clipped Delta Canard

Table 4.13 – Swept clipped delta canard area and length in meters.

Swept Clipped Delta	Area [m^2]	Length [m]
10 degree	0.00358	0.1524
15 degree	0.00295	0.1524

The swept clipped delta canard was analyzed at deflection angles of 10 and 15 degrees. Results include velocity and pressure contours for each case, along with calculated aerodynamic coefficients. The velocity contours show how the deflected canard alters the incoming flow, particularly near the leading edge where acceleration occurs and at the trailing edge where flow separation begins to form. At 15 degrees, the wake region becomes more pronounced, and higher levels of flow disturbance appear downstream, indicating stronger aerodynamic influence. Pressure contours illustrate how loading changes across the surface of the canard as the deflection increases. At 10 degrees, pressure is distributed relatively evenly, while the 15-degree case shows larger pressure differences between the upper and lower surfaces. These differences translate to increased lift and drag.

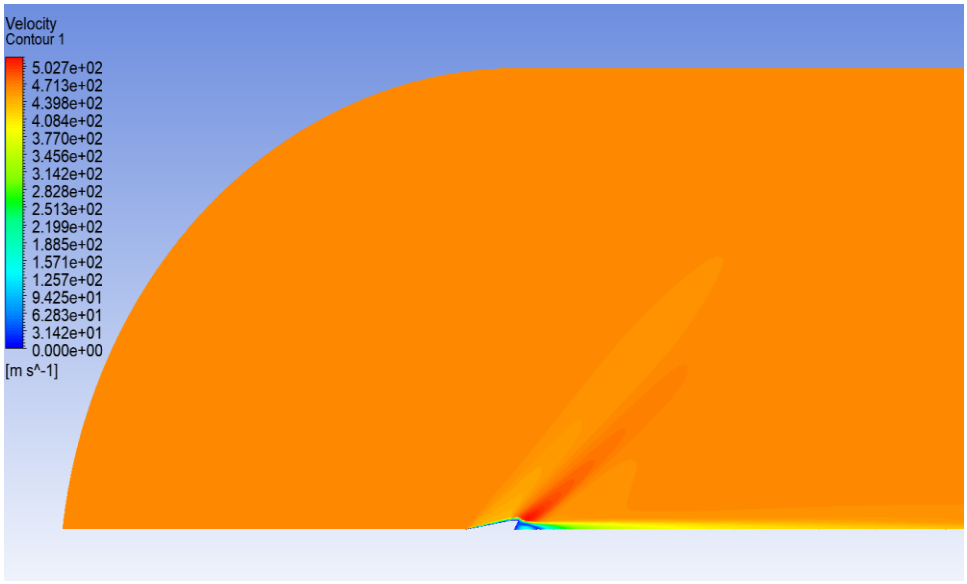

Figure 4.48 – Velocity contour of swept clipped delta canard (10 deg).

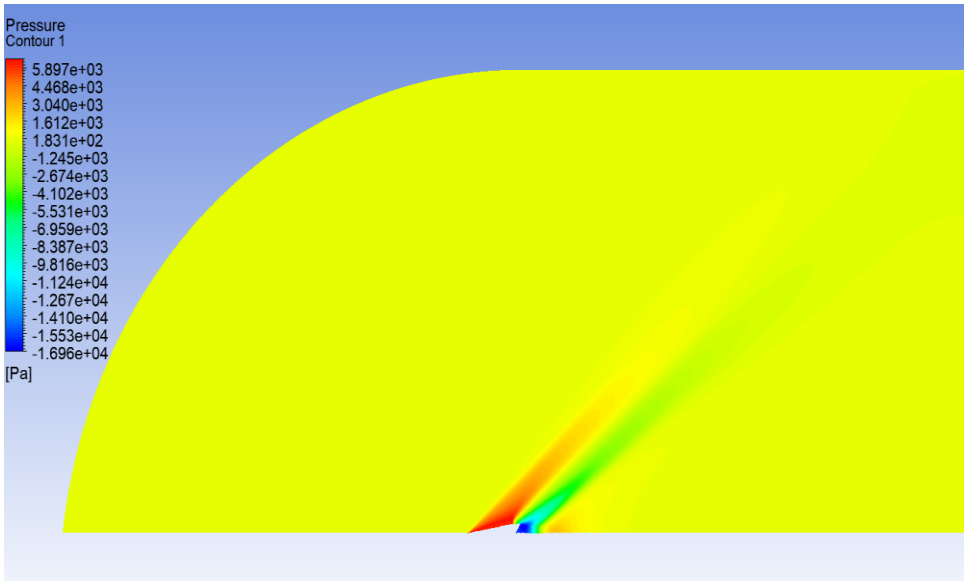

Figure 4.49 – Pressure contour of swept clipped delta canard (10 deg).

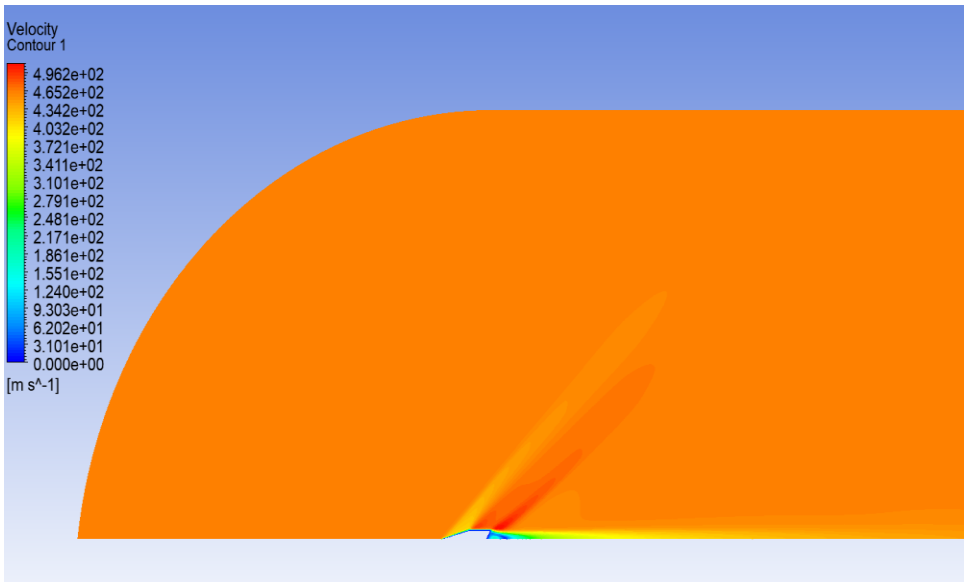

Figure 4.50 – Velocity contour of swept clipped delta canard (15 deg).

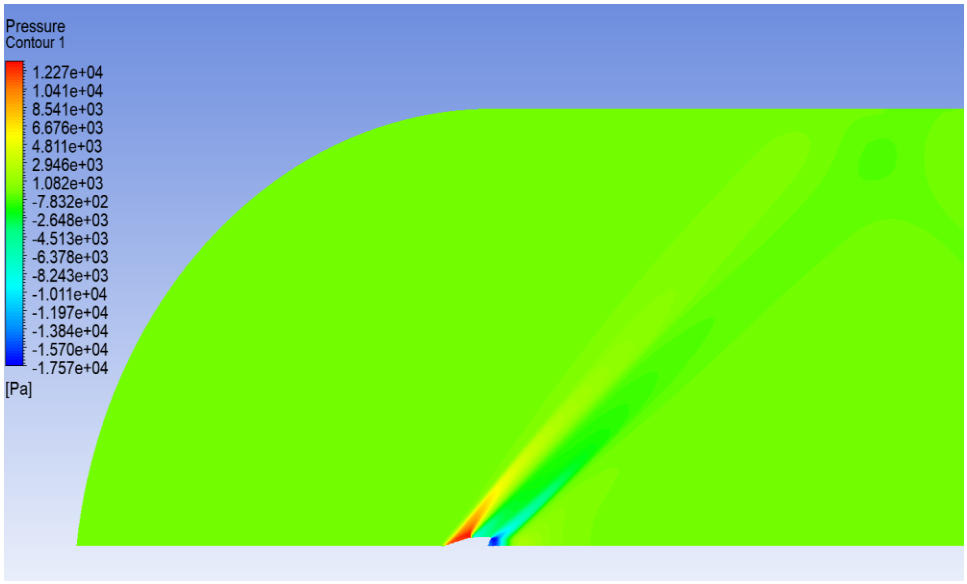

Figure 4.51 – Pressure contour of swept clipped delta canard (15 deg).

4.3.2. Delta Canard

Table 4.14 – Delta canard area and length in meters.

Delta	Area [m^2]	Length [m]
10 degree	0.00205	0.1524

15 degree	0.00312	0.1524

Results for the delta canard include pressure and velocity contours at 10 and 15 degrees of deflection, as well as aerodynamic coefficients for each case like the other canards and tail fins. The delta canard has a full triangular shape, which gives it a larger surface area than the swept clipped configuration. Velocity contours show how this larger surface interacts with the supersonic flow. At lower deflection, the airflow remains relatively attached, while at 15 degrees, the flow separates more aggressively behind the trailing edge, creating a larger wake region. These changes indicate an increase in drag and a stronger aerodynamic footprint. Pressure contours reveal how surface loading develops along the top and bottom surfaces. As the deflection increases, pressure rises on the lower surface and drops more significantly on the upper surface, increasing lift but also contributing to higher pressure drag.

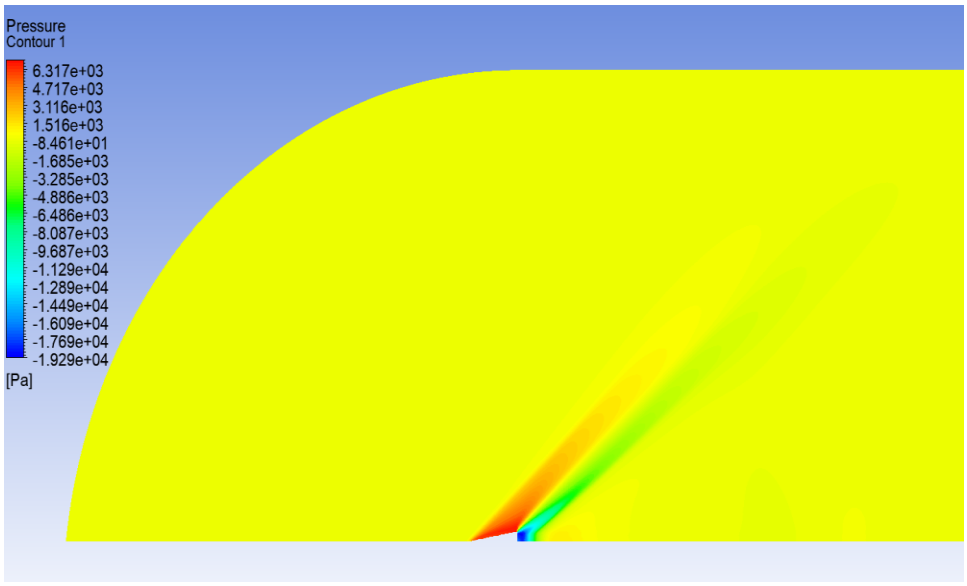

Figure 4.52 – Pressure contour of delta canard (10 deg).

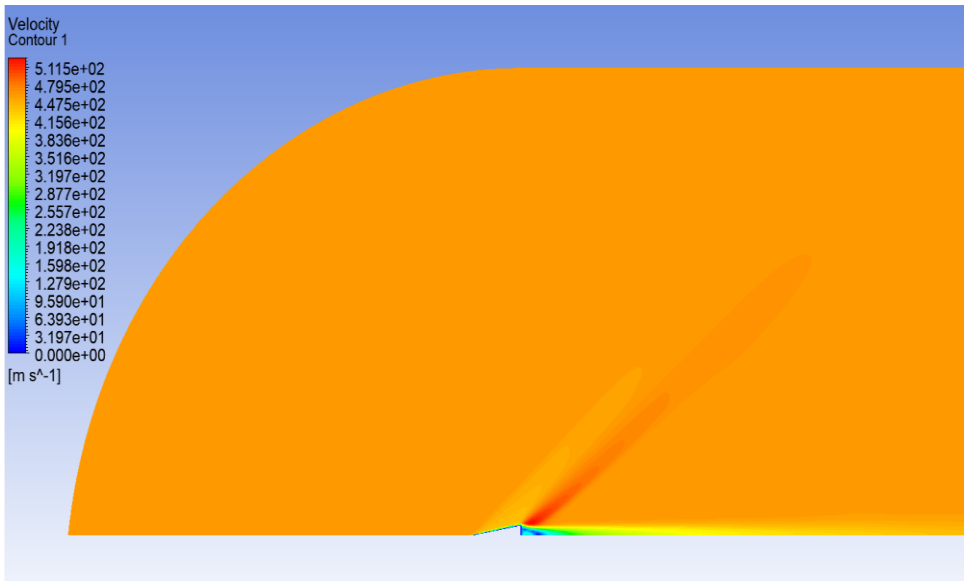

Figure 4.53 – Velocity contour of delta canard (10 deg).

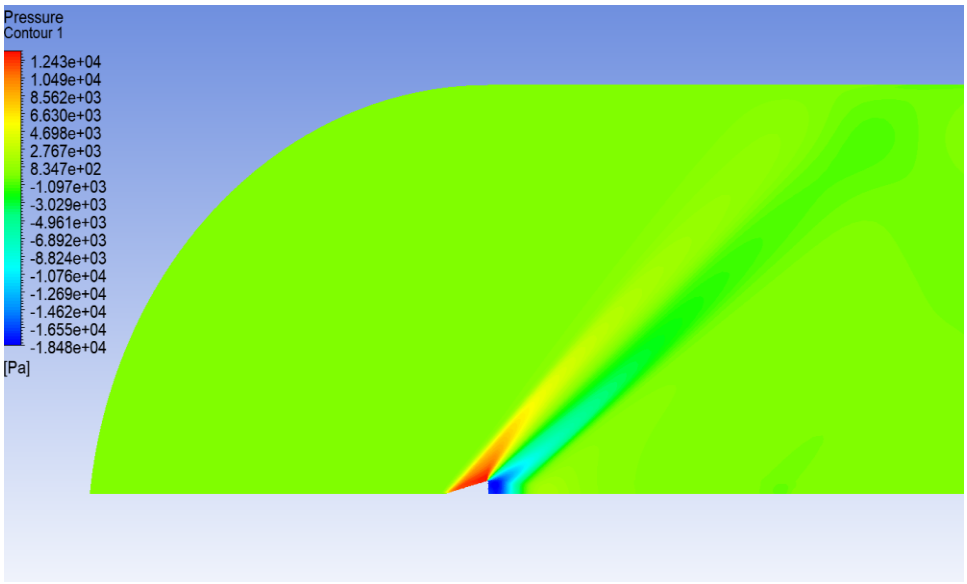

Figure 4.54 – Pressure contour of delta canard (15 deg).

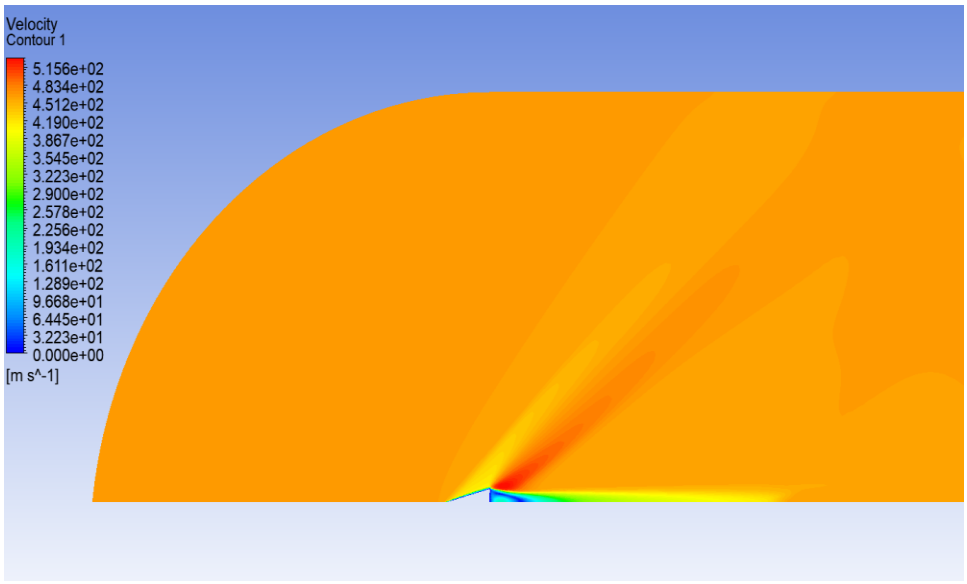

Figure 4.55 – Velocity contour of delta canard (15 deg).

5. Discussion of 2D and 3D Configurations

5.1. 2D Models

5.1.1. Nose Cone Configuration

This section analyzes the aerodynamic performance of the ogive, von Kármán, and long ellipsoid nose cones using the 2D CFD results obtained at Mach 1.5 and an altitude of 8,000 meters. Each geometry was tested at four fineness ratios 4:1, 5:1, 6:1, and 7:1 providing a consistent comparison of how nose cone length influences drag and overall flow behavior. The goal was to identify which profile delivered the lowest drag coefficient while maintaining favorable flow characteristics under supersonic conditions. The data in Table 4.1 shows that the von Kármán profile at a 6:1 ratio achieved the lowest drag coefficient (0.0671) out of all configurations. It consistently outperformed the ogive and ellipsoid designs at equivalent ratios. The ogive nose cone followed closely behind, especially at 6:1 and 7:1 where its drag values began to plateau around 0.0902. On the other hand, the long ellipsoid shape produced the highest drag coefficients, with its best result at 7:1 still higher than the worst-case values for the other two profiles. These trends are directly linked to how each shape manages pressure gradients, shock formation, and boundary layer behavior.

For the coefficient of pressure, the von Kármán profile generally exhibits the highest values, particularly at lower fineness ratios, indicating greater aerodynamic drag due to pressure differences. In contrast, the long ellipsoid consistently shows the lowest pressure coefficients, especially at higher fineness ratios, suggesting improved aerodynamic efficiency. Regrading the coefficient of skin friction, variations are more subtle, but the ogive and long ellipsoid shapes tend to maintain lower values at higher fineness ratios, implying reduced surface resistance. Overall, increasing the fineness ratio generally reduces both pressure and friction drag. Looking at the velocity contours, the ogive and von Kármán profiles both produced tightly compressed bow shocks near the nose tip, but the flow remained more attached along the surface of the von Kármán nose cone. This is especially visible in the 6:1 contour shown in Figure 4.16, where the flow maintains higher velocity magnitude closer to the body. The streamline behavior indicates a smoother transition of the boundary layer, reducing separation and allowing for better pressure recovery toward the aft end of the cone. In contrast, the ellipsoid designs show a thicker subsonic region along the body and more noticeable deceleration zones. These areas create increased pressure drag, especially near the midsection where the curvature transitions are more gradual, as seen in Figure 4.24 and Figure 4.26.

The pressure contours reinforce these observations. On the ogive and von Kármán profiles, there is a strong high-pressure region at the stagnation point followed by a rapid pressure drop along the cone. The von Kármán, however, maintains a lower pressure gradient farther

downstream, meaning less resistance and reduced pressure drag. This behavior is clearly illustrated in Figure 4.17 and Figure 4.19. In contrast, the ellipsoid nose cones display broader high-pressure zones extending farther along the body, as shown in Figure 4.28. These extended zones are a sign that the flow is not being smoothly redirected, especially at lower fineness ratios where the curvature is more abrupt. As a result, more energy is lost due to increased drag. An important aerodynamic takeaway is that elongating the nose cone improves drag performance, but only up to a point. For all three shapes, the largest drop in drag occurs between 4:1 and 6:1. Beyond that, gains become marginal especially for the ogive and ellipsoid configurations. The von Kármán at 6:1 provides the best compromise between minimized drag and geometric practicality, making it a strong candidate for integration into the 3D baseline model.

From a design perspective, these findings show that nose cone geometry directly influences how shock waves form and how the boundary layer behaves, which in turn controls drag. The von Kármán nose cone demonstrated the most favorable aerodynamic profile due to its inherent ability to delay flow separation and reduce both wave and pressure drag at supersonic speeds. The ogive profile showed decent performance with a simpler shape, making it potentially easier to manufacture. The ellipsoid nose cone, while structurally smooth, lacked the sharp flow control needed for efficient supersonic travel.

5.1.2. Tail Fin Configuration

The tail fin analysis includes two 2D configurations: a trapezoidal fin and a clipped delta fin. Each was evaluated at deflection angles of 10° and 15° to investigate how geometry and control surface angle affect aerodynamic performance in supersonic flow at Mach 1.5. The primary goal of this comparison was to observe differences in drag buildup, surface pressure distribution, and wake behavior caused by variations in planform shape and deflection. Among the two geometries, the trapezoidal fin produced the lower drag values. At 10°, the drag coefficient was 0.1783, increasing to 0.2249 at 15°. The clipped delta fin generated 0.2296 at 10° and reached 0.3401 at 15°, making it the highest-drag configuration in this section. This increase is attributed to the clipped delta's sharper sweep and wider chord base, which amplifies pressure drag and create a broader wake as the deflection increases. Velocity contours for the trapezoidal fin are shown in Figures 4.37 and 4.39. At 10°, flow remains attached across much of the surface, with a narrow wake forming behind the trailing edge. In Figure 4.39, separation becomes more pronounced at 15°, leading to a thicker wake and increased downstream flow deceleration. The clipped delta fin contours, shown in Figures 4.42 and 4.44, reveal greater flow curvature and velocity gradients even at 10°, with more aggressive separation and a wider low-velocity region appearing at 15°.

Pressure contours offer further insight into surface loading patterns. For the trapezoidal fin (Figures 4.38 and 4.40), moderate pressure builds along the lower surface with relatively even distribution. At 15°, Figure 4.40 shows localized intensification near the root, but the pressure remains better balanced across the span compared to the clipped delta. In Figures 4.41 and 4.43,

the clipped delta displays stronger pressure gradients and less uniform surface loading. High-pressure concentrations near the root and tip at 15° contribute to greater drag and reduced flow stability. Both fins can generate control forces, but their aerodynamic efficiencies differ significantly. The trapezoidal fin provides smoother pressure transitions and better flow attachment at moderate deflections, making it more efficient for minimizing drag while maintaining control authority. The clipped delta offers higher potential control force due to its geometry but at the cost of significantly more drag and a more unstable wake.

5.1.3. Canard Configuration

The aerodynamic performance of two canard geometries was evaluated using the same methods at Mach 1.5. These configurations include a swept clipped delta canard and a full delta canard, both tested at deflection angles of 10° and 15°. While both canards are designed to provide additional control authority, their geometric differences lead to noticeably different aerodynamic characteristics. The swept clipped delta canard produced lower drag across both deflection angles. At 10°, it recorded a drag coefficient of 0.1573, which increased to 0.2266 at 15°. The delta canard, with its larger surface area and sharper planform, showed higher drag values, reaching 0.1857 at 10° and 0.2882 at 15°. These results suggest that while both shapes produce control forces, the full delta canard imposes a greater aerodynamic cost, especially at higher deflection angles.

Velocity contours for the swept clipped delta canard are shown in Figures 4.48 and 4.50. At 10°, the flow accelerates smoothly, and the wake remains narrow. At 15°, Figure 4.50 shows more pronounced separation and an expanded wake, although still more controlled than the delta variant. The delta canard velocity contours, shown in Figures 4.53 and 4.55, reveal larger regions of flow detachment and a wider low-velocity region behind the trailing edge, particularly at higher deflection. Pressure contours for the swept clipped delta canard (Figures 4.49 and 4.51) display steady surface loading at 10°, with pressure rising near the root and leading edge. At 15°, a greater pressure difference appears across the span. In Figures 4.53 and 4.55, the delta canard produces a much steeper pressure gradient, with high-pressure buildup along the lower surface and strong pressure drop on the upper surface. This creates greater lift but also contributes to increased drag due to amplified pressure differential and wider flow separation. Overall, the swept clipped delta canard demonstrates better aerodynamic efficiency through smoother surface loading and more stable wake behavior. It performs well under moderate deflection and introduces less overall drag. The full delta canard produces stronger control forces, but this comes with significant drag penalties and flow instability at higher angles.

5.2. 3D Models

Following the results gathered from the 2D simulations of nose cone, tail fin, and canard geometries, three potential 3D rocket configurations have been developed. Each concept represents a unique approach to vehicle design, prioritizing different aerodynamic outcomes based on the collected performance data. These designs are proposed as candidates for future full-body 3D

modeling and simulation. They can serve as a foundation for testing complete flow interactions across all components and for refining aerodynamic control strategies in high-speed applications.

5.2.1. Configuration I – Efficiency Oriented Rocket

The efficiency-focused configuration is designed to minimize total aerodynamic drag during flight. It incorporates the von Kármán nose cone with a fineness ratio of 6:1, which showed the lowest drag coefficient among the tested profiles. This shape produced smoother shock patterns and favorable pressure recovery, especially compared to the long ellipsoid. With its mathematically optimized curvature, the von Kármán profile helps delay shock formation and reduces the overall drag force acting on the vehicle's forward section. At the rear, trapezoidal tail fins at 10° deflection are selected for their consistently low drag behavior and stable flow characteristics. In the 2D results, these fins maintained attached flow along most of the surface and produced a lower drag coefficient than their clipped delta counterparts. Their geometry supports efficient stabilization without introducing strong separation or excessive wake formation, which is essential for reducing base drag in the full 3D body.

The swept clipped delta canards at 10° further contribute to aerodynamic cleanliness by offering minor control input with minimal flow disruption. The canard's tapered and compact shape directs local airflow without creating strong shock interactions or pressure imbalances. It also complements the von Kármán nose cone by maintaining attached flow along the forebody, preserving laminar behavior over larger portions of the airframe. Together, this configuration presents an ideal setup for sounding rockets or high-altitude vehicles where drag reduction is essential. Its geometry focuses on efficient flow shaping and limited surface disturbance, making it suitable for passive-stabilized flights with little to no trajectory correction. It would perform best in environments where energy conservation and altitude gain are top priorities.

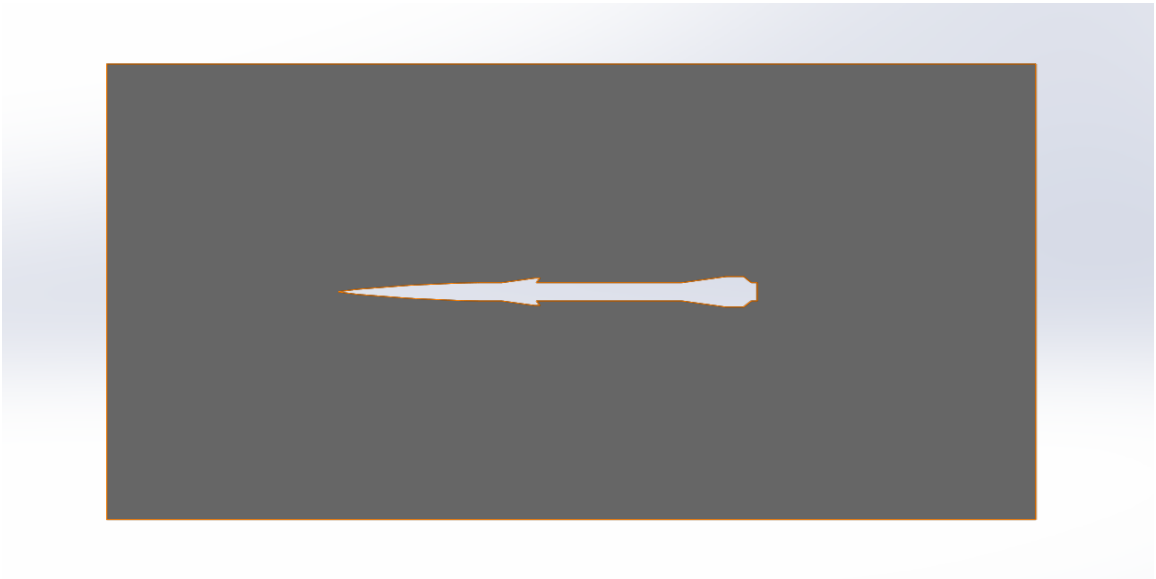

Figure 5.1 – Configuration I: efficiency oriented rocket 2D model.

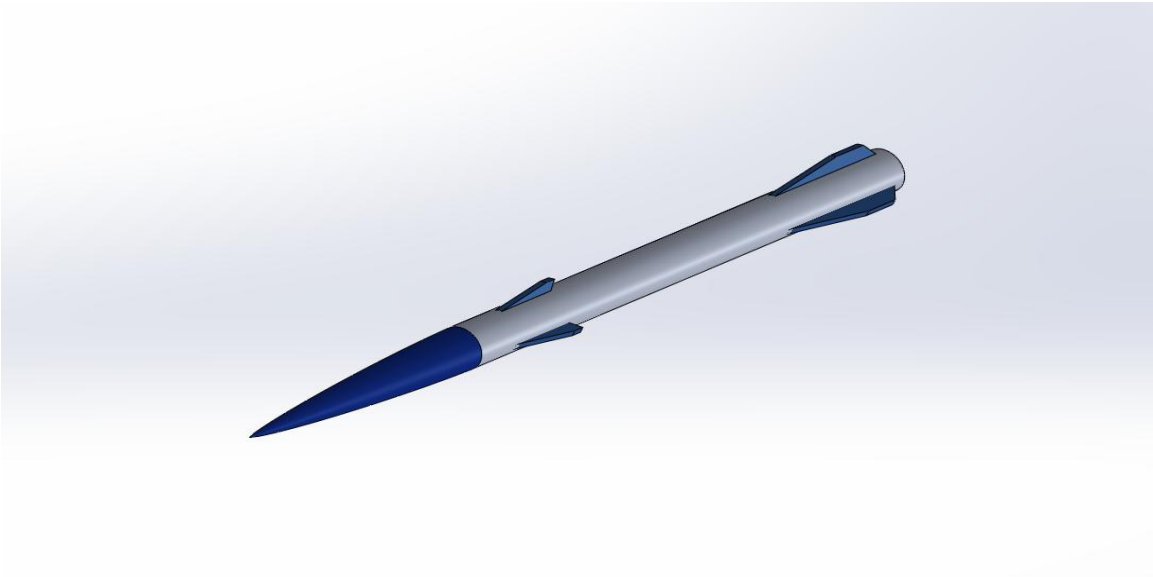

Figure 5.2 – Configuration I: efficiency oriented rocket 3D model.

5.2.2. Configuration II – Control Authority Rocket

The second configuration prioritizes control force generation over drag efficiency. It combines geometries that showed strong pressure gradients and wake development in the 2D analyses, which are favorable for producing significant aerodynamic moments. This setup is intended for rockets or atmospheric vehicles requiring strong pitch and yaw control or rapid course corrections during flight. The nose cone selected is the long ogive with a 7:1 fineness ratio, which demonstrated stable drag behavior while providing additional surface area to influence forward pressure distribution. Although not as efficient as the von Kármán shape, the longer ogive can enhance flow shaping over the nose and support greater interaction with forward-mounted control surfaces like canards.

At the rear, clipped delta tail fins deflected at 15° are used to maximize lateral and longitudinal control force. These fins generated the highest drag coefficients during the 2D simulations, but they also showed strong pressure differentials and early wake development, which can be leveraged for maneuverability. Their sharply swept geometry increases flow curvature and surface pressure variations, resulting in greater aerodynamic authority when used in dynamic control systems. For the forebody, full delta canards at 15° are selected due to their large surface area and strong lift potential. The 2D results indicated significant pressure gradients between the upper and lower surfaces, especially at higher deflection. While these canards introduce noticeable drag, they produce high control moments and are capable of actively steering or stabilizing the rocket, even in aggressive flight conditions. This configuration is ideal for mission profiles that require in-flight course correction, descent targeting, or guidance control through atmospheric layers.

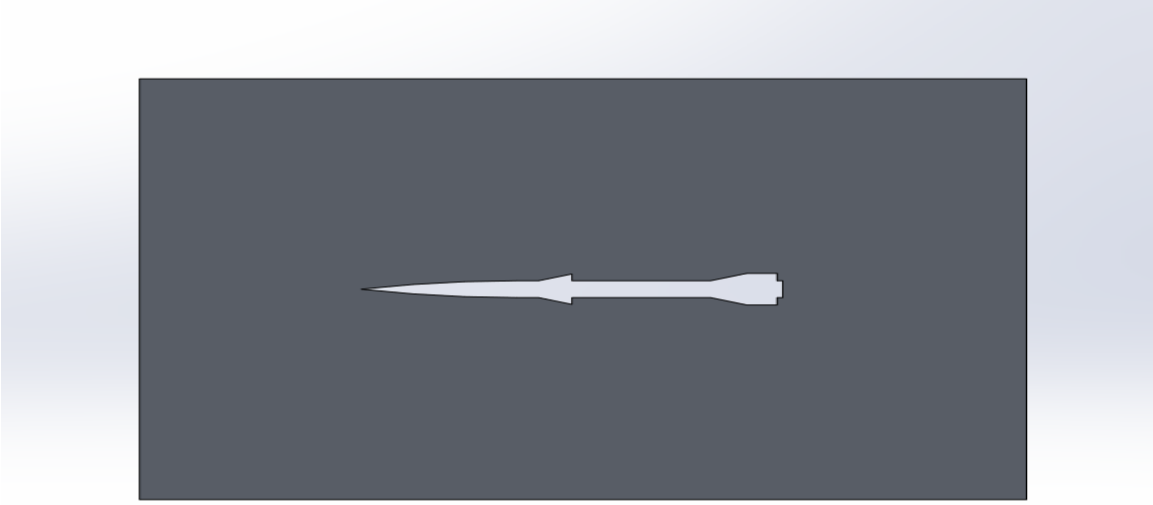

Figure 5.3 – Configuration II: control authority rocket 2D model.

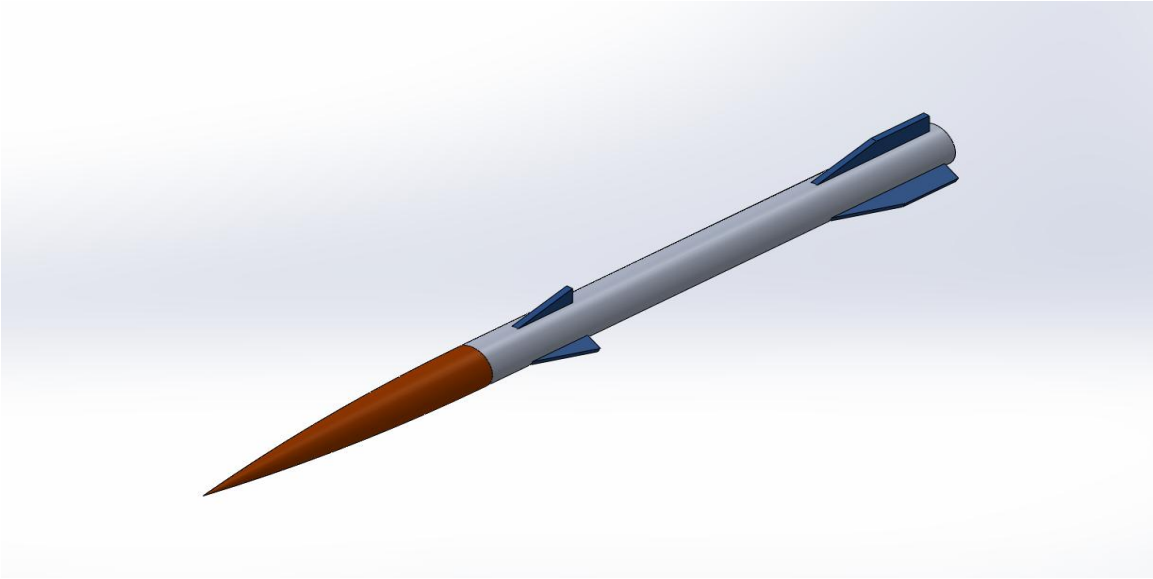

Figure 5.4 – Configuration II: control authority rocket 3D model.

5.2.3. Configuration III – Balanced Performance Rocket

The final configuration aims to find a compromise between aerodynamic efficiency and control authority, offering a balanced design suitable for general purpose or multi-mission rockets. Each selected component provides favorable performance without dominating in either drag reduction or control force generation. The ogive nose cone with a 6:1 fineness ratio was chosen for its reliable drag performance and clean surface shaping. It delivered consistently low drag values during the 2D testing while offering a more gradual pressure transition than the long

ellipsoid. Although it does not match the von Kármán in pure efficiency, it benefits from a simpler curvature and predictable flow interaction, which makes it easier to integrate with canards and forward-body systems.

For the tail, trapezoidal fins at 15° deflection were selected to improve stability while still managing aerodynamic resistance. At this deflection angle, the trapezoidal fins showed increased wake formation but maintained more even pressure distribution than the clipped delta fin. The slightly higher drag is balanced by improved control response compared to the 10° setup, making this an effective middle ground for passive and active flight stability. The swept clipped delta canards at 15° complete the configuration by offering moderate control authority with controlled surface loading. In the 2D simulations, these canards produced measurable control forces while avoiding the high-pressure spikes and wake intensities observed with the full delta design. The lower drag and cleaner flow behavior allow for consistent pitch input without compromising the overall aerodynamic footprint of the vehicle.

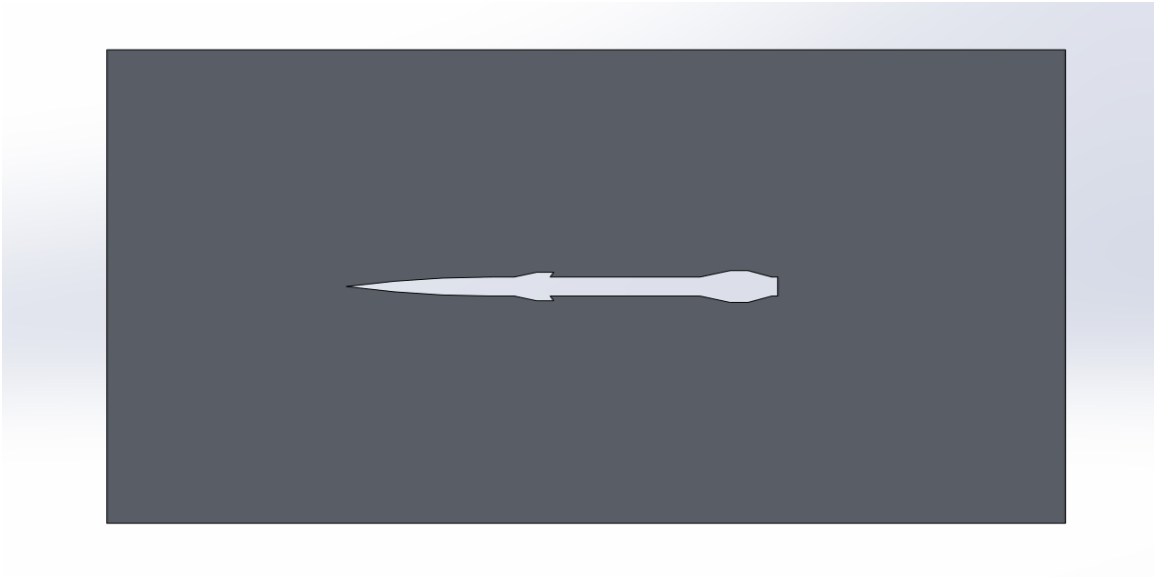

Figure 5.5 – Configuration III: balanced performance rocket 2D model.

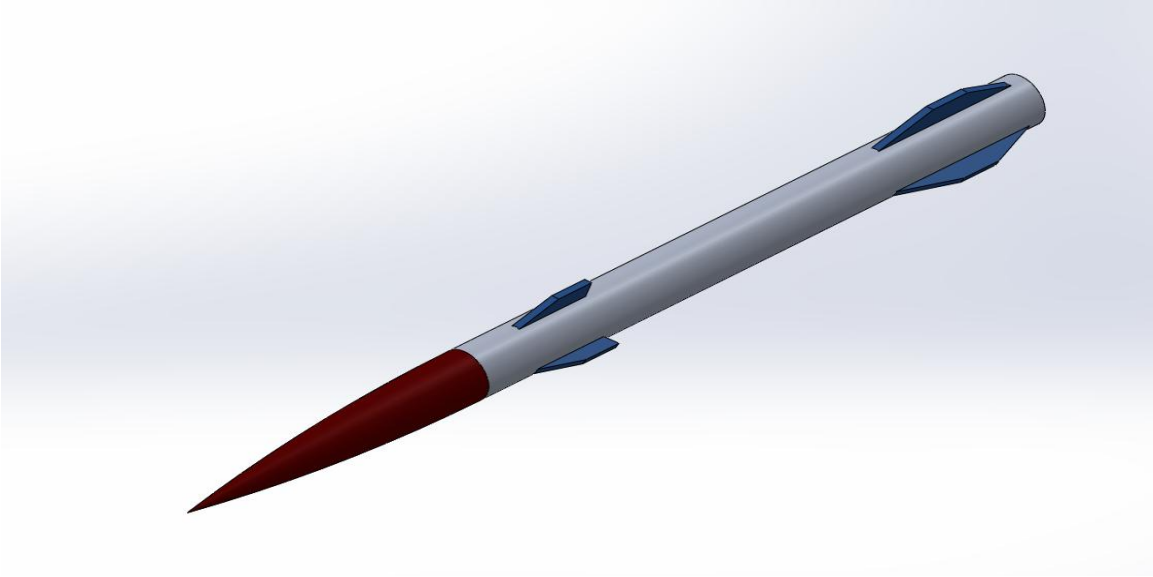

Figure 5.6 – Configuration III: balanced performance rocket 3D model.

6. Future Work

This project concluded the first step in optimizing the aerodynamics of a supersonic rocket using two-dimensional CFD simulations. Even though a lot was accomplished, there's still a ton of room to keep pushing the research to get closer to real-world rocket conditions. Right now, the analysis focused mainly on isolated nose cone, tail fin, and canard setups at Mach 1.5, giving a strong foundation in how these parts behave. But designing rockets for real missions demands a bigger picture view; looking at how everything interacts, how the environment messes with the rocket, and how it flies. Future work can take this project from strong basics to something that could stand up in real aerospace testing. One of the biggest upgrades would be to move from two-dimensional to full three-dimensional simulations. Real rockets are messy, complex 3D bodies, and the way the nose cone, fins, canards, and body shape affect each other is a huge deal for stability and performance. A 3D CFD setup would capture key things like asymmetric flow separation, crossflow effects on fins, and body interference on control surfaces, things you can't see in 2D. By building a full 3D rocket model with the best nose cone, fin, and canard from this project, future work could get much more realistic aerodynamic force and moment predictions.

Another major step would be looking at different altitudes. This project worked at 8,000 meters, but real rocket flights covered everything from sea level to the edge of space. Temperature, pressure, and density shift a lot as you climb, and those changes mess with shock waves, boundary layers, and drag. Simulating different points along the flight would show how the rocket's behavior shifts with altitude and help build better, more reliable designs for missions that need to reach higher or move faster. It would also be huge to simulate full launch conditions instead of a steady wind tunnel-style freestream. Rockets don't launch into perfect conditions they fight gravity, crosswinds, and high angles of attack during ascent. Future work should model vertical launches, Mach transitions, and gusty winds to see how the rocket holds up through the most intense phases of flight. This would give a much better idea of stability margins and control effectiveness when it counts.

Another critical addition would be heat transfer modeling. Supersonic rockets get hammered by aerodynamic heating, especially on the nose cone and leading edges. Future work could predict temperature distributions and figure out where the rocket needs thermal protection systems (TPS) to survive the flight. Coupling heat and airflow models would bring the research one step closer to full mission-readiness. Taking things even further, future work should move toward full airframe optimization instead of looking at nose cones, fins, and canards one at a time. The real trick is getting the whole rocket working together minimizing drag while keeping control authority and stability. Future designs could balance trade-offs depending on mission goals, like maximizing altitude or hitting precise targets. A complete optimization would show what real-world rockets must juggle.

Another exciting next step would be simulating active control surfaces. In this project, fins and canards were static. But real rockets often have moving fins for mid-flight corrections. Future models could simulate dynamic fin and canard movements, using basic control algorithms to adjust for flight conditions. Adding that kind of active control would get even closer to operational systems like interceptor missiles or next-gen space launchers. Lastly, the ultimate step would be to build and test real hardware. Wind tunnel tests, small prototype launches, or even full-scale trials would give the data needed to validate the simulations. Testing would close the loop from computer models to real-world performance, making it possible to fine-tune the designs and prove they work.

7. Conclusion

This project successfully demonstrated the aerodynamic optimization of a sounding rocket operating at Mach 1.5, focusing on critical design elements such as nose cone profiles, tail fin shapes, and canard configurations. Through CFD analyses, the von Kármán nose cone at a 6:1 fineness ratio emerged as the most efficient design, significantly reducing drag and promoting smoother flow characteristics. Similarly, the trapezoidal tail fin showed superior performance, balancing aerodynamic stability with minimal drag penalties across different deflection angles. Among the canard options, the swept clipped delta design proved the most advantageous, delivering effective control forces while maintaining low drag, thus making it an ideal choice for vehicles requiring aerodynamic responsiveness without heavy performance compromises.

Building on these findings, three distinct 3D rocket configurations were proposed, each tailored to prioritize different mission goals: aerodynamic efficiency, control authority, and balanced performance. These conceptual designs demonstrate the importance of complete optimization, where the interaction between all aerodynamic surfaces must be carefully considered to meet the demands of real-world supersonic flight. Furthermore, this research highlights the value of structured CFD methodologies and provides a foundation for expanding into more complex studies, including three-dimensional simulations, launch environment modeling, thermal effects analysis, and active control systems. Each of these future paths offers the opportunity to further refine and validate the designs presented in this work.

Ultimately, the insights gained from this project not only enhance the understanding of high-speed aerodynamic behavior but also pave the way for practical applications in modern aerospace vehicles like surface to air missiles. By combining computational analysis with targeted design improvements, this research contributes to the ongoing development of more efficient, stable, and versatile rockets. The knowledge built here lays a foundation for future testing, validation, and continued advancement toward operational supersonic and hypersonic flight technologies.

REFERENCES

[1] Velmani, M., Suresh, V., "Numerical Study of Freestream Turbulence Effects on the Nose Cones in Supersonic Flow," *Aircraft Engineering*, Vol. 95, No. 2, pp. 214–224, 2023. https://doi.org/10.1108/AEAT-02-2022-0039.

[2] Shah, V.K., Ateeb, K., Razzaq, M., Varun, C., Avinash, B., "Determination of the Optimum Nose Cone Geometrical Shape for Supersonic Missile," *Materials Today: Proceedings*, Vol. 64, pp. 749–754, 2022. https://doi.org/10.1016/j.matpr.2022.05.205.

[3] Belega, B.A., "Analysis of New Aerodynamic Design of the Nose Cone Section Using CFD and SPH," *INCAS Bulletin*, Vol. 7, No. 2, pp. 43–52, 2015. https://doi.org/10.13111/2066-8201.2015.7.2.4.

[4] Eghlima, Z., Mansour, K., "Effect of Nose Shape on the Shock Standoff Distance at Nearsonic Flows," *Thermophysics and Aeromechanics*, Vol. 23, No. 4, pp. 499–512, 2016. https://doi.org/10.1134/S086986431604003X.

[5] Sahbon, N., Murpani, S., Michałów, M., Miedziński, D., Sochacki, M., "A CFD Study of the Aerodynamic Characteristics of Twardowsky and FOK Rockets," *Prace Instytutu Lotnictwa / Transactions on Aerospace Research*, Vol. 2022, No. 1, pp. 35–58, 2022. https://doi.org/10.2478/tar-2022-0003.

[6] Cadamuro, R., Cazzola, M.T., Lontani, N., Riboldi, C.E.D., "A Static Stability Analysis Method for Passively Stabilized Sounding Rockets," *Aerospace*, Vol. 11, No. 3, Article 242, 2024. https://doi.org/10.3390/aerospace11030242.

[7] Milne, B., et al., "High-Fidelity Dynamics Modelling for the Design of a High-Altitude Supersonic Sounding Rocket," *Designs*, Vol. 7, No. 1, Article 32, 2023. https://doi.org/10.3390/designs7010032.

[8] Barrowman, J.S., "The Practical Calculation of the Aerodynamic Characteristics of Slender Finned Vehicles," *Scientific and Technical Aerospace Reports*, Vol. 39, 2001.

[9] Kumar, A., Shukla, R.K., Gusain, K.S., Sadar, A., "Study of Effect of Mach Number on Coefficient of Drag of Sounding Rocket by Computational Method," *IOP Conference Series: Materials Science and Engineering*, Vol. 1104, No. 1, Article 012029, 2021. https://doi.org/10.1088/1757-899X/1104/1/012029.

[10] Famellos, P., Skevas, A., Koutsiadis, A., Koutsouras, C., Panagiotou, P., "Design and Analysis of a Base Bleed Unit for the Drag Reduction of a High-Power Rocket Operating at

Transonic Speeds," *Aerospace*, Vol. 11, No. 5, Article 385, 2024. https://doi.org/10.3390/aerospace11050385.

[11] Brocksmith, J.B., "Effects of Tubercles on the Drag of Rocket Fins at Very High Reynolds Numbers Using CFD Analysis," *ProQuest Dissertations & Theses*, 2020.

[12] Sankalp, S.S., Sharma, V., Singh, A., Salian, A.S., Srinivas, G., "Computational Analyses of Tail Fin Configurations for a Sounding Rocket," *Aerospace Systems*, Vol. 5, No. 2, pp. 233–246, 2022.

[13] Li, C.C., Tai, C.S., Lai, C.C., Fu, S.M., Tsai, Y.C., "Study of the Aerodynamic Characteristic and Flight Trajectories in a Tail Fin-Stabilized Projectile with Different Shapes," *Procedia Engineering*, Vol. 79, pp. 108–113, 2014. https://doi.org/10.1016/j.proeng.2014.06.317.

[14] Silva, R.G.A.D., Damilano, J.G., Azevedo, J.L.F., "A Sensitivity Investigation on the Aeroelastic Dynamic Stability of Slender Spinning Sounding Rockets," *Journal of Aerospace Technology and Management*, Vol. 5, No. 1, pp. 15–26, 2013. https://doi.org/10.5028/jatm.v5i1.192.

[15] Minotti, A., Teofilatto, P., Pontani, M., Pallone, M., "Design Methodology and Performance Evaluation of New Generation Sounding Rockets," *International Journal of Aerospace Engineering*, Vol. 2018, Article ID 1678709, pp. 1–16, 2018. https://doi.org/10.1155/2018/1678709.

[16] Endo, K., Kumamoto, A., Katoh, Y., "Observation of Wake-Induced Plasma Waves Around an Ionospheric Sounding Rocket," *Journal of Geophysical Research: Space Physics*, Vol. 120, No. 6, pp. 5160–5175, 2015. https://doi.org/10.1002/2014JA020047.

[17] de Neto, J.A.O., Basso, E., Azevedo, J.L.F., "Aerodynamic Study of Sounding Rocket Flows Using Chimera and Patched Multiblock Meshes," *Journal of Aerospace Technology and Management*, Vol. 3, No. 1, pp. 87–97, 2011. https://doi.org/10.5028/jatm.2011.03016810.

[18] Bryson, H., Sültrop, H.P., Buchanan, G., et al., "Vertical Wind Tunnel for Prediction of Rocket Flight Dynamics," *Aerospace*, Vol. 3, No. 2, Article 10, 2016. https://doi.org/10.3390/aerospace3020010.

[19] Tsenov, G., Yovkov, K.G., "Computation of Hypersonic Blunt Body Heat Transfer: Model Development and Validation," *Aerospace Science and Technology*, Vol. 122, Article 107437, 2022. https://doi.org/10.1016/j.ast.2022.107437.

[20] Kim, B.K., Al-Obaidi, A.S.M., "Investigation of the Effect of Nose Shape and Geometry at Supersonic Speeds for Missile Performance Optimisation," *Journal of Physics: Conference Series*, Vol. 2523, No. 1, Article 012010, 2023. https://doi.org/10.1088/1742-6596/2523/1/012010.

Appendix

Appendix A – Code for calculating the Cd of a nose cone

```
% Referenced to be used for future work %
% Classwork from AE266 %
clc; clear; close all;
% Given Data
M_inf = 1.5; % Freestream Mach number
gamma = 1.4; % Ratio of specific heats
L = 1.0; % Length of the body
a1 = sqrt(3)/3; % Linear coefficient
a2 = -sqrt(3)/6; % Quadratic coefficient
% Discretization
n_panels = 6; % Number of panels
dx = L / n_panels; % Panel width
x = linspace(0, L, n_panels+1); % Panel boundary points
y = a1*x + a2*x.^2; % Surface profile
dy_dx = a1 + 2*a2*x; % Slope of the surface
theta = atan(dy_dx); % Surface inclination angle
% Newtonian Theory
Cp_newton = 2 * (sin(theta)).^2;
% Modified Newtonion
Cp_max = (2/(gamma*M_inf^2)) * ((((((gamma+1)^2)*M_inf^2)/
(4*gamma*M_inf^2-2*(gamma-1)))^(gamma/(gamma-1))) * ((2*gamma*M_inf^2-
(gamma-1))/(gamma+1))-1);
Cp_newton_mod = Cp_max * (sin(theta)).^2;
% Tangent-Wedge Method (Using oblique shock relations)
Cp_tangent = zeros(size(theta));
for i = 1:length(theta)
if theta(i) > 0 % Only for leading edge and wedge sections
beta_guess = theta(i) + (20 * pi / 180); % Initial guess for beta
beta_sol = fzero(@(beta) tan(theta(i)) -
2*cot(beta)*((M_inf^2*sin(beta)^2-1)/(M_inf^2*(gamma+cos(2*beta))+2)),
beta_guess);
M1n = M_inf * sin(beta_sol);
M2n = sqrt((1 + ((gamma-1)/2) * M1n^2) / (gamma*M1n^2 - (gamma-1)/2));
P_ratio = 1 + ((2*gamma)/(gamma+1)) * (M1n^2 - 1); % Pressure ratio
Cp_tangent(i) = (2 / (gamma * M_inf^2)) * (P_ratio - 1);
end
```

```
end
% Shock-Expansion Method
Cp_shock_exp = zeros(size(theta));
for i = 1:length(theta)
if theta(i) > 0 % Compression
K = M_inf * theta(i); % Hypersonic similarity parameter
1
P_ratio = 1 + (((gamma*gamma+1)/4))*(K^2)+(gamma*K^2)*sqrt(((gamma
+1)/4)^2+1/K^2);
Cp_shock_exp(i) = (2 / (gamma * M_inf^2)) * ((P_ratio - 1));
end
end
% % Differential drag force components
dA = dx * cos(theta); % Projected area element in the x-direction
dD_newton = Cp_newton .* dA .* sin(theta);
dD_newton_mod = Cp_newton_mod .* dA .* sin(theta);
dD_tangent = Cp_tangent .* dA .* sin(theta);
dD_shock_exp = Cp_shock_exp .* dA .* sin(theta);
% Drag Coefficient Calculation
Cd_newton = 2 * sum(dD_newton) / L;
Cd_newton_mod = 2 * sum(dD_newton_mod) / L;
Cd_tangent = 2 * sum(dD_tangent) / L;
Cd_shock_exp = 2 * sum(dD_shock_exp) / L;
% Display Results
fprintf('Drag Coefficients:\n');
fprintf('Newtonian Theory: %.4f\n', Cd_newton);
fprintf('Modified Newtonian Theory: %.4f\n', Cd_newton_mod);
fprintf('Tangent-Wedge Method: %.4f\n', Cd_tangent);
fprintf('Shock-Expansion Method: %.4f\n', Cd_shock_exp);
```